July 2002 • NREL/SR-520-32535

Subcontractor Report

Identifying Electronic Properties Relevant to Improving the Performance and Stability of Amorphous Silicon Based Mid-Gap and Low-Gap Cells

Final Subcontract Report
16 January 1998–15 October 2001

J.D. Cohen
University of Oregon
Eugene, Oregon

National Renewable Energy Laboratory

1617 Cole Boulevard
Golden, Colorado 80401-3393

NREL is a U.S. Department of Energy Laboratory
Operated by Midwest Research Institute • Battelle • Bechtel

Contract No. DE-AC36-99-GO10337

July 2002 • NREL/SR-520-32535

Identifying Electronic Properties Relevant to Improving the Performance and Stability of Amorphous Silicon Based Mid-Gap and Low-Gap Cells

Final Subcontract Report
16 January 1998–15 October 2001

J.D. Cohen
University of Oregon
Eugene, Oregon

NREL Technical Monitor: B. von Roedern

Prepared under Subcontract No. XAF-8-17619-05

National Renewable Energy Laboratory

1617 Cole Boulevard
Golden, Colorado 80401-3393

NREL is a U.S. Department of Energy Laboratory
Operated by Midwest Research Institute • Battelle • Bechtel

Contract No. DE-AC36-99-GO10337

NOTICE

Available electronically at http://www.osti.gov/bridge

Available for a processing fee to U.S. Department of Energy
and its contractors, in paper, from:

U.S. Department of Energy
Office of Scientific and Technical Information
P.O. Box 62
Oak Ridge, TN 37831-0062
phone: 865.576.8401
fax: 865.576.5728
email: reports@adonis.osti.gov

Available for sale to the public, in paper, from:

U.S. Department of Commerce
National Technical Information Service
5285 Port Royal Road
Springfield, VA 22161
phone: 800.553.6847
fax: 703.605.6900
email: orders@ntis.fedworld.gov
online ordering: http://www.ntis.gov/ordering.htm

Printed on paper containing at least 50% wastepaper, including 20% postconsumer waste

PREFACE

This Final Technical Progress Report covers the work performed at the University of Oregon for the period 16 January 1998 to 15 October 2001 under NREL Subcontract Number XAF-8-17619-05. The following personnel participated in this research program:

NAME	TITLE	WORK PERFORMED
J. David Cohen	Principal Investigator	Program Manager
Yoram Lubianiker	Research Associate	Studies of degradation in mixed-phase dc sputtered material; studies of H-diluted a-Si:H films; Properties of high deposition rate a-Si:H; Properties of ETL matched films and devices.
Chih-Chiang Chen	Research Assistant	Defect properties of a-Si,Ge:H Alloys.
Kimon Palinginis	Research Assistant	Defect properties of United Solar low Ge fraction a-Si,Ge:H alloys; Studies of BP Solar, NREL HWCVD a-Si,Ge:H alloys.
Yanyang Tan	Research Assistant	Properties of a-Si:H samples deposited at high rates; ESR measurements.
Jennifer Heath	Research Assistant	Studies of United Solar matched films and devices; Studies of NREL ultra-high deposition rate samples.
Suman Iyer	Visiting Scientist	Properties of BP Solar a-Si:H samples deposited at high rates.

TABLE OF CONTENTS

LIST OF ILLUSTRATIONS

Page

LIST OF TABLES

EXECUTIVE SUMMARY

The work carried out under NREL Subcontract Number XAF-8-17619-05 has concentrated on five areas of study. For the first area we examined a set of samples produced by United Solar deposited under conditions of high hydrogen dilution just below the microcrystalline phase boundary. We found that the degraded film defect density *decreased* as the film thickness *increased*, in contrast to undiluted films which exhibited nearly uniform defect distributions. Corroborating our findings with X-ray diffraction (XRD) results obtained by Don Williamson on similar films, we concluded that the films were becoming more ordered and less defective just prior to the onset of a detectable microcrystalline component. Moreover, we found that under conditions where XRD provided evidence for the onset of microcrystallinity, we likewise found the appearance of the distinctive microcrystalline "shoulder" in our sub-band-gap photocapacitance spectra. Finally, we used AFM in conjunction with KFM microscopy to identify regions of microcrystallinity near the surface of these films which increased in size as the film thickness increased. Second, we report results on a set of samples produced by dc reactive magnetron sputtering by John Abelson's group at the University of Illinois. We identified the existence of a small microcrystalline component, roughly 5% of the total volume, distributed throughout the interior region of these films. For these films the degradation kinetics were found to be quite unusual; however, they could be accounted for by a model that postulated two phases of degrading material: (1) a-Si:H host material of good quality and (2) a more defective component associated with boundary regions near the microcrystallites.

Third, we investigated four sets of samples where the deposition rate had been varied to include samples grown at moderate to high rates. The first set of samples, produced at Electrotechnical Laboratory in Japan, was deposited under H_2 dilution at 10Å/sec. These films were found to exhibit extremely low deep defect densities and narrow Urbach tails, indicating they were of exceptional quality. The photocapacitance spectra for these films exhibited evidence for a small degree of microcrystallinity. The fill factors for a set of matched Schottky barrier cells tended to be inversely correlated with the deep defect densities in these samples. In the second (and most extensive) set of samples, deposited at BP Solar, both the hydrogen dilution and the power level were varied to produce a set of 9 films, with 6 matched devices, whose growth rate encompassed the range: 0.65 to 6Å/s. The performance of the devices, particularly the fill factors, decreased roughly monotonically with increasing growth rate. However, the deep defect densities were found to be nearly constant. By far the strongest correlation between film and device properties was found to involve the Urbach energies in this set of samples: an increasing bandtail width in the films correlated fairly directly with poorer fill factors in the matched devices. In the third set of samples, produced at United Solar, we found evidence for increasing defect densities and also somewhat larger Urbach energies for the films deposited at 3Å/s and 6Å/s. The fourth set of samples we examined were a couple of ultra-high growth rate HWCVD samples produced at NREL at 90Å/s and 130Å/s. We found that defect densities and Urbach energies were a bit higher than lower growth material, but only modestly so. For the 130Å/s sample the degraded defect densities were below 4×10^{16} cm^{-3} and the Urbach energy was 53meV. That is, these values were not really any higher than for device quality glow discharge a-Si:H deposited at 6Å/s.

In the fourth area of study, we examined a-Si,Ge:H mid-gap and low-gap alloys. For a series of six United Solar mid-gap a-$Si_{1-x}Ge_x$:H samples, with $0.02 \leq x \leq 0.2$, we used modulated photocurrent spectroscopy to identify two types of deep defects, which we identified as neutral Si and neutral Ge dangling bonds. For all the alloys in this series we found that the Ge dangling bonds dominated the total in the dark-annealed state while the Si dangling bond density was larger in the light-degraded state. For three of these samples (Ge fractions of 5, 13.5, and 20at.%) we also looked for correlations between film properties with corresponding device performance. Unlike the cases of high growth rate material, the Urbach energies for this set of alloy samples were nearly constant. Also in contrast to the results for the BP a-Si:H samples, the fill factors in the devices *did* appear to be strongly (inversely) correlated with the film deep defect densities provided that defect density exceeded about 7×10^{15} cm^{-3}. We also evaluated the quality of a-Si,Ge:H alloys from two sources that were new to us: dc glow discharge material from BP Solar and HWCVD deposited a-Si,Ge:H from NREL. Our measurements indicated that the BP Solar material seemed to have exceptional properties up to a Ge fraction of 40at.%. The NREL HWCVD alloy material, while very good for 5at.% Ge, appeared inferior for Ge fractions at or above 20at.%.

Finally, we utilized the United Solar low Ge fraction a-Si,Ge:H alloy films to provide new information about the fundamental mechanisms for deep defect creation. These films contain two types of deep defects (Si and Ge dangling bonds) that both degrade and anneal at different rates. We determined that correlations between the annealing of these defects required that a global mediating entity (e.g., mobile hydrogen or propagating strain) must be involved in the defect creation process. We also found that, in contrast to the metastable Si dangling bonds, there appeared to be a distinct and fairly low limit to the density of Ge dangling bond precursor sites. Light-induced annealing studies were also carried out and provided some additional insight.

1.0 INTRODUCTION

The work carried out over the past 3 1/2 years under NREL Subcontract XAF-8-17619-05 has contributed toward the goals of two of the Amorphous Silicon Sub-Teams: toward developing more stable mid-gap a-Si:H materials, and toward understanding and improving the properties of the low-gap a-Si,Ge:H alloys. An additional task has been to pursue these goals for materials produced at enhanced growth rates, because this is becoming increasingly important in the effort to reduce manufacturing costs.

Our experimental results are based on a variety of techniques sensitive to the properties of defect states in semiconductors: admittance spectroscopy, drive-level capacitance profiling, modulated photocurrent spectroscopy, and transient photo-capacitance (and photocurrent) spectroscopy. These characterization methods were used to determine electronic quantities important to the device performance of these amorphous semiconducting materials: the deep defect energy distributions and densities, Urbach bandtail energies, and the $\mu\tau$ products for holes. In most cases we examined the changes in the deduced electronic properties caused by light induced degradation.

Our experimental studies have been concentrated in roughly five areas. Specifically: (1) We have examined a-Si:H grown very close to the microcrystalline phase boundary, so-called "edge material", to help understand why such material is more stable with respect to light-induced degradation; (2) We have also studied the electronic properties, and degradation characteristics of mixed phase material that is mostly a-Si:H, but which contains a significant microcrystalline component; (3) We have examined the electronic properties of high deposition rate material. These studies have included both moderately high deposition rate material (up to 6Å/s) produced by the PECVD growth method, and extremely high deposition rate material (up to 130Å/s) produced by the HWCVD growth method. (4) We have examined series of a-Si,Ge:H alloys from several sources. In one extensive series of studies we examined low Ge fraction alloys in an attempt to learn more about the fundamentals of degradation in general. In a couple other studies we evaluated the properties of a-Si,Ge:H alloys produced by methods we had not previously examined. (5) Finally, for three different types of samples we compared basic material properties with companion cell performance data. This was carried out in each case on series of samples for which one or more specific deposition parameters were varied systematically.

In the Sections that follow, we first describe the samples studied and review the experimental techniques employed. In Sections 4, 5, and 6 we present our detailed results involving the electronic properties of the a-Si:H alloy samples, and in Sections 7 and 8 the a-Si,Ge:H samples. Section 8 focuses specifically on employing the low Ge alloys to explore fundamental aspects of light-induced degradation. In Sections 6 and 7 we also include reports on some studies that attempt to correlate materials properties with solar cell device performance. Finally, in Section 9 we summarize our findings and draw some general detailed conclusions.

2.0 SAMPLES

2.1 UNIVERSITY OF ILLINOIS SAMPLES

Both hydrogenated and deuterated films were deposited at a rate of 100Å/min by dc reactive magnetron sputtering of a 5"×12" planar Si target in an Ar + H_2 or Ar + D_2 plasma. The substrate temperature was 250°C, the Ar partial pressure was 0.14 Pa, and the H_2 or D_2 pressure was varied from 0.04 to 0.10 Pa. Films grown under such conditions using hydrogen have been found to have properties fully equivalent to a-Si:H deposited by plasma CVD.[1] Previous studies have determined that the transition from a-Si:H to fully μc-Si growth occurs at a hydrogen partial pressure of 0.5 Pa [2], and roughly a factor of two lower for deuterium.[3]

For the photocapacitance and photocurrent studies described below we evaporated semitransparent Pd contacts onto each film and reverse biased the junction at the p^+ c-Si substrate. Samples were studied in "state A" (annealed in the dark at 470K for 30 minutes) and in a light soaked "state B", produced by exposure to a tungsten-halogen light source at an intensity of 300mW/cm^2 for 150 hours.

We previously utilized Raman spectroscopy to establish the existence of a μc-Si component for each of these samples.[4] This method also allowed us estimate the relative volume fractions of crystallites in these samples. More information about the detailed structure of these films was obtained using high resolution plan-view TEM micrographs on a couple of the films. From such micrographs we identify a moderate density of crystallites with sizes in the 5 to 50nm range (see Section 5).

2.2 UNITED SOLAR SYSTEMS SAMPLES

2.2.1 Samples Deposited Using Hydrogen Dilution Near The Edge Of Microcrystallinity

Several series of undoped (i) films were produced at United Solar Systems Corp. by PECVD at varying levels of H-dilution and film thickness (0.5 to 2.5 μm), all at a deposition temperature of 300°C. These samples were employed in a 3-way collaboration [5] to correlate X-ray diffraction structural measurements (carried out at Colorado School of Mines), junction capacitance spectroscopic measurements of defect densities and distribution (University of Oregon), and p-i-n device performance (United Solar). The substrates included bare stainless steel (i/SS), amorphous n-layer-coated stainless steel (i/a-n/SS), and microcrystalline n-layer-coated stainless steel (i/μc-n/SS). The n-layers were typically about 20 nm thick. United Solar provided my group with three samples: One with no H-dilution (i/a-n/SS, 1.3 μm thick) and two with high hydrogen dilution but different i-layer thicknesses (i/a-n/SS, 1.05 and 1.3 μm thick)

2.2.2 United Solar High Growth Rate Samples

An initial series of three a-Si:H samples was obtained from United Solar: one low growth rate reference film was deposited using hydrogen dilution at 1Å/sec under conditions that

have produced the most stable, highest efficiency devices produced at United Solar. The other two samples were deposited at 3Å/sec and 6Å/sec. The first of these was deposited in a conventional PECVD reactor utilizing modified deposition conditions (higher rf power, etc.), while the second was deposited under VHF conditions using a 70MHz excitation frequency. Both films were deposited under conditions that have led to the best performing cells reported to date for these higher deposition rates. In each case the film was deposited on a stainless steel substrate over a thin contacting layer of n^+ a-Si:H. A Pd Schottky contact was deposited onto the top surface of each sample to enable characterization by our junction capacitance methods.

2.2.3 United Solar Glow Discharge Amorphous Silicon-Germanium Alloys With Low Germanium Fractions

United Solar provided us with a series of low Ge fraction a-Si,Ge:H material produced by rf glow discharge onto p^+ crystalline Si substrates. This series of six films had Ge fractions of 2at.%, 5at.%, 6.5at.%, 10at.%, 13at.%, and 20at.% and were 0.9μm to 1.2μm thick. A semitransparent Pd Schottky contact was deposited onto each such film to allow our characterization measurements. In each case they also fabricated a p-i-n device (SS/n-i-p/TCO) using each of these alloy fractions as the i-layer. Unfortunately, several of these devices utilized i-layers of varying thicknesses. However, three of the matched devices incorporated i-layers of 1600Å thicknesses. These were the samples with Ge fractions of 5at.%, 13at.%, and 20at.%. There was no intentional Ge composition grading in any of these samples.

2.3 BP SOLAR SAMPLES

2.3.1 Amorphous Silicon Samples at Various Growth Rates

A series of nine samples were deposited at BP Solar in collaboration with Gautam Ganguly to examine the properties of DC glow discharge i-layer a-Si:H films deposited using different levels of hydrogen dilution and growth rates. This study was intended to correlate films and matched device performance before and after degradation.

For materials characterization, the i-layers were deposited on p^+ crystalline silicon and/or SnO_2 coated specular glass substrates. These series of samples were deposited varying two of the external deposition parameters; specifically, the hydrogen dilution of silane and the plasma power. The pressure was kept constant. In this manner the deposition rate varied from 0.65 to 6Å/s. Specifically, the a-Si:H films were deposited using three levels of hydrogen: D/2 (“low dilution”), D (“standard”), and 2D (“high dilution”), as well as three power levels: C (“standard”), 3C (“high”), and 5C (“very high”). These i-layer films were 1 to 2.5μm thick.. Figure 1 displays the manner in which the growth rate varies for the standard (“D”) dilution gas mixture as a function of deposition power density.

Matched solar cell devices were fabricated in a glass/SnO_2/p/i/n/ZnO/Al structure using the identical series of growth conditions with the exception of excluding the high (3C) power level case. For the devices the i-layer thickness was kept close to 0.25μm. Table I indicates the matrix of samples studied in this manner and lists their growth rates in each case.

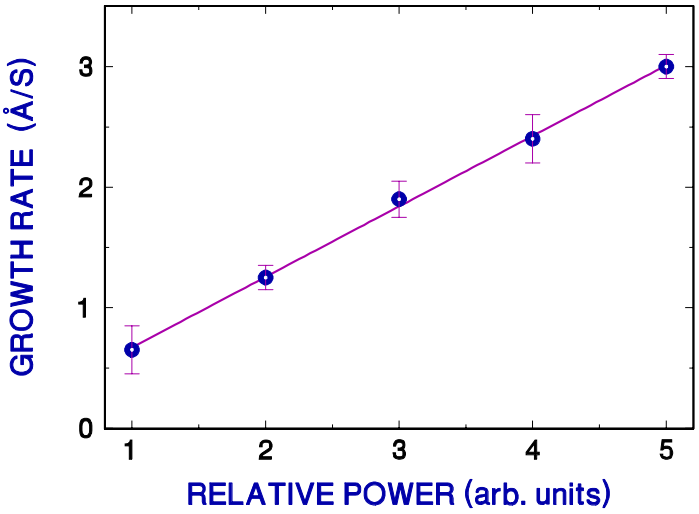

FIG. 1. Growth rate vs. deposition power for a series of BP Solar a-Si:H films with the standard ("D") hydrogen dilution. Thicknesses were determined by measuring the capacitance in the low temperature (carrier freeze-out) regime. The error bars were determined by repeating these measurements using several different contacts for each film.

TABLE I. Dependence of growth rate in Angstroms/second upon the growth parameters D (relative hydrogen dilution level) and C (relative discharge power level in chamber) for nine BP Solar samples.

DILUTION → POWER ↓	**D/2**	**D**	**2D**
C	**1.5**	**0.65**	**1.0**
3C	**3.7**	**1.9**	**1.8**
5C	**6.0**	**3.0**	**3.7**

2.3.2. Amorphous Silicon-Germanium Alloys

We also examined a preliminary series of three a-Si,Ge:H alloy samples deposited with Ge fractions of 5, 10, and 40at.%. These films were deposited onto p^+ crystalline Si substrates. In some cases a buffer layer of a few hundred Angstroms of standard a-Si:H was deposited onto the substrate first to help with film adhesion. This buffer layer does not affect the characterization measurements described below since our methods examine the film properties in the vicinity of a Pd Schottky barrier contact deposited on the top surface. The specifics of these three a-Si,Ge:H alloy films are given in Table II.

TABLE II. Characteristics of BP Solar a-Si,Ge:H alloy films.

Sample	Ge fraction (at.%)	Buffer layer?	Thickness (μm)
A9257-1	40	No	1.5
A9270-1	10	Yes	1.5
A9271-1	5	Yes	1.6

2.4 ELECTROTECHNICAL LABORATORY HIGH GROWTH RATE FILMS

Intrinsic a-Si:H films were grown using rf plasma decomposition of silane at a substrate temperature of 250°C. One set of samples was deposited from pure silane at a pressure of 20 mTorr with a gas flow of 30 sccm. The rf power was varied (in the range of 10 to 100 Watts), thus affecting the growth rate. Another set of samples was deposited from hydrogen diluted silane in a 4:1 ratio. The silane flow was kept the same as in the first set, so that the total pressure in the chamber was 100 mTorr. In this case the H_2 dilution results in only small decrease of growth rate. For comparison we also grew a non-diluted sample at the higher pressure. The growth conditions are summarized in Table III. More details on the growth system and conditions and more information about these samples are given in ref. 6.

TABLE III. The growth parameters and characteristics of the ETL samples. In all cases the silane flow was 30 sccm.

Sample	H_2 flow (sccm)	pressure (mTorr)	rf power (Watts)	thickness (μm)	growth rate (Å/sec)
12451	None	100	20	2.13	14.9
12464	120	100	100	2.1	15.22
12465	None	20	100	2.33	16.2
12466	120	100	60	1.9	10.55
12467	None	20	60	1.6	10.3
12468	120	100	20	1.64	2.5
12469	None	20	10	1.69	2.8

2.5 NREL HOT-WIRE CVD FILMS

2.5.1 Ultra-High Deposition Rate a-Si:H Material

Scientists at NREL have pioneered the hot-wire CVD growth method for the deposition of a-Si:H films and devices. Initially the effort in this regard was directed toward reducing hydrogen content while maintaining good electronic properties. It was hoped this might lead to materials that were more stable, and had lower optical gaps than a-Si:H produced by glow discharge. However, more recently the NREL effort in this regard has been focused on increasing growth rate while maintaining good electronic properties. It was demonstrated that HWCVD films could be deposited at rates exceeding 15Å/s while maintaining the same saturated

deep defect as films deposited at rates below 5Å/s [7]. More recently, through the use of multiple filaments and adjusting other deposition parameters, the growth rate of HWCVD a-Si:H films at NREL has been increased to over 100Å/s.[8]

Brent Nelson at NREL supplied us with three of these ultra-high growth rate samples for evaluation. These consisted of films deposited on stainless steel substrates at rates of 90Å/s, 110Å/s and 130Å/s. The hydrogen content of all three films was estimated to be 6 to 8at.%.

2.5.2 Hot-Wire Amorphous Silicon-Germanium Films

At the end of 1999 we received an extensive series of HWCVD samples from Brent Nelson at NREL. These films were deposited on a variety of substrates and primarily consisted of a-Si,Ge:H alloy material, with several pure a-Si:H films included for reference. The Ge content and substrates used are listed in Table IV. Many of these depositions produced films that were peeling or contained bubbles and were thus unsuitable for characterization by our methods. However, many good quality films were also produced, and results obtained on some of these films are included in Section 7.

TABLE IV. Hot-Wire CVD a-Si:H and a-Si,Ge:H films deposited by Brent Nelson at NREL and sent to us in November,1999. The Ge content and substrate types are indicated. "SS" denotes stainless steel; Dynasil 1000 is a type of fused quartz.

Sample	Ge Content	Substrate(s)	Thickness (μm)
H684	0	SS, Dynasil 1000, p^+ c-Si	2.4
H685	5	SS, Dynasil 1000, p^+ c-Si	2.0
H686	35	SS, Dynasil 1000, p^+ c-Si	2.9
H687	19.3	SS, Dynasil 1000, p^+ c-Si	2.6
H688	2	SS, Dynasil 1000, p^+ c-Si	2.0
H689	50	SS, Dynasil 1000, p^+ c-Si	2.3
H691	0	Dynasil 1000, p^+ c-Si	2.3
H693	0	c-Si	0.5

3.0 EXPERIMENTAL CHARACTERIZATION METHODS

The measurements employed in our studies rely on a set of experimental techniques which have all been described previously in some detail. They consist of (1) admittance spectroscopy as a function of temperature and frequency, (2) drive-level capacitance profiling (DLCP), (3) modulated photocurrent (MPC) spectroscopy, and (4) transient photocapacitance taken together with transient junction photocurrent spectroscopy. For completeness of this report we include a brief description of these method below. A more detailed description of most of these methods can be found in our final report published by NREL (SR-520-25802) in 1998.

3.1 ADMITTANCE SPECTROSCOPY

Our Schottky diode samples contain a depletion region which is characterized as a function of temperature and frequency before we undertake the more sophisticated capacitance based measurements described in Sections 3.2 to 3.4 below. Such measurements provide us with an estimate of film thickness: The temperature independent region at low T is simply related to the geometric thickness, d, by the formula $C = \varepsilon A/d$. Also, an Arrhenius plot of the frequency of the lowest temperature capacitance step (or conductance peak) *vs*. 1/T provides us with the activation energy of the ac conductivity, E_σ, which we identify with the Fermi energy position: $E_\sigma = E_C - E_F$.[9] These admittance measurements also give us an indication of the quality of our Schottky barriers which allow us to pre-screen our samples for further study.

3.2 DRIVE-LEVEL CAPACITANCE PROFILING

The drive-level capacitance profiling method has been described in detail in many publications [10,11]. It is similar to other kinds of capacitance profiling in that it provides us with a density vs. distance profile; however, this particular method was developed specifically to address the difficulties encountered in interpreting capacitance measurements in amorphous semiconductors. In this method we monitor the junction capacitance both as a function of DC bias, V_B, and as a function of the amplitude of the alternating exciting voltage, δV. One finds that to lowest order this dependence obeys an equation of the form:

$$C(V_B, \delta V) \quad = \quad C_O(V_B) + C_1(V_B)\,\delta V + \ldots$$

and that the ratio

$$N_{DL} = \frac{C_0^3}{2q\varepsilon A^2 C_1} \tag{1}$$

is directly related to an integral over the density of mobility gap defect states:

$$N_{DL} = \int_{E_C - E_e}^{E_F^0} g(E)\,dE \tag{2}$$

Here E_F^o is the bulk Fermi level position in the sample and E_e depends on the frequency and temperature of measurement:

$$E_e(\omega,T) = k_B T \log(\nu/\omega) \quad (3)$$

Thus, by altering the measurement temperature (or frequency) we obtain information about the energy distribution of the defects and, by altering the applied DC bias, we can vary the spatial region at which we detect the defects in the sample. That is, we can spatially profile the defects as a function of the position from the barrier interface.

In our current studies we typically measured 10 or 100Hz profiles for a series of temperatures between 320K to 360K. These data usually indicated a clear upper limit for N_{DL} which, we have shown [12], is equal to roughly one half the total defect density in these samples. Thus, this provides us with a quantitative measurement of the deep defect levels. In addition, because of the profiling information also obtained, we are able to assess the spatial uniformity of the electronic properties in these samples.

3.3 MODULATED PHOTOCURRENT SPECTROSCOPY

The modulated photocurrent (MPC) method is based upon measuring the complex current response to an applied oscillating light source. It is the frequency domain analogue of the more familiar transient photocurrent time-of-flight method, but provides a clearer signal in the long time regime where trapping of carriers into deep defects plays the dominant role. To avoid perturbing the occupation of the responding states we employ a 560nm LED at a very low photon flux of 10^{11} cm^{-2} s^{-1} which can be modulated up to frequencies up to 120 kHz. The MPC method was first applied to determine the thermal energy distribution of majority carrier trapping states in an amorphous semiconductor by H. Oheda [13] and the experimental procedure was refined by G. Schumm and G.H. Bauer in more recent studies [14].

An algebraic combination of the in- and out-of- phase current response gives a quantity that is directly proportional to the density of trapping states involved. According to the analysis by Brüggemann et. al. [15], the density of states at a thermal energy, E_ω, will be given by the modulus of the ac current density, |jac| and its phase lag ϕ with respect to the modulated light source:

$$g(E_\omega) = \frac{2N_C}{\nu\pi k_B T}\left\{\left[\frac{qG_1 A\mu_e F}{|j_{ac}(\omega)|}\right]\sin\phi - \omega\right\}, \quad \text{with } E_\omega = k_B T \log(\omega/\nu) \quad (4)$$

Here ν is the thermal emission prefactor, N_C is the effective density of conduction band states, q is the electronic charge, G_1 is the sinusoidal component of the generation rate at angular frequency ω, μ_e is the free electron mobility, and F is the electric field.

Such measurements can provide a very clear picture of the thermal energy distribution of majority carrier traps. Examples of such spectra will be discussed in Section 5.1.

3.4 TRANSIENT PHOTOCAPACITANCE AND PHOTOCURRENT

The general method of junction transient measurements on amorphous semiconductors has been discussed in detail in several earlier publications.[9,16,17] The basic physics of all such measurements is as shown in Fig. 2. We illustrate the situation for a semiconductor with one discrete deep gap states within the space charge region of a Schottky barrier which is subjected to a voltage "filling pulse". This pulse causes a non-equilibrium (filled) occupation of gap states to be established. As time progresses, the initial steady-state population is recovered through the excitation of trapped electrons to the conduction band where they can then move out of the depletion region under the influence of the electric field. In the dark this process proceeds entirely by the thermal excitation of trapped carriers. However, this process can be enhanced through optical excitation which is the basis of the photocapacitance and junction photocurrent techniques described below.

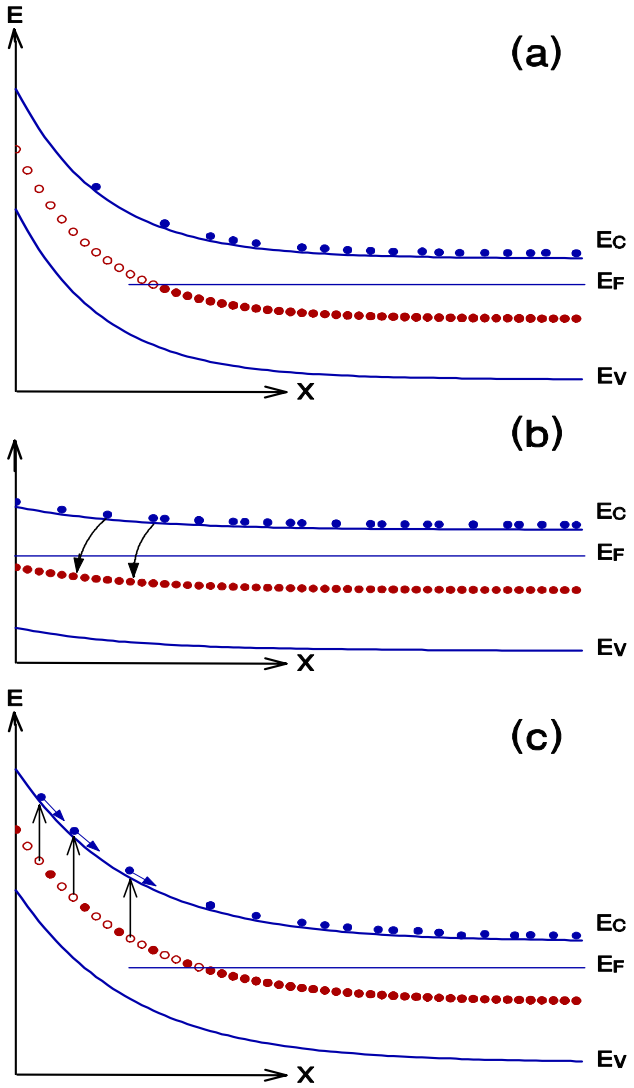

FIG. 2. Schematic diagram indicating the basic sequence of events in semiconducting junction transient measurements:

(a) Junction under reverse bias in quasi-equilibrium showing the electronic occupation of gap states (solid circles) plus empty gap states above E_F in deep depletion (open circles).

(b) During voltage "filling pulse" gap states capture electrons from the conduction band.

(c) Reverse bias is restored and occupied gap states above E_F are slowly released to the conduction band due to thermal or optical excitation processes.

The re-equilibration can be observed by the redistribution of trapped carriers, either as a change in the *junction capacitance* (which occurs because the depletion region will contract as negative charge is lost and the positive charge density increases) or by monitoring the *current* which results from the motion of this charge. However, the observation of capacitance transients has one significant difference compared to current transient measurements: The dominant type of emitted carrier (electron or hole) can be identified by the *sign* of the observed change in capacitance.

The methods of junction transient photocapacitance and photocurrent have also been discussed by us in great detail recently in the literature [18,19,20] and also in previous NREL reports. They represent types of sub-band-gap optical spectroscopy and provide spectra quite similar in appearance to PDS derived sub-band-gap optical absorption spectra or to CPM spectra. Instead of detecting absorbed energy, however, our photocapacitance and photocurrent transient methods detect the optically induced change in defect charge within the depletion region. However, unlike the CPM method, both of our junction based techniques are not greatly influenced by the free carrier mobilities since, once an electron (or hole) is optically excited into the conduction (valence) band it will either totally escape the depletion region on the slow timescale of our measurement (0.1 to 1s) or be retrapped into a deep state and not escape. In most cases we assume that almost all of the optically excited majority carriers (electrons) *do* escape but, in general, only a fraction of the minority carriers (holes) escape.

As mentioned above, we are also able to distinguish whether optical excitation of defect states comes about because of the excitation of trapped electrons to the conduction band or because of the excitation of valence band electrons into an empty mobility gap state. This ability to distinguish electron from hole processes is unique among all the various types of sub-band-gap optical spectroscopies.

4.0 DEFECT BEHAVIOR OF a-Si:H NEAR THE MICROCRYSTALLINE ONSET

During the Subcontract period we participated in a joint collaboration with researchers at United Solar and at Colorado School of Mines to examine the properties of a-Si:H films grown under hydrogen dilution close to the onset of microcrystallinity ("edge material").[21] United Solar provided hydrogen diluted samples of several thickness' (0.5, 1.5, and 2.5 μm on n^+ a-Si:H coated stainless steel) to Don Williamson for X-ray analysis. They also provided him with 0.5μm thick films on 3 types of substrates (bare stainless, n^+ a-Si:H coated stainless steel, and n^+ μc-Si coated stainless steel). They provided my group with two hydrogen diluted a-Si:H films of thickness' 1.05 and 1.3 μm on n^+ a-Si:H coated stainless steel, plus one undiluted (standard glow discharge) a-Si:H on n^+ a-Si:H coated stainless steel. For all samples we evaporated a semi-transparent Pd contact onto the top surface to produce a Schottky barrier for our junction measurements.

For the samples deposited on n^+ a-Si:H coated stainless steel, Don Williamson's X-ray analysis indicated that the films were purely amorphous at 0.5μm thick, were mixed-phase microcrystalline/amorphous for the 1.5μm thick film, and were predominantly microcrystalline at 2.5μm. The implication of his results was that the hydrogen diluted a-Si:H was approaching the onset of crystallinity as the film got thicker; the onset of distinct crystallinity occurred somewhere in excess of 1μm.

4.1 ELECTRONIC PROPERTIES OF a-Si:H NEAR MICROCRYSTALLINE ONSET

One of the tasks of my laboratory was to assess whether the electronic properties of these films were also varying as these hydrogen diluted films increased in thickness. Scientists at United Solar and ECD had reported that a-Si:H films grown under hydrogen dilution close to the onset of microcrystallinity exhibited a higher degree of stability [22]. Therefore, it seemed possible that the density of deep defects in the light-degraded state of these films would become lower as these films became thicker, at least until the onset of microcrystalline was reached.

The three films (one non H-diluted "standard" sample, plus two deposited with hydrogen dilution with different total thickness') were characterized in a light-degraded state produced by exposure to red-filtered light from a tungsten-halogen source at an intensity of $2 W/cm^2$ for 100 hours. The samples were immersed in methanol during light soaking to maintain a low surface temperature. Figure 3 displays a series of drive-level capacitance profiling (DLCP) data for the standard sample. Each profile was obtained using a measurement frequency of 33Hz and measurement temperatures were varied between 330K to 370K. Based upon cross correlation studies between ESR and DLCP on previous samples [12], we believe that a good estimate of the total defect density will be obtained by doubling the profile values displayed for the 370K curve. That is, this standard glow discharge sample has a defect density near 2×10^{16} cm^{-3} in its light degraded state.

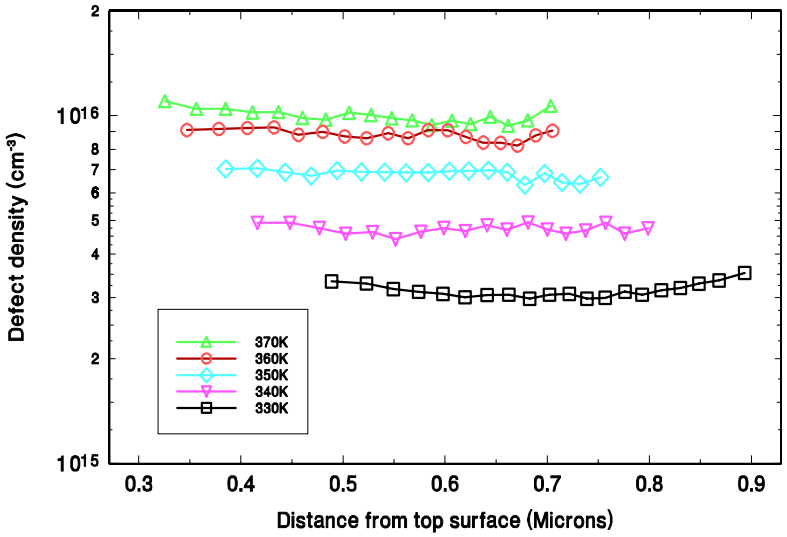

FIG. 3. Drive-level capacitance profiles for the United Solar standard glow discharge sample in its light degraded state obtained using a measurement frequency of 33Hz and several measurement temperatures. Note that the defect density profiles show very little spatial variation.

Figure 4 shows the DLCP profiles at different measurement temperatures obtained for the two a-Si:H grown with hydrogen dilution (in the light degraded state). Note that the profiles for the two samples of different thickness' are nearly identical except for the lowest temperatures where the profile distances approach the edge of the thinner sample. Also note that the higher temperature profiles exhibit considerable spatial variation, and also a defect density considerably smaller than indicated by the standard sample data, lying between 1.2 and 1.5×10^{16} cm^{-3}. In Figure 5 we display a direct comparison between the profiles for all three samples. These are shown for the two highest measurement temperatures where the profiles should be encompassing a larger part of the deep defect band. We see that the hydrogen diluted samples exhibit defect densities roughly a factor of 1.5 lower than the standard sample, and we also note the much stronger spatial variation of the profiles for the hydrogen diluted samples. This variation indicates a decrease in deep defect density toward the top surface of those films. That is, the density of light-induced deep defects becomes smaller as we move toward the onset of microcrystallinity as deduced from the X-ray studies of Don Williamson on United Solar samples deposited under the identical conditions. This tends to support the conclusion that it is this approach to microcrystallinity which leads to a more stable a-Si:H material evidenced, in this case, by a lower defect density in the degraded state.

In Figure 6, we display photocapacitance spectra taken for the two hydrogen diluted samples. The spectrum for the thinner sample is nearly identical to those of very high quality glow discharge samples reported previously [23,24,25]. The fit curve indicates an Urbach energy of 46meV. The thicker sample spectrum matches that of the thinner sample in both the bandtail regime and also at optical energies below 1.0eV where the signal is believed to originate solely from dangling bond defects in a-Si:H. However, the thicker sample has an additional feature at intermediate optical energies which, as we shall discuss in Section 5.1, indicates the presence of silicon microcrystallites. We believe that the volume fraction is very low for this sample, 1% or less. Indeed, such samples usually do not exhibit any evidence for crystallinity in Raman

spectroscopy. However, our results *are* consistent with Don Williamson's X-ray results that indicate a small degree of microcrystallinity for the 1.5□m thick samples grown in this fashion.

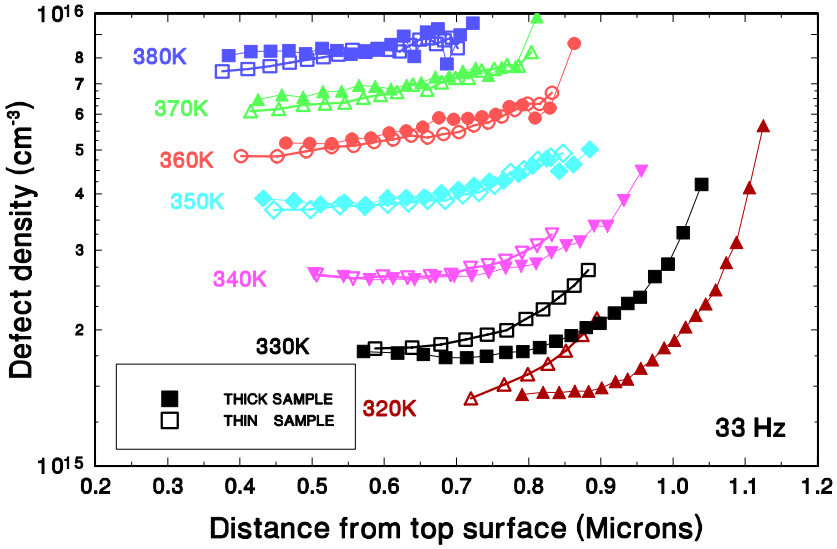

FIG. 4. Drive-level capacitance profiles for the two hydrogen diluted United Solar standard glow discharge samples in their light degraded state at several measurement temperatures. Note that the profiles show considerably more spatial variation than those of the standard sample.

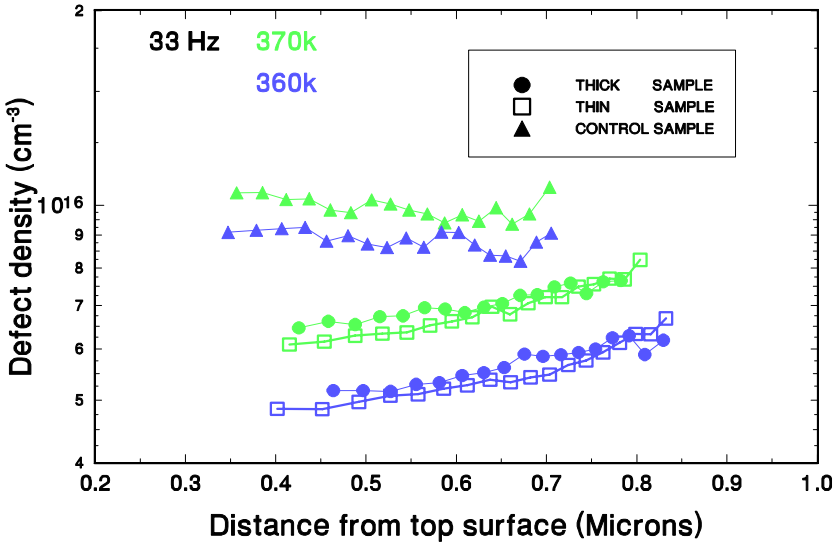

FIG. 5. Comparison of drive-level profiles for all three samples at the highest profiling temperatures. The total defect density in each film is estimated to be twice the value shown for the 370K curves in each case. Note that the profiles for the hydrogen diluted samples are significantly lower than for the standard sample and also indicate a much greater spatial variation.

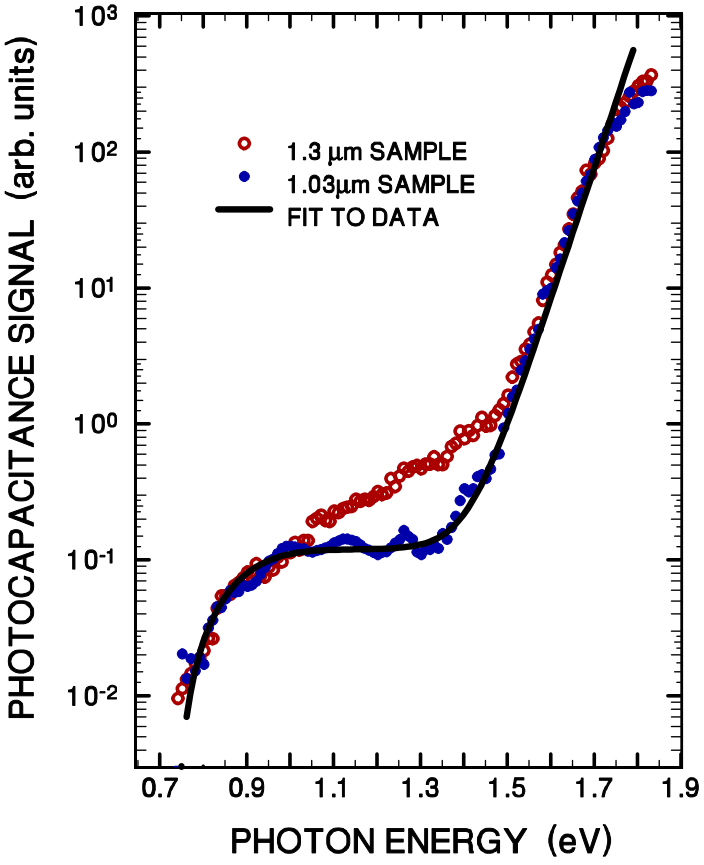

FIG. 6. Photocapacitance spectra for the two United Solar hydrogen diluted a-Si:H samples of different thickness. The thinner sample spectrum is quite similar to many published results for sub-band-gap spectra of a-Si:H in the literature. The thicker sample shows an additional feature at intermediate energies that we associate with the presence of a very small fraction of microcrystallites. The solid line is a fit to the thinner sample data which indicates an Urbach energy of 46meV and an estimated deep defect density of 1.5×10^{16} cm^{-3}. This latter value agrees quite closely with the defect density obtained from the DLCP measurements for this sample.

4.2 MORPHOLOGY OF THE MICROCRYSTALLINE ONSET IN a-Si:H

After studying the electronic properties, we attempted to obtain more detailed structural information regarding the nature of the amorphous/microcrystalline boundary region. We have been able to detect the presence of microcrystallites within the material using a completely new approach: by the simultaneous application of Atomic Force Microscopy (AFM) and Kelvin probe Force Microscopy (KFM) [26]. Thus, in contrast to previous structural studies which are primarily *global* probes of the film morphology (X-ray diffraction or Raman spectroscopy), the AFM tip when used as a Kelvin probe can image the contact potential difference (CPD) between the tip and a *local* sample environment. And, indeed, our results clearly show a difference in the work function of the microcrystallites with respect to the rest of the film. Thus, we have obtained the surface spatial distribution of the crystallites in our samples.

Our AFM and KFM measurements were carried out in collaboration with G. Lubarsky and Y. Rosenwaks at Tel Aviv University in Israel. The instrument was a commercial AFM (Autoprobe CP, Park Scientific Instruments) operating in the non-contact mode. For topographic imaging, the p^+ c-Si cantilever with a sharpened tip (<20nm radius) was driven by a piezoelectric bimorph at a frequency slightly above resonance. For the KFM measurements an alternating voltage (with a 20 kHz frequency) was applied to the cantilever to induce an alternating

electrostatic force. The CPD is then equal to the dc voltage required to null this force. The sensitivity of this measurement was better than 2mV.

In Fig. 7 we present typical results of the AFM and KFM measurements for the three United Solar samples studied. Starting with the AFM topography, one can see in Fig. 7(a) that the control sample is rather smooth, with height fluctuations of the order of 10 nm. On the other hand, the samples grown under high dilution conditions exhibit a more complicated structure. This consists of few "bumps" that are superimposed on a surface, the roughness of which is similar to that of the control sample. The density of these "bumps" in the thin sample (Fig. 7(b)) is smaller than in the thick sample (Fig. 7(c)), and their average height increases from 60 to 130 nm. Since we knew that the highly diluted material was close to the onset of microcrystallinity, we tentatively identified the "bumps" as microcrystallites. However, additional evidence was required to prove that these were not merely topographic fluctuations of the amorphous material.

This evidence is unambiguously provided by the KFM data, which are presented for the same locality characterized by the AFM. The control sample exhibits a uniform CPD with fluctuations smaller than 0.05 eV, as can be seen in Fig. 7(d). On the other hand, the diluted films exhibit higher CPD values at points exactly corresponding to the topographic "bumps" (Figs. 7(e) and 7(f) for the thin and thick films, respectively). It is noteworthy that few of the "bumps" seen in the thick sample do not exhibit a CPD value which is different from the rest of the film. Accordingly we believe that they merely represent a topographic change. However, most of the "bumps" seen in Figs. 7(e) and 7(f) must be understood as a different phase of the material, i.e., a microcrystalline phase. We thus conclude that the samples grown from diluted silane contain a small concentration of microcrystallites, at least in the top portion of each film. Furthermore, both the concentration and the size of these microcrystallites increase with film thickness.

We can attempt to interpret the origin of the observed 0.25V CPD variation observed in these crystalline features relative to the host a-Si:H matrix. The most straightforward explanation is in terms of an internal electric field at the microcrystalline/amorphous silicon boundary. We note that in a similar manner KFM measurements can detect changes in CPD p-n junction [26]. It is known [27] that in microcrystalline silicon (μc-Si:H) the Fermi energy is roughly 0.35 eV closer to the conduction band edge than in a-Si:H. Since the conduction band offset between a-Si:H and c-Si:H is about 0.1 eV [28,29], the existence of a 0.25 CPD difference naturally follows. Also, E_F at the microcrystallites' surfaces will lie roughly 0.7eV below E_C so that interfacial defect states are likely to be ionized, leading to an internal field around the microcrystallites.

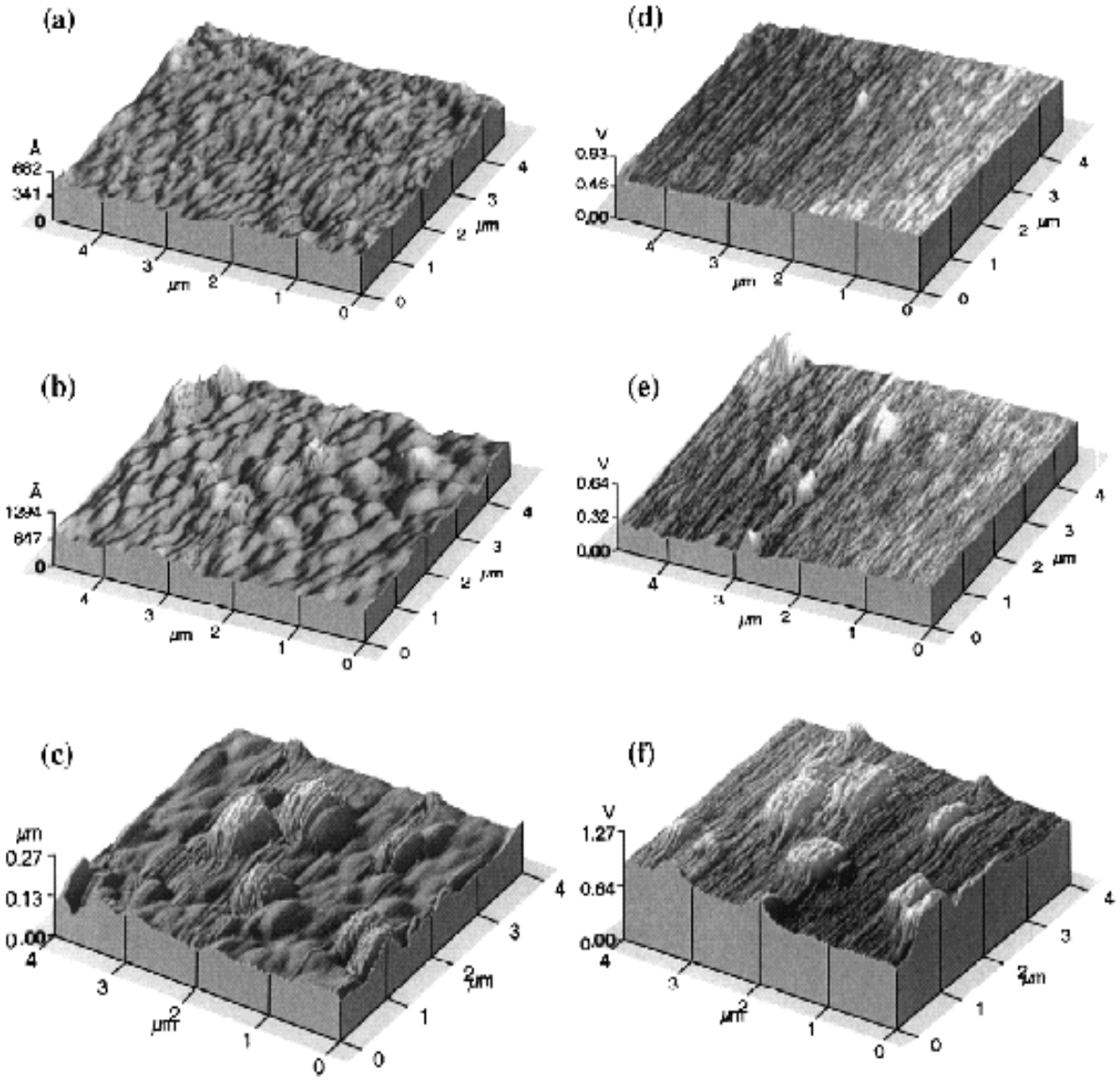

FIG. 7. AFM topographic images (a,b,c) and KFM contact potential difference images (d,e,f) of three United Solar amorphous silicon films. These three films are an undiluted silane a-Si:H sample (a,d), a 1.03 µm thick a-Si:H film deposited under high hydrogen dilution (b,e), and a thicker, 1.3 µm a-Si:H film deposited under high hydrogen dilution (c,f). The bumps in the KFM produced images exhibiting higher contact potentials are identified as (clusters of) microcrystallites embedded in the a-Si:H host material.

Since the differences in photoconductivity between a-Si:H and microcrystalline silicon are small [27], we expect that under band to band excitations the CPD difference will diminish, as a result of the similar energetic location (with respect to the vacuum level) of the quasi Fermi levels. Indeed, KFM measurements performed in the presence of HeNe laser illumination indicate a CPD difference smaller than 0.05 eV between the two phases.

The present results can assist in understanding the improved performance of solar cells that utilize the high dilution material. Intuitively, one expects that the presence of microcrystallites, with their considerably smaller gap, would provide an efficient channel for photocarrier recombination. Indeed, one recent model has proposed that this is the reason for their improved stability [26]. However, this explanation ignores the inevitable poorer device performance that would result from the corresponding shorter lifetimes. The excellent cell performance of these materials proves that the crystallites cannot be acting as an efficient recombination channel. Indeed, the uniform quasi Fermi energy indicates that the crystallites do not act as an efficient electron trap. In addition, the holes will not easily diffuse into the crystallites simply because their diffusion length is far shorter than the distance between the crystallites. Thus, it seems likely that the improvement of the devices is simply a result of the improved quality of the amorphous component, which is manifested by the low defect densities reported in Section 4.1.

5.0 LIGHT INDUCED DEGRADATION KINETICS IN MIXED PHASE SAMPLES

5.1 EVIDENCE FOR PRESENCE OF MICROCRYSTALLINE COMPONENT

In this part of our work we have studied the degradation kinetics of a-Si:H films grown by dc reactive magnetron sputtering (See Section 2.1). In a previous study we showed that such films include a considerable density of microcrystallites embedded in the amorphous matrix. Evidence for the existence of these microcrystallites in these sputtered samples was first found by Raman spectroscopy.[4] Figure 8 displays a typical Raman spectrum for the sputtered samples used in this part of our study. In this case the crystalline component is clearly discernible and indicates a volume crystalline fraction of roughly 5%. Additional evidence was subsequently obtained using plan-view TEM, which was carried out by Ian Robertson's group at the University of Illinois.[30] An example of the film structure is shown in the bright-field image presented in

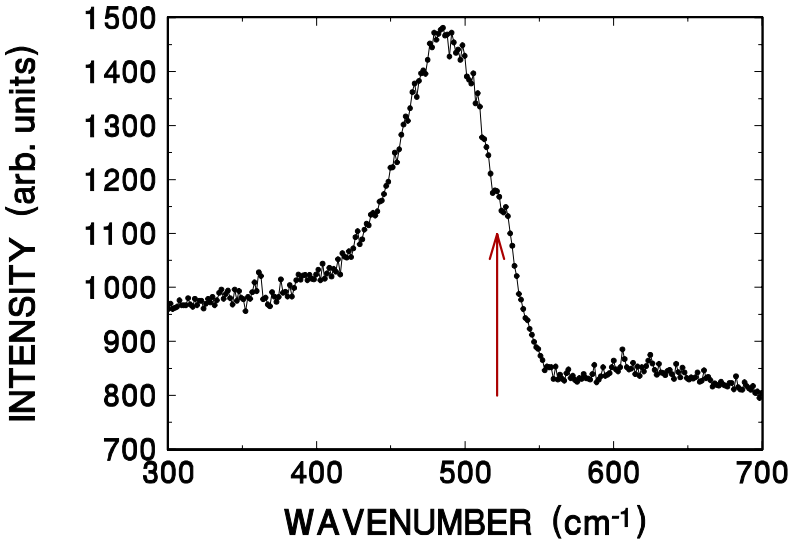

FIG. 8. Raman spectrum for Illinois, dc sputtered sample, (sample 1937) indicating a microcrystalline component at 522 cm^{-1}

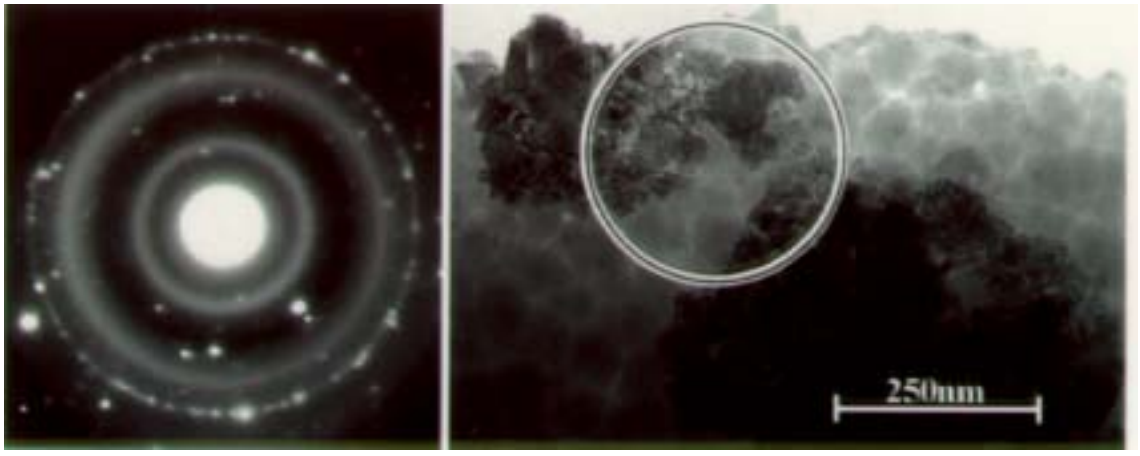

FIG. 9. Bright-field TEM image of Illinois sample 1921 taken from ref. 30. The diffraction pattern from the region circled indicates that the dark regions in the micrograph consist of fine-grained crystalline Si material.

Fig. 9. A selected area diffraction pattern from the region indicated by the circle confirms that the dark regions are actually composed of small crystallites, which give rise to the ring pattern. Dark-field microscopy using a portion of a ring confirmed that small crystallites had agglomerated to form the dark regions shown in Fig. 9. Such images indicate that these films consisted of 5 to 50 nm sized Si crystallites embedded in the amorphous silicon.

An additional and quite sensitive indicator of the presence of microcrystallites in such samples is also obtained from transient photocapacitance spectroscopy (see Section 3.4).

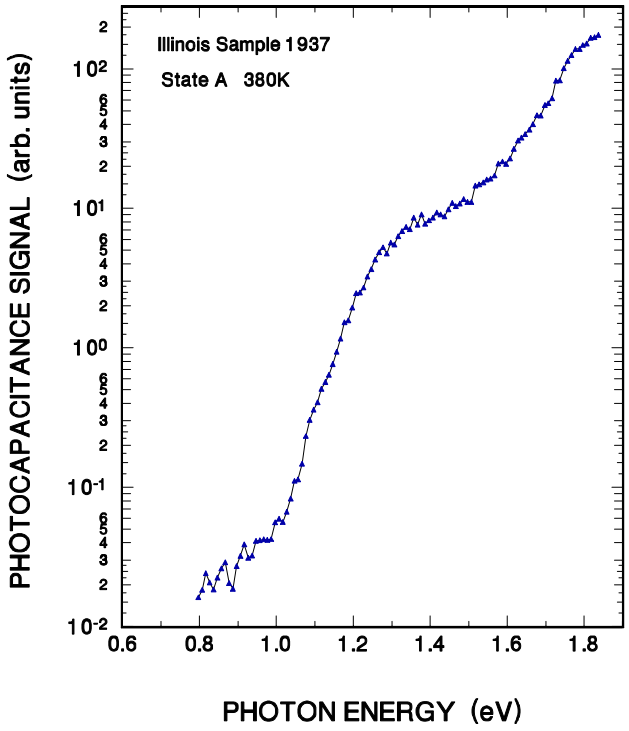

FIG. 10. Photocapacitance spectrum of Illinois sample 1937 showing a "crystalline silicon" feature with an onset close to 1.1 eV. The measurement frequency was 1kHz.

In Fig. 10 we display the photocapacitance spectrum for the sample whose Raman spectrum is shown in Fig. 8. While the Raman evidence for the microcrystalline component in this sample is fairly subtle, the photocapacitance spectra displays a very distinct shoulder in the energy regime between 1.1 and 1.5eV. No such feature has ever been observed for standard glow discharge a-Si:H. Although we have some additional evidence that the strength of this feature scales with the strength of the corresponding Raman crystalline peak [4], the details of such a quantitative analysis are still under investigation. Nevertheless, short of carrying out TEM, we believe that the photocapacitance sub-band-gap spectra may actually provide us with our most sensitive test of the presence of a microcrystalline component in such mixed phase samples. Some of these issues have already been discussed in Section 4.

5.2 BEHAVIOR OF LIGHT INDUCED DEFECT CREATION

In this Section, we demonstrate experimentally that the presence of these microcrystallites gives rise to a very unusual defect creation kinetics. The defect density in each film was determined using the drive-level capacitance profiling (DLCP) method (see Section 3.2), and the Fermi level position was determined through admittance spectroscopy (see Section 3.1). We characterized these samples following periods of light soaking using a tungsten-halogen lamp with a maximal intensity of 4.5 W/cm^2. During light soaking the samples were immersed in methanol, to eliminate any significant increase in surface temperature. The junction capacitance measurements in every case were carried out at temperatures only up to 350K, to avoid thermal annealing of the metastable defects.

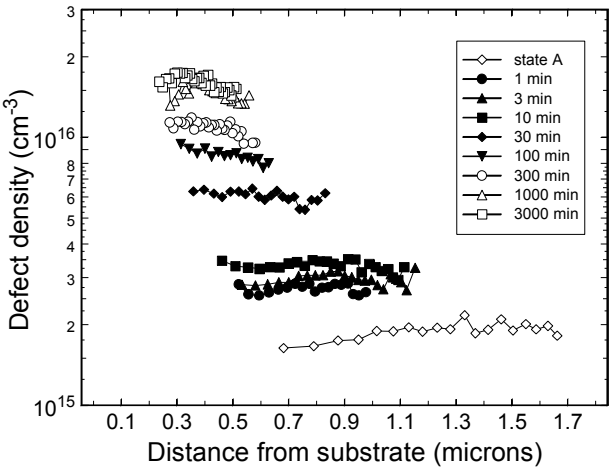

FIG. 11(a). Drive-level capacitance profiles obtained at various stages of light soaking with an intensity of 4.5 W/cm^2. The measurements were carried out at 350K at a frequency of 11 Hz, using the substrate, p$^+$n, junction.

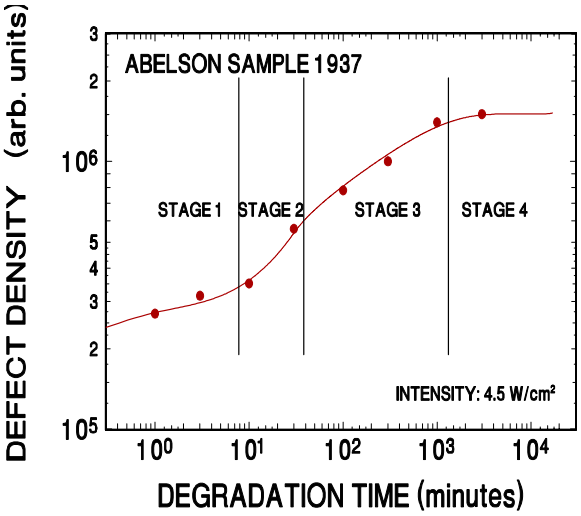

FIG. 11(b). Spatially averaged defect densities vs. light exposure time. The solid line is a guide to the eye. The increase in defect density with time falls into 4 distinct behavioral regimes which we call "stages".

In Fig. 11 we present the results of the DLCP for one sample in various stages of light soaking (from 1 minute to 50 hours). One can see that the profiles obtained are uniform within the experimental accuracy, indicating that the material's properties are independent of the distance from the substrate. To further verify this, we repeated the experiment using the front Schottky diode, and obtained similar results. This figure reveals the unusual degradation kinetics of these a-Si:H films which is made more clear in Fig. 11(b) which presents the spatially averaged defect densities of Fig. 11(a) plotted against the light exposure time. One sees that the defect density increases significantly during the first minute of degradation, and then very slowly until 10 minutes (hereafter called "stage 1"). At this point the defect density increases dramatically in the next time interval (stage 2), and later at a more moderate pace (stage 3) followed by saturation (stage 4). All these results, including the abrupt increase in stage 2, are reproducible and independent of the specific Pd contact used.

Since the DLCP technique measures the integrated density of states between the Fermi energy and a cut-off energy (which is 0.8 eV below the conduction band edge at the temperature and frequency of our measurements), it is important to determine the Fermi level position in the various stages of light soaking. We found that the Fermi energy did not shift during light soaking by more than 0.01 eV. Hence the changes in the measured profiles are directly indicative of the changes in the density of dangling bonds.

The degradation kinetics obtained for different light intensities are displayed in Fig. 12. Here we present the average defect densities obtained through the DLCP technique under three different intensities. We see that most of the features found for the high light intensity are present also in lower intensities. The main differences are that stage 1 becomes even slower as the light intensity decreases, while stage 2 gradually disappears. It is noteworthy that the transition point from stage 1 to stage 2 occurs at longer times and lower defect densities as the light intensity is reduced. The other differences, i.e. the lower overall defect density and the longer times required to achieve saturation under lower light intensity, are well known and generally occur for all a-Si:H samples [31,32].

We also examined the annealing kinetics of our samples. This was done by partially annealing the samples in steps of increasing temperature for 15 minutes at each temperature. In Fig. 13 we present the defect densities as a function of the annealing temperature. The simple curves indicate only a single type of annealing behavior. This indicates that the different steps in the degradation process cannot be explained by appealing to the existence of "fast" and "slow" defects as was previously proposed [33].

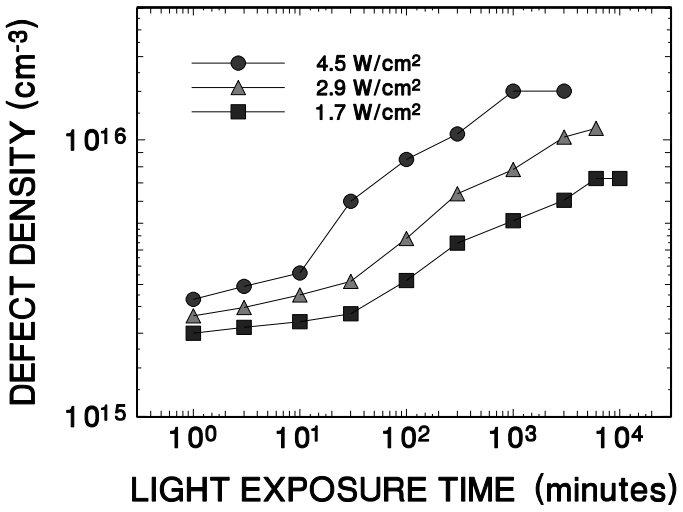

FIG. 12. Defect density as a function of light soaking time for various light intensities. The densities were determined by averaging the drive-level profiles.

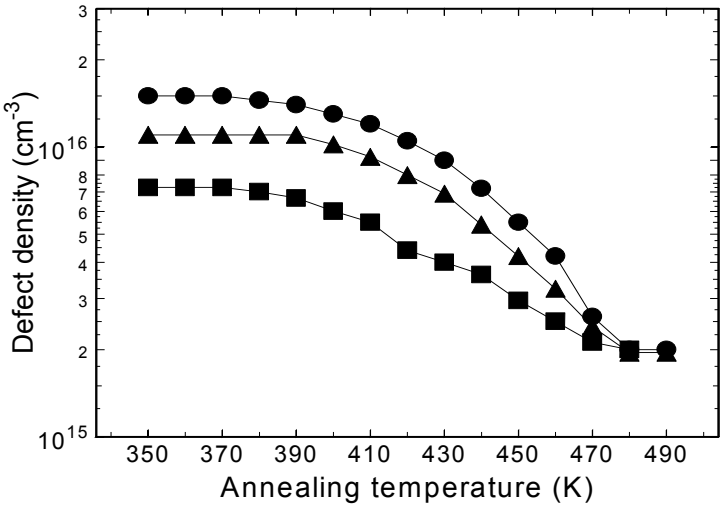

FIG. 13. The defect density as a function of the annealing temperature. These were isochronal anneals at increasing temperature of duration 15 minutes. The lines through the data are to guide the eye.

5.3 MODELING

The most common way to account for the degradation kinetics in a-Si:H is via the rate equation [32]:

$$\frac{dN}{dt} = \frac{c_{SW} G^2}{N^2} - \lambda f(G,N) N , \qquad (5)$$

where N is the density of the dangling bond defects and G is the light intensity. The coefficients C_{SW} and λ determine the rates of the light induced defect creation and annealing processes, respectively. We assume that light induced annealing process is initiated via the capture of one type of carrier into the metastable defects, and thus we take f(G,N) = G/N. This equation neglects any thermal processes, but this is a good approximation since the light soaking was carried out at temperatures which did not greatly exceed room temperature. When the light induced annealing term is negligible, the solution of the rate equation is:

$$N^3(t) - N^3(0) = 3C_{SW} G^2 t , \qquad (6)$$

so that, once the defect density significantly higher than the initial density, one obtains the well known $t^{1/3}$ rule. Indeed, a more accurate way of examining the validity of the model described by equation (5) is to plot the data according to the left hand side of equation (6), and to look for a linear relation with time. This way of presenting these data is displayed in Fig. 14. Here one can clearly see that in the short times region the experimental data definitely do *not* fit a $t^{1/3}$ dependence.

Thus stage 1 indeed represents an anomalously slow degradation not merely been masked by a high initial defect density. This means that the unusual degradation kinetics found here for amorphous silicon samples that contain microcrystallites cannot be fully accounted for by the usual kinetics of degradation even if we add in a constant component of non-degrading states

associated with the microcrystallites. On the other hand, the later time regimes denoted above as stages 3 and 4 are reasonably consistent with the model represented by equation (5).

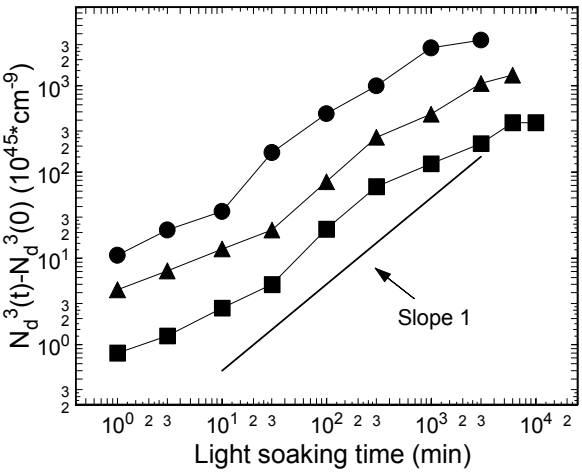

FIG. 14. The third power of the defect density as a function of light soaking time. We have subtracted the contribution of the defects in State A. By comparing the experimental results with a line of slope 1, one can clearly see that the results follow a linear fit only in stage 3 of the degradation.

We therefore suggest that the simplest model that can account for the entire degradation kinetics is of a material which contains three phases. The first phase is high quality amorphous silicon. The second phase is a more disordered type of a-Si:H, believed to lie adjacent to the microcrystallites. The higher degree of disorder of this second phase might be due either to extra stress caused by the presence of the microcrystallites, or to a deficit of diffusing hydrogen which is able to passivate a larger fraction of the bulk defect states. The third phase are the microcrystallites, which provide only a constant, non-degrading, contribution to the defect density. In actual practice, however, we have found that this last contribution to the total defect density can be neglected. The total defect density will thus be given by $f_1N_1+f_2N_2$ where N_i and f_i are the defect density and the effective volume fraction of the i^{th} phase, respectively. Since the second phase is assumed to be much more defective we start with $N_2 >> N_1$, but we also know that $f_2 << f_1$. That is, the Raman spectra and TEM micrographs indicate that the vast majority of the film consists of high quality amorphous silicon.

Turning to the degradation kinetics, we assume that N_2 degrades like equation (5). However, due to the high initial defect density of this phase, the light induced annealing term in this equation will be significant even for short light soaking times. Furthermore, because this phase is highly defective, the corresponding coefficients C_{SW} and λ have relatively high values. For Phase 1 we assume that initially the recombination is governed not by the dangling bonds within this phase, but by defect states within Phase 2 into which the carrier can diffuse and recombine. We denote the effective density of these centers by Z so that we can represent the lifetime for the charge carriers in Phase 1 as proportional to G/Z. This means that the rate equation for the degradation of Phase 1 in the early time regime will read:

$$\frac{dN}{dt} = \frac{c_{SW}^{*} G^2}{Z^2} - \lambda * \frac{G}{Z} N_1 \qquad (7)$$

where C^*_{SW} and λ^* denote the light induced defect creation and annealing coefficients for this phase. Note that the value of Z will depend on the light intensity used in the degradation because the position of the quasi Fermi level will alter the proportion of such states that are acting as recombination centers.

As the dangling bond density begins to increase, it will shift the quasi Fermi level towards midgap, but will not initially alter the free carrier lifetime since the collapse of the quasi Fermi level will simply deactivate an equal number of the Z states. However, once the density of the dangling bonds is high enough to deactivate *all* of the Z states the recombination kinetics will become "normal" again:

$$\frac{dN}{dt} = \frac{c^*_{SW} G^2}{N_1^2} - \lambda^* \frac{G}{N_1} N_1 \tag{8}$$

We note that equation (7) leads to a relatively fast initial degradation of Phase 1, one which is *linear* with time. On the other hand, once the N_1 deep defects dominate the overall recombination the degradation will follow the "normal" $t^{1/3}$ rule.

In Fig. 15 the fit lines indicate that this model can indeed account for all the features of our data. In the first stage of degradation, because the overall defect density is controlled by the contribution of Phase 2 which is high, the light induced annealing term makes the degradation kinetics slower than usual. Then, as the 1st phase defect density starts to grow (initially linearly in time) the total grows very rapidly. Shortly thereafter, this phase totally dominates the carrier recombination processes so that the degradation kinetics is controlled by the defects in this phase. The defect density dependence then rolls over into the "normal" $t^{1/3}$ behavior and ultimately saturates.

Although it may seem that this model contains a large number of free parameters, the only change we have made to between the fits for the different light intensities shown in Fig. 15(a) was in the density parameter Z. This is to account for the number of activated Z defects needed as recombination centers to balance the carrier generation rate. (Of course, we also changed the value of G to match the experimental light intensities.) This analysis indicates that Phase 1 accounts for 95% of the total and Phase 2 for only 5%. For Phase I we found fairly typical values of $C^*_{SW} = 0.0013$ $cm^{-3}sec$ and $\lambda^* = 3\times10^{-13}$, while the corresponding values for the defective second phase were determined to be about 1000 times higher.

While the above fits to the experimental data are quite satisfactory, we also see that the dependence of the saturated defect density on the light intensity of these fits is not as strong as in the experiment. We can improve this if we allow C^* to be slightly dependent on G. In this case

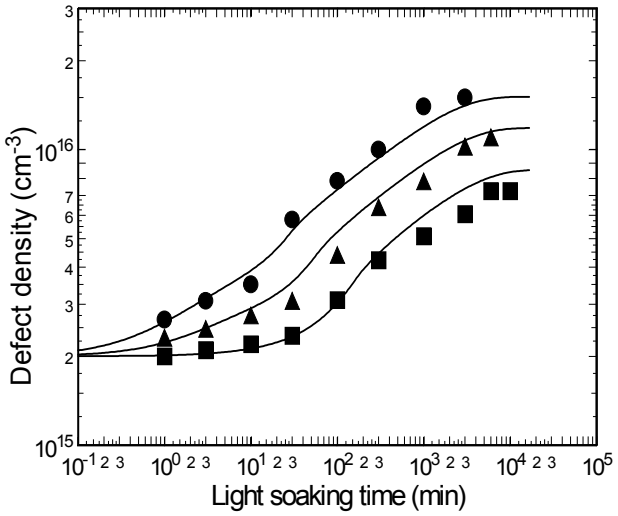

FIG. 15(a). Defect density vs. light soaking time: experiment and model. For these fits the only parameter adjusted to match the data for the different light exposure intensities was the Z concentration.

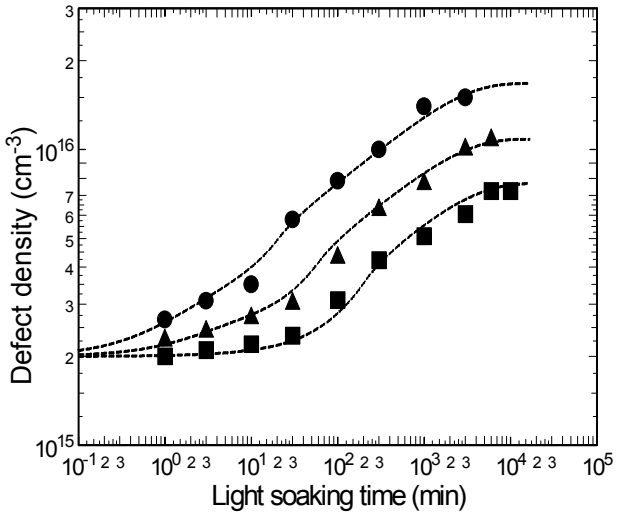

FIG. 15(b). Defect density vs. light soaking time: experiment and model. These some-what better fits also allowed the creation coefficient C^*_{SW} to become slightly intensity dependent.

we obtain the superior fits indicated by the curves in Fig. 15(b). These fits indicate that C* increased by 40% as the light intensity was changed by a factor of 2.8. Such a variation in the creation coefficient C^* might be explained by the existence of potential fluctuations in the Phase 1 such that a larger generation rate would allow the photocarriers to overcome these fluctuations, leading to an increase in the bi-molecular recombination rate.

More of the details of the modeling have been reported elsewhere [34,35]. We stress that the special kinetics reported here is not limited to sputtered a-Si:H samples. We have recently observed similar kinetics in some glow discharge a-Si:H samples grown under H dilution [36]. An unusually slow degradation in H diluted material has also been previously reported based on studies using the CPM technique [37]. This argues against the possibility that the results reported here are due to peculiar aspects of the DLCP technique. Indeed, it is now well known [38] that one of the effects of such dilution is the introduction of a small fraction of microcrystallites into the amorphous silicon matrix.

6.0 CHARACTERIZATION OF HIGH GROWTH RATE a-Si:H MATERIAL

Considerable recent effort has been devoted to obtain hydrogenated amorphous silicon (a-Si:H) films that are grown at high deposition rates but contain a low defect density after light soaking. The most stable cells deposited by plasma decomposition of pure silane diluted in H_2 exhibit growth rates in the vicinity of 1Å/sec which significantly limits the device fabrication rate. Thus a variety of modified deposition techniques are being explored to try to increase the growth rate while maintaining low stabilized defect densities and cell efficiencies. In this Section we report results for higher growth rate a-Si:H films obtained from four different outside laboratories employing a number of different deposition techniques: ETL, BP Solar, United Solar, and NREL. In the last case, we report our evaluation of HWCVD samples produced at ultra-high growth rates, beyond 100Å/s.

6.1 ETL HIGH GROWTH RATE SAMPLES

We first report our results for seven samples of intrinsic a-Si:H films grown by G. Ganguly while he was at ETL using the rf glow discharge technique. Four of these samples were deposited without hydrogen dilution, the remaining 3 samples were diluted in hydrogen using a H_2/SiH_4 ration of 4. The rf power level was varied for each subset of samples to change the growth rate from 2.5Å/sec to 15Å/sec. More details on the growth parameter have been presented in Section 2.2. The deep defect density in these samples was determined by the drive-level capacitance profiling (DLCP) method. We also recorded the sub-band-gap optical absorption spectra using the transient photocapacitance (TPC) technique. Films were characterized in both the dark annealed state (state A), as well as a degraded state produced by exposure to red filtered tungsten halogen light for 100 hours at an intensity of 2.2 W/cm^2 (state B).

In Fig. 16 we plot the defect densities of these samples determined by the DLCP technique, as a function of their growth rate. Closed symbols represent the hydrogen diluted samples whereas the open symbols are for the samples grown from pure silane. For the non-diluted samples one observes that the defect density decreases as the growth rate decreases. However, for the samples grown using hydrogen dilution the defect density exhibits a shallow minimum at the relatively high growth rate of 10.5 Å/sec. These trends appear both in state A and state B. Furthermore, the hydrogen dilution leads to significantly lower defect densities for the samples grown at the higher rates. At the highest growth rate one obtains an almost identical reduction of the defect density by increasing the silane pressure instead of using the dilution with hydrogen. We note that all of the samples exhibit very low overall defect densities. Indeed, the extremely low defect density exhibited by the hydrogen diluted sample deposited at 10 Å/sec represents *one of the lowest defect densities we have ever recorded* for an a-Si:H film using the DLCP method.

For all of the ETL samples, films were deposited on p^+ c-Si and a matching set of films, 7000 to 8000Å thick, were grown on n^+ c-Si, and coated with semitransparent (50%) Ni contacts to form *Schottky diode* solar cells. The fill factors (FF) of these relatively thick devices were expected to be more representative of the bulk material. The FFs were recorded in the annealed state and in the light soaked state (obtained by 6 hours of light soaking using 3 suns at 60°C).

Figure 17 displays the fill factors of such solar cells as a function of the corresponding defect densities of the intrinsic films. We do indeed observe a correlation between a low defect density and a high FF. While the FF values do not appear to be particularly high, this is primarily because the thicknesses (7000 - 8000Å) are far in excess of those used in standard devices (2000 - 3000Å). We also note that because the films and devices were degraded under different conditions, we should probably not expect too good a match in any case. Nonetheless, while there is a large degree of scatter in the dependence of fill factor on the measured defect density, there is actually a much more consistent correlation between samples and devices before and

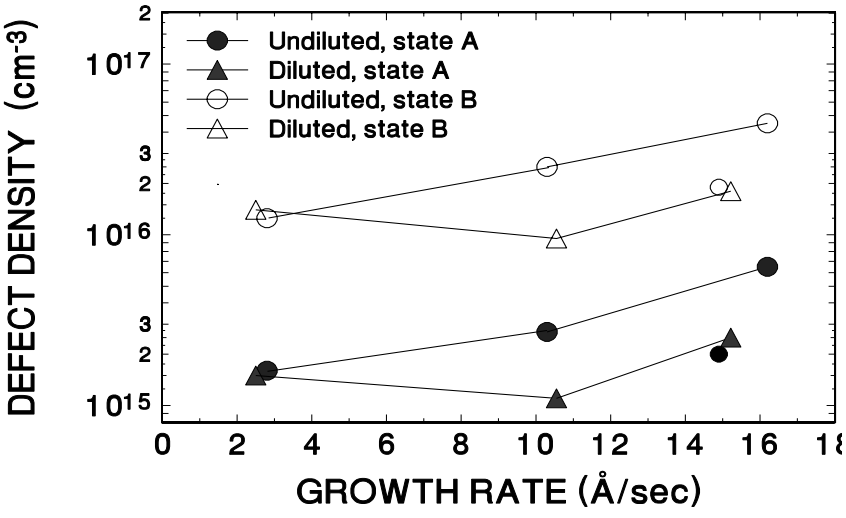

FIG. 16. Deep defect density for the ETL a-Si:H films in both their dark annealed state A, and a light degraded state B. In this case the defect densities shown are twice the drive-level densities obtained at 360K and 11Hz. Note that the undiluted film deposited at higher SiH_4 pressure (small circles) closely matches the diluted sample data for the same total chamber pressure.

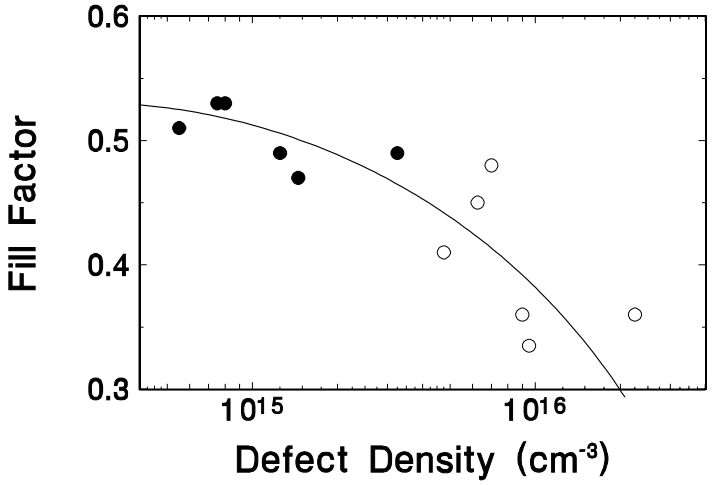

FIG. 17. The Fill Factor of solar cells as a function of the DLCP defect densities in the corresponding ETL intrinsic films. The closed and open symbols represent the annealed and light soaked states, respectively. The line is plotted to guide the eye.

after degradation. This indicates that there is roughly a 0.1 drop in FF when the defect density increases an order of magnitude, provided that the initial defect density is above about 1 x 10^{15} cm^{-3}. For smaller initial defect densities we believe that other factors, instead of the defect density, dominate the FFs in these devices.

We also studied the detailed degradation kinetics versus exposure time for several of these samples. In Fig. 18 we display the results for sample 12468: grown at a power level of 20 Watts under hydrogen dilution. These results indicate that, apart from the very low level of degradation, there is nothing unusual about the degradation kinetics compared to standard glow discharge a-Si:H samples. That is, a nearly perfect $t^{1/3}$ bimolecular dependence on light exposure time is clearly evident once the annealed (state A) defect density has been subtracted.

On the other hand, the sub-band-gap spectrum for this sample, displayed in Fig. 19, indicates a small component of Si microcrystallites (see Section 4.1 above). This is consistent with previous studies indicating that the most stable a-Si:H films grown under hydrogen dilution

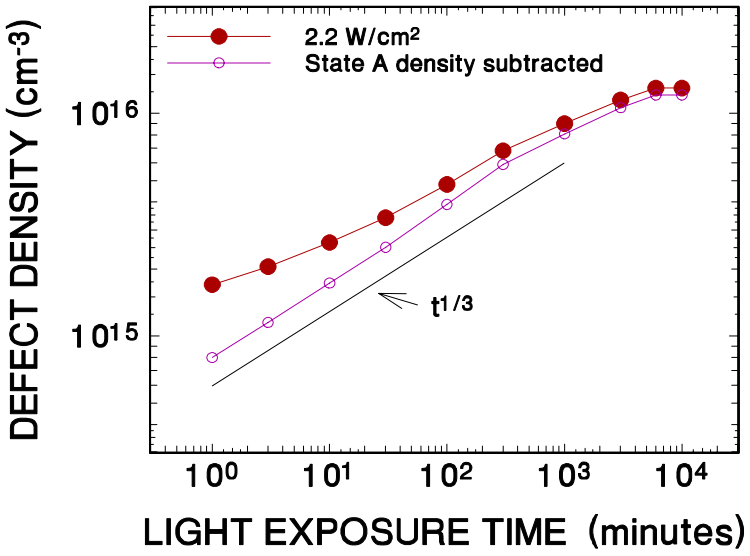

FIG. 18. Deep defect density vs. light exposure (using an intensity of 2.2 W/cm^2) for a-Si:H sample 12468 grown under hydrogen dilution. If we subtract the defect density in state A, the defect density exhibits a nearly perfect $t^{1/3}$ dependence on exposure time.

contain a small microcrystalline component. However, in contrast to the Illinois sputtered samples (Section 4.2), this crystalline component does not give rise to any unusual degradation kinetics. This seems to indicate crystallites that have a markedly different size distribution or morphology.

The degree of microcrystallinity indicated by the sub-band-gap spectra for all of the samples in this series deposited under hydrogen dilution appear very similar to that shown in Fig. 19. However, in Fig. 20 we compare the sub-band-gap spectra for the series of the 3 *undiluted* films deposited under a 20 mTorr chamber pressure. Here we observe a systematic apparent *increase* in the microcrystalline "shoulder" as the growth rate is *decreased* from 16 Å/sec to 2.8 Å/s.

We conclude this Section by briefly considering the how the varying growth conditions of these ETL samples may be affecting the degree of microcrystallinity. It has been argued that the formation of microcrystallites depends on the ratio of H atoms to SiH_3 radicals, with higher values promoting the formation of microcrystallites [39]. Hydrogen atoms, which originate from the dissociation of the silane molecules, collide and react with other silane molecules. This leads to the formation of more SiH_3 radicals accompanied by H_2 molecules [40]. Accordingly, at low silane partial pressures the ratio of H/SiH_3 is high so that the formation of microcrystallites is promoted. When the power is increased, H-ion bombardment energies increase and inhibit the

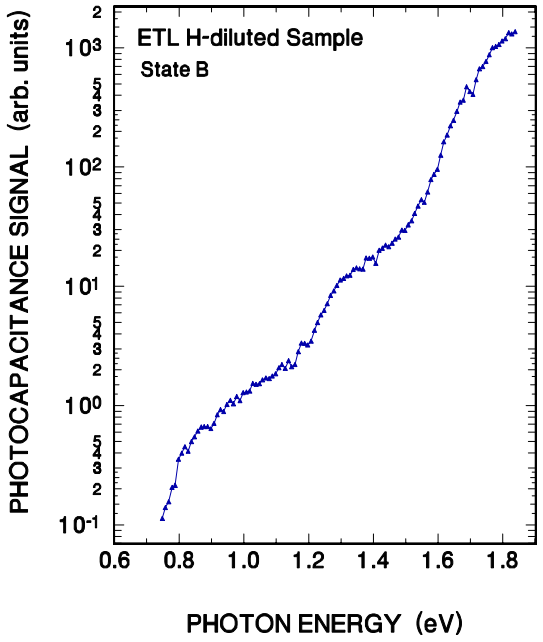

FIG. 19. Sub-band-gap, photocapacitance spectrum of the hydrogen diluted sample 12468 showing a feature with an onset close to 1.1 eV believed to be due to a small component of silicon microcrystallites.

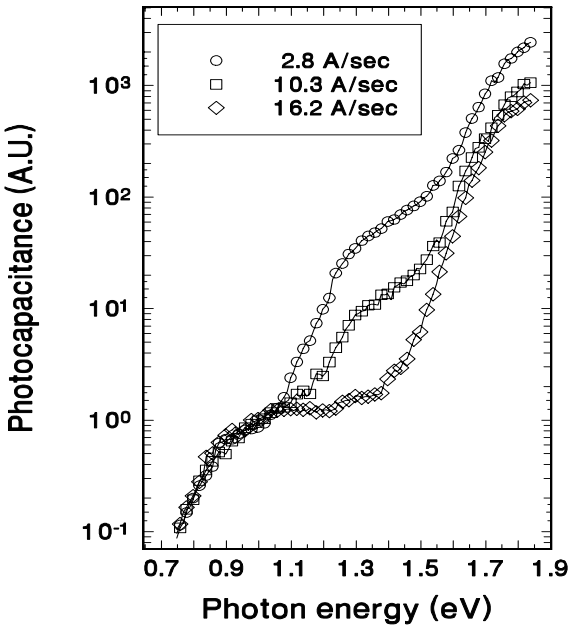

FIG 20. Photocapacitance spectra for the ETL non diluted samples. The data is for all samples in state B, and was recorded at 380K. The microcrystalline shoulder is observed to increase as the growth rate is decreased.

growth of microcrystallites [39]. When H_2 is added while maintaining a low silane partial pressure, additional H atoms are formed from the dissociation of H_2 which itself does not react with H atoms, and results in higher H/SiH_3 ratios. This is reflected in the higher microcrystalline inclusion in the diluted samples.

6.2 BP SOLAR HIGH GROWTH RATE AMORPHOUS SILICON

In collaboration with Gautam Ganguly at BP Solar we have been examining the properties of DC glow discharge i-layer a-Si:H films deposited using different levels of hydrogen dilution and growth rates. This study specifically attempts to correlate film properties with

matched device performance. The materials properties measured at the University of Oregon include the deep defect densities, electrical conductivities, and sub-band-gap photocapacitance spectra. The cell parameters were measured by Dr. Ganguly at BP Solar.

As described in Section 2.4 above, this series of BP Solar samples were deposited varying two of the external deposition parameters; the hydrogen dilution of silane and the plasma power. The pressure was kept constant. In this manner the deposition rate varied from 0.65 to 6Å/s. These i-layer films were 1 to 2.5μm thick. Matched solar cell devices were fabricated in a glass/SnO_2/p/i/n/ZnO/Al structure using the identical series of growth conditions. For the devices the i-layer thickness was kept close to 0.25μm.

For the materials characterization of the films, semi-transparent Pd dots (area 0.88 mm^2) were evaporated to form Schottky barrier contacts. Both the films and devices were characterized in their as-grown state (State A) and in a light-degraded state (State B). The light-degraded state was obtained by illuminating the films and devices for 100 hours using the same red-filtered ELH light source at an intensity of 100 mW/cm^2. In degrading the films we were careful to compensate for the partial transparency of the Pd contacts. Cell performance parameters (open circuit voltages, V_{OC}; short-circuit current densities, J_{SC}; fill factors, FF; and cell efficiencies, Eff) were determined in both states A and B. These results for the cell parameters are listed in Table V. The cell parameters, particularly in State B, exhibit a clear deterioration in properties as the growth rate is increased. This is nicely illustrated in Fig. 21 in which we plot the state B cell efficiency dependence on growth rate for this set of samples.

Drive-level capacitance profiling was used to determine the deep defect densities in both the as-grown and degraded states. In contrast to the cell performance, we observed essentially no clear correlation between the defect densities in these samples with deposition rate. This is clearly illustrated in Fig. 22.

As these studies began to progress we began to wonder whether there might be distinct differences between the properties of films deposited onto different substrates. BP Solar normally employs superstrate cells and so we have been examining films deposited onto glass/

Table V. Device performance parameters before (state A) and after (state B) light soaking.

Sample	**Condition**	**R Å/sec**	**State A**				**State B**			
			FF	Voc	Jsc	Eff	FF	Voc	Jsc	Eff
42-1	C, 2D	0.65	0.72	0.9	10.53	6.9	0.63	0.89	9.68	5.38
A9124-1	C, D	1.0	0.69	0.89	11.39	7.0	0.59	0.88	10.3	5.33
66-1	C, D/2	1.5	0.72	0.89	11.82	7.6	0.57	0.85	10.4	5.01
A9140-3	5C, D	3.0	0.69	0.9	9.95	6.2	0.58	0.88	8.96	4.57
67-2	5C, 2D	3.7	0.6	0.89	9.98	5.4	0.53	0.89	8.99	4.24
66-2	5C, D/2	6.0	0.69	0.91	9.61	6.0	0.48	0.86	7.97	3.28

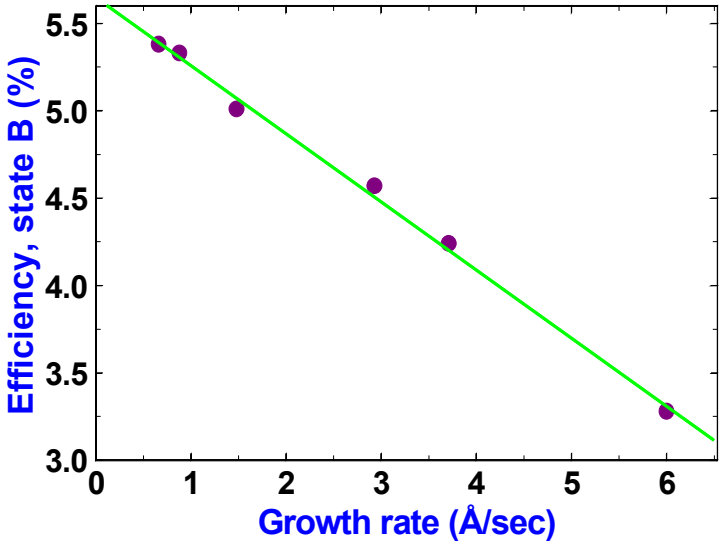

FIG. 21. Cell efficiency dependence on growth rate for BP Solar samples in state B indicating a loss of performance as deposition rate is increased.

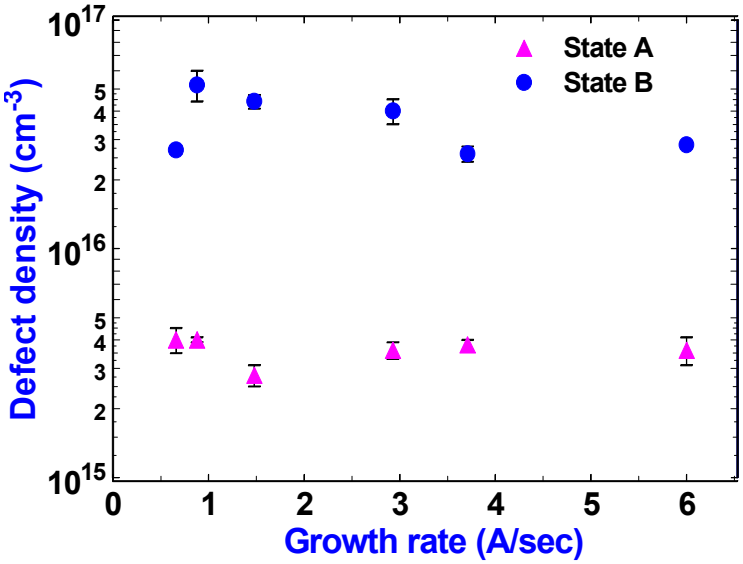

FIG. 22. Deep defect densities as a function of growth rate for six BP Solar films. The defect densities were determined by the drive-level capacitance profiling (DLCP) method, and the error bars indicate the range of spatial variation exhibited by the measured profiles. Note the lack of any clear correlation between deep defect densities and growth rate.

TCO substrates. However, we often obtain films deposited onto heavily doped crystalline silicon substrates so that we can carry out a broader range of our measurement techniques. Some questions have been raised, however, whether such differences in substrates might affect the intrinsic properties of a-Si:H films. Therefore we decided this was a good opportunity to examine a film deposited simultaneously onto two different substrates: glass/TCO and doped c-Si.

The two samples were studied using admittance measurements and DLCP in both their dark annealed state and a light degraded state obtained after 100h exposure to red-filtered ELH light at an intensity of 1W/cm^2. The DLCP profiles were obtained at 11Hz and two measurement temperatures: 350K and 360K. These profiles are displayed in Figs. 23 and 24.

It is important to recall that the DLCP density reflects an integral over the density of states between the Fermi energy and a cutoff energy proportional to the measurement temperature [see Eq. (3)]. Therefore, the *difference* between the profiles for the two temperatures reflects the magnitude of the density of states in that energy range (near roughly 0.85eV below E_C). In addition, it has previous been shown from comparison studies between DLCP with ESR in matched samples [12], that by doubling the 11Hz, 360K profile density a good estimate of the total density of deep defects is obtained.

One can see in Fig. 23 that, for the annealed state, there appears to be a somewhat significant difference for results on the 2 substrates. However, the difference is most severe at low applied DC bias (lower distances) and so the higher values for the c-Si substrate sample in this regime is most likely an artifact due to a poorer ohmic back contact in that case. A larger apparent defect density can then occur because, near zero bias with two blocking junctions, the capacitance will be due to two depletion regions in series. This situation will distort the normal C *vs*. V dependence, causing C to change less rapidly with voltage (either the DC bias or the alternating voltage amplitude) and thus indicate an erroneously higher density. Once the applied bias exceeds about 1V, this type of problem essentially goes away since then one junction is sufficiently forward biased to disappear from the measurement. Indeed, at higher DC bias (higher distances) the two profiles agree reasonably well except that the c-Si sample is offset slightly to a higher profile value. Since the difference between the profiles at the two temperatures is nearly identical, however, this indicates a nearly identical density of states.

On the other hand, for state B (Fig. 24) the results for the two samples are, to within the experimental uncertainty, *absolutely identical*. This is certainly reassuring since it indicates that the substrate is not affecting the deep defect density, at least once the film is a couple thousand angstroms thick. However, there is one slightly mysterious aspect. In measuring the AC admittance of both samples in state B, we found a significantly different activation energy of conductance: 0.752eV for the c-Si substrate vs. 0.805eV for the glass/TCO. Our results in this regard seem very clear. Thus, there may indeed be subtle differences in the electronic properties of these two samples; however, these are probably not significantly enough to affect the conclusions drawn in this report.

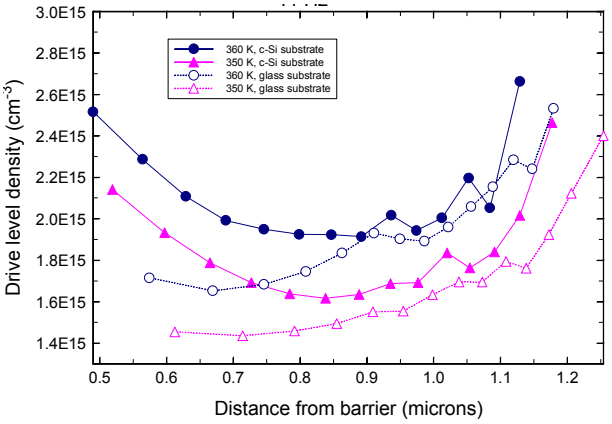

FIG. 23. Drive-level capacitance profiles in the *dark anneal state* for BP Solar film deposited on two substrates: glass/TCO and crystalline Si. Measurements were taken at 11Hz and at two different measurement temperatures as indicated. The profile distance is relative to a top Pd Schottky contact.

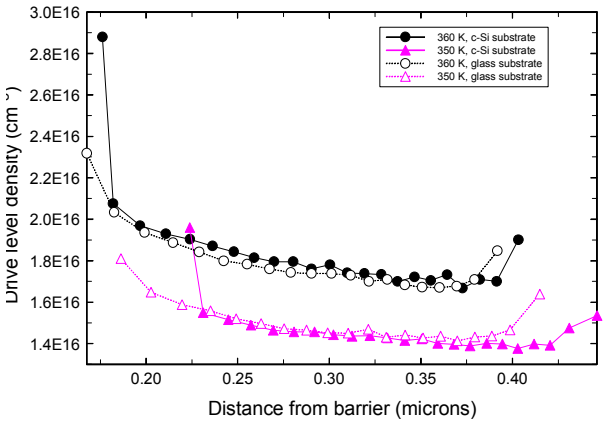

FIG. 24. Drive-level capacitance profiles in the *light degraded state* for BP Solar film deposited on the two substrates. The other measurement parameters are the same as listed for Fig. 23. Note the nearly identical deep defect profiles for the films deposited onto the two different substrates.

Since the deep defect densities do not appear to be correlated to the corresponding cell performance, we extended our characterization using the techniques of transient photocapacitance (TPC) and transient photocurrent (TPI) spectroscopies as described in Section 3.4. Such spectra provide us with a measurement of the Urbach tail width and an independent assessment of the relative deep defect density. Moreover, as we have discussed previously [23], a comparison of the TPC and TPI also provides information about the hole $\mu\tau$ products in these films. Examples of such spectra for two BP Solar films deposited at the extremes of growth rates for this set of samples are displayed in Figs. 25 and 26.

In comparing the two sets of spectra for the lowest and highest growth rate samples (in their light-degraded states) one notes the following differences: (1) A significantly narrower bandtail (lower Urbach energy) for the low growth rate sample compared to the high growth rate sample; (2) A larger deep defect band for the high growth rate sample, in spite of the fact that the DLCP measurements indicated defect bands of more nearly equal magnitude; (3) A larger difference between the photocapacitance and photocurrent in the bandtail region for the low growth rate sample. This indicates a larger probability that the minority carrier (hole) can escape the depletion region before being deep trapped, and thus indicates a larger hole $\mu\tau$ product for the low growth rate sample compared to the high growth rate sample.

In Table VI we list the parameters obtained from the fits to the photocapacitance and photocurrent sub-band-gap spectra for all 6 films; specifically, the Urbach energies, an estimate of the defect band magnitude (as deduced from the transient photocurrent spectra), and the ratio of the photocurrent to photocapacitance spectra magnitudes in the bandtail region once the two

spectra have been aligned at the lowest optical energies. This last quantity is directly related to the hole μτ product; that is, a higher ratio generally indicates a higher μτ product.

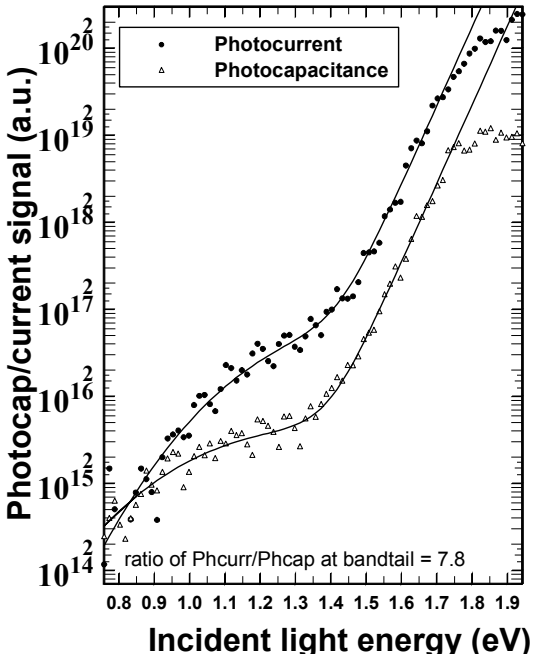

FIG. 25. Transient photocapacitance and photocurrent spectra for the lowest deposition rate sample (0.7Å/sec).

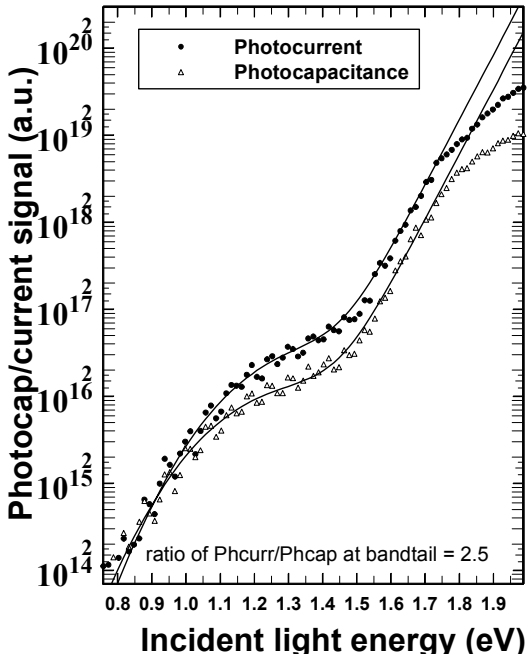

FIG. 26. Transient photocapacitance and photocurrent spectra for the highest deposition rate sample (6Å/sec).

TABLE VI. Summary of BP Solar film parameters determined from photocapacitance and photocurrent sub-band-gap spectra. The deep defect band magnitude and the ratio of the photocurrent to photocapacitance signals in the bandtail region are listed for the degraded state of each film. The companion device fill factors are also listed for reference in the degraded state. (Note that D,C,P for "growth conditions" indicate the reference hydrogen dilution, discharge power, and chamber pressure values, so that "2D" indicates twice the hydrogen dilution level, etc.)

Sample No.	Growth Rate (Å/s)	Growth Conditions	Matched Cell Fill Factor	E_U (meV)	Defect Band (arb. units)	Phcur/phcap Tail Ratio
42-1	0.66	2D,C,P	0.63	48	1.4	7.8
9124-1	0.88	D,C,P	0.59	50	1.9	3.5
66-1	1.5	D/2,C,P	0.57	52	1.4	2
9140-3	2.9	D,5C,P	0.58	57	1.5	2.8
67-2	3.7	2D,5C,P	0.53	55	4.6	3.5
66-2	6.0	D/2,5C,P	0.48	58	8.9	2.5

In the Table one observes a couple of clear trends: The previously noted decrease in fill factors with increasing deposition rate is apparent, as well as an increasing value of Urbach energy with increasing deposition rate. The defect band magnitudes and bandtail ratios, on the other hand, are not so clearly correlated with either deposition rate or device fill factors. To illustrate the observed correlation with Urbach energies more clearly, we have plotted in Figs. 27(a) and 27(b) the variation of Urbach energies with growth rate, and the variation of matched device fill factor with Urbach energy.

The apparent strong correlation between device fill factor and Urbach energy comes as a bit of a surprise, especially since the hole μτ products deduced from our data are not particularly strongly correlated. However, it does help explain our results from some previous studies in which there appeared to be a much stronger correlation between deep defect densities and device behavior since, in those series of samples, the Urbach energies were more nearly constant.

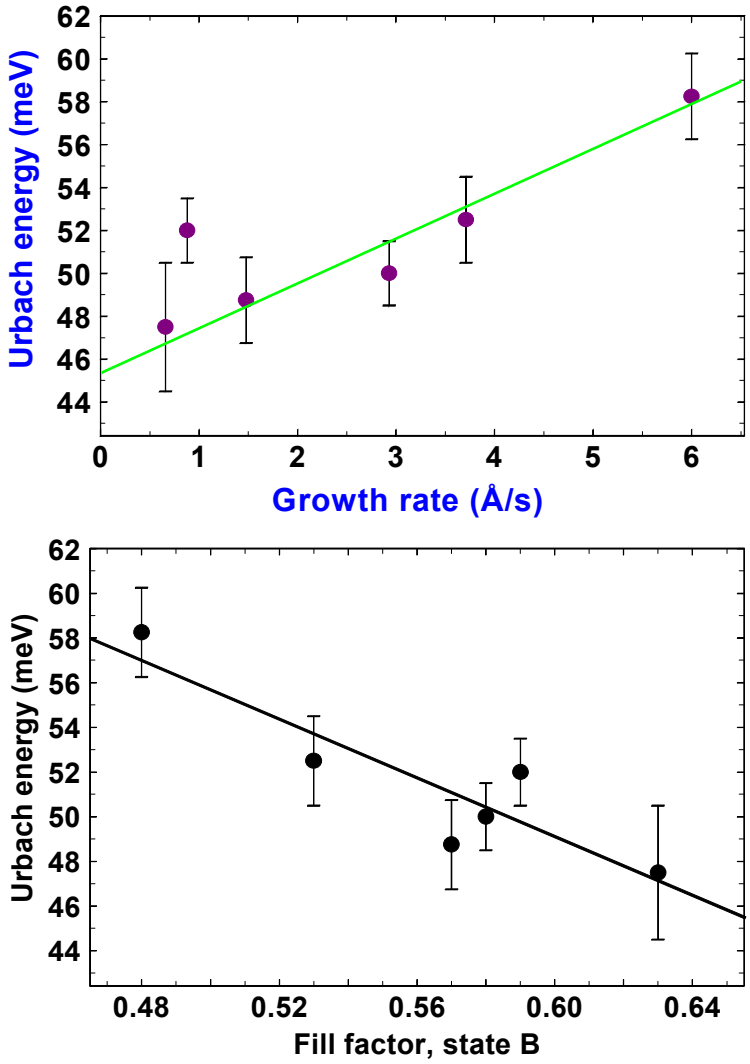

FIG. 27.

(a) Urbach energy vs. growth rate, indicating a fairly strong correlation.

(b) Matched device fill factor in state B vs. Urbach energy, again showing a strong correlation except in the case of sample 9140-3.

6.3 UNITED SOLAR HIGH DEPOSITION RATE a-Si:H FILMS

A preliminary series of three a-Si:H samples was obtained from United Solar. These 3 films had been optimized at their respective growth rates in terms of delivering good performance for photovoltaic p-i-n cells. One film was low growth rate hydrogen diluted material deposited at 1Å/sec. This corresponds to the material that has produced the most stable, highest efficiency devices produced at United Solar. The other two samples were deposited at 3Å/sec and 6Å/sec. The first of these was deposited in a conventional PECVD reactor utilizing modified deposition conditions (higher rf power, etc.), while the second was deposited under VHF conditions using a 70 MHz excitation frequency. Both films were deposited under conditions that have led to the best performing cells reported to date for these higher deposition rates.

Each film was deposited on a stainless steel substrate over a thin contacting layer of n^+ a-Si:H. A Pd Schottky contact was deposited onto the top surface of each sample to enable characterization by our junction capacitance methods. Capacitance vs. frequency and temperature allowed us to determine the thickness of each sample as well as the activation energy of the dark conductivity, E_σ. These quantities are listed in Table VII.

We then carried out drive-level capacitance profiling (DLCP) measurements to assess overall defect density and spatial uniformity of electronic properties. We also carried out transient photocapacitance (TPC) spectroscopy, to document the sub-band-gap spectra and thus, for example, document differences in the Urbach energies or deep defect energy distributions. The above measurements were all carried out for the light-degraded state of these sample which were obtained by an exposure to a red filtered tungsten-halogen source at an intensity of $2W/cm^2$ for 100 hours. These defect densities and Urbach energies have been included in Table VII.

TABLE VII. Properties deduced for United Solar a-Si:H samples of varying deposition rate. All three samples were deposition on n+ a-Si:H coated stainless steel substrates. The thickness and activation energy of conductivity were determined from admittance vs. temperature and frequency measurements, the Urbach energies were determined from the transient photocapacitance spectra (see Fig. 29), and the deep defect densities were determined from the drive-level capacitance profiling measurements (see Fig. 28) for the degraded state of each film.

SAMPLE	Deposition Rate	Thickness	Conductivity Activation Energy (eV)	Urbach Energy (meV)	Deep Defect Density (cm^{-3})
10065	1Å/sec	1.05 μm	0.73	46	1.5×10^{16}
B4345	3Å/sec	1.2 μm	0.77	45	2.5×10^{16}
R7625	6Å/sec	1.05 μm	0.73	48	3.5×10^{16}

A comparison of the drive-level capacitance profiles for all 3 samples in their light-degraded state is shown in Fig. 28. At the measurement frequency and temperature employed, the deep defect density is approximately twice the density given on the vertical axis. One notes that the deep defect density increases markedly as the deposition rate increases, and also that its spatial variation becomes somewhat larger. The sub-band-gap spectra for these three films obtained from the transient photocapacitance measurements are shown in Fig. 29. The three samples exhibit quite similar sub-band-gap spectra. The only significant evidence for poorer

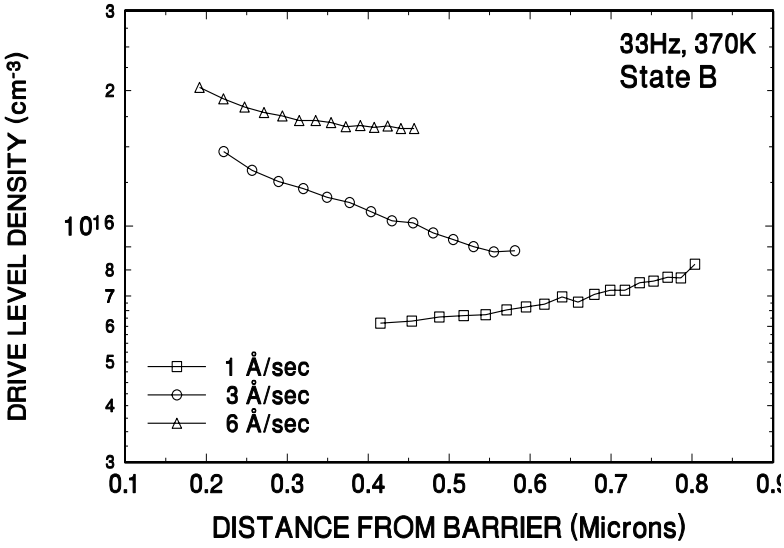

FIG. 28. Drive-level capacitance profiles for three United Solar a-Si:H samples in their light degraded states. These samples were deposited at the three different growth rates indicated using conditions which have led to the best stabilized cell performance obtained at United Solar. The profiles were carried out using a measurement frequency of 33Hz and a temperature of 370K. Under such conditions the total deep defect density is approximately twice that shown on the vertical axis.

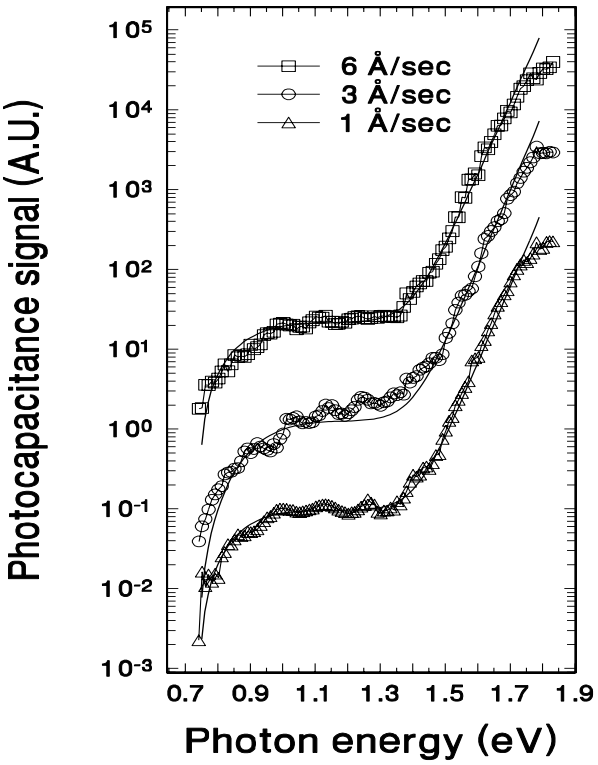

FIG. 29. Sub-band-gap spectra obtained from transient photocapacitance measurements of the three United Solar samples in their light degraded state. The three spectra have been offset vertically for display purposes. The thin solid lines are fits to these spectra used to estimate the deep defect densities and to determine the value of the Urbach energies

film properties at the higher deposition rate material from these spectra is a moderate increase in the deep defect density consistent with that obtained from the DLCP data, and a slightly wider Urbach tail obtained for the film deposited at 6 Å/sec.

We can formulate a few general conclusions of this quite preliminary study of the effects of increased deposition rate on the electronic properties of the United Solar a-Si:H films. Specifically, our measurements do show differences in the electronic properties consistent with poorer device performance; namely, a moderate increase in deep defect density and a slight increase in the width of the Urbach tail. Unfortunately, the current samples do not yet allow us to perform measurements to assess minority carrier transport properties. We are currently planning a more comprehensive series of studies to examine such effects.

6.4 ULTRA-HIGH GROWTH RATE HWCVD AMORPHOUS SILICON

Amorphous silicon films deposited by the hot-wire CVD method have properties quite distinct from glow discharge material. For example, it was previously established that quite good electronic properties could be maintained even when the hydrogen content fell below 2at.%; something that has never been achieved by any other technique. In more recent years scientists at NREL have been pushing up the growth rate of a-Si:H using the HWCVD well beyond the limit of what has been explored with the glow discharge process. Using a multi-filament configuration the NREL growth has demonstrated growth rates exceeding 100Å/s with reportedly acceptable electronic properties.

We characterized two of these NREL ultra-high growth rate films in some detail using both the drive-level capacitance profiling method and transient photocapacitance spectroscopy. More details concerning the samples studied are given in Section 2.4.1. The two samples examined were deposited at 90Å/s and 130Å/s, respectively. In Fig. 30 we display the deep

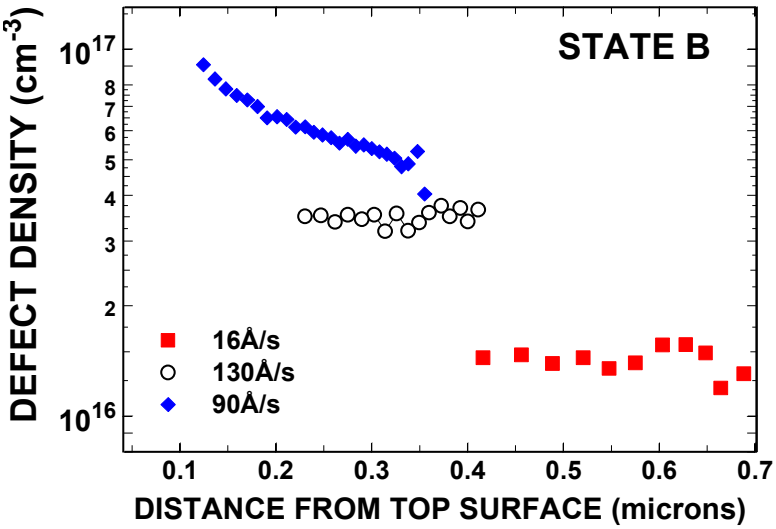

FIG. 30. Drive-level capacitance profiles for three NREL HWCVD films: two ultra-high deposition samples plus a lower deposition rate high quality HWCVD sample for reference. In all cases the samples were examined in a strongly light degraded metastable state.

defect profiles for both these samples together with a much lower deposition rate HWCVD reference sample, all in light degraded states obtained by light soaking for 120 hours at 2W/cm^2 red-filtered light. This lower deposition rate sample has properties quite comparable to the best glow discharge a-Si:H films.

In this figure we observe that the 130Å/s actually appears to have superior properties to the 90Å/s film, both in terms of a lower overall defect density, and in terms of more spatially uniform electronic properties. Moreover, even at this extremely high growth rate the defect density is observed to be within a factor of 2 of the high quality low growth rate sample.

In Fig. 31 we compare the photocapacitance spectra for the same three samples in their light-degraded states. These data confirm that the ultra-high deposition rate samples have quite good electronic properties. The 130Å/s film has a deep defect band that is within a factor of two in magnitude compared to the very high quality low deposition rate reference sample, and the Urbach energy (near 53meV) is also only modestly larger than that of the reference sample. More details concerning the electronic properties of these samples have recently been published [41] including the photoconductivity and some degradation kinetics as determined by our NREL collaborators. We should mention that in cases where defect densities were determined at NREL using DLCP or the CPM technique, there was excellent quantitative agreement.

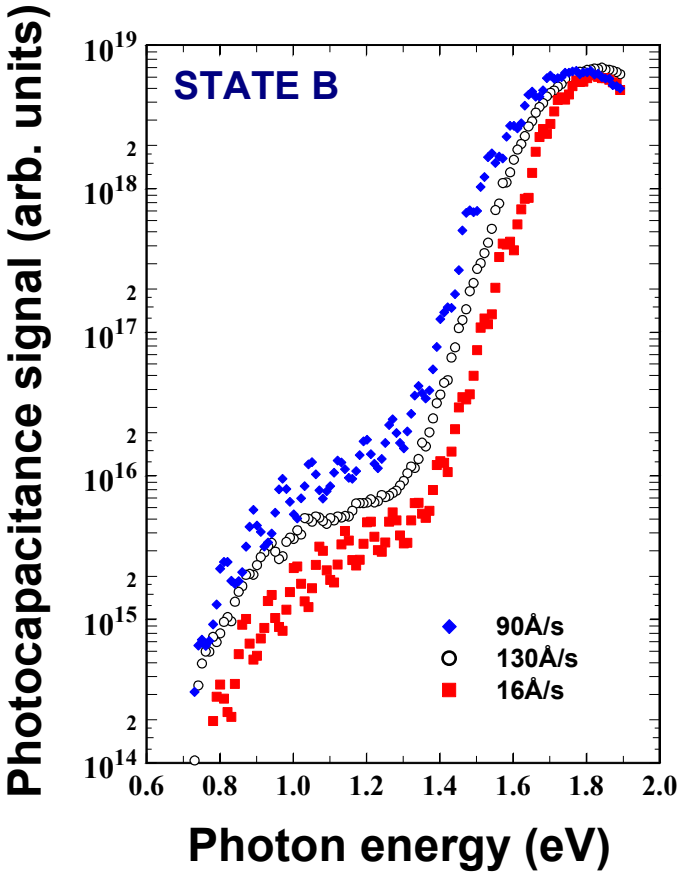

FIG. 31. Transient photo-capacitance spectra for the two NREL ultra-high deposition rate samples together with the lower deposition rate reference sample. The relative magnitudes of the deep defect band generally agree with the DLCP results of Fig. 30. The Urbach energies are comparable (near 53meV) for the two ultra-high deposition rate samples, and somewhat smaller (roughly 45meV) for the lower deposition rate sample.

7.0 AMORPHOUS SILICON-GERMANIUM ALLOY STUDIES

7.1 ELECTRONIC PROPERTIES OF UNITED SOLAR a-Si,Ge:H ALLOYS WITH LOW GERMANIUM CONTENT

Our studies of the a-Si,Ge:H alloys over the past decade under NREL Subcontracts has given us a fairly complete picture of the defect structure for alloys in the "low-gap" range suitable for tandem and triple solar cells; that is, a-$Si_{1-x}Ge_x$:H material with Ge fractions covering $0.25 \le x \le 0.5$. However, such alloys with Ge fractions below 0.2 are also important in photovoltaic applications since they can be utilized as the mid-gap alloy material in triple cells. At Ge fractions above 0.3 there is ample evidence from electron spin resonance (ESR) measurements that Ge dangling bonds dominate the deep defect population.[42] There has also been ESR evidence to suggest that Ge dangling bonds are dominant already at Ge fractions below 0.1 [43]. However, the only studies to date for such low alloy fraction material utilized material that had fairly poor electronic properties by today's standards; in particular, defect densities significantly in excess of 1×10^{16} cm^{-3} in the annealed state. Therefore, a few years ago we began a study of optimized rf glow-discharge intrinsic a-$Si_{1-x}Ge_x$:H alloys grown by United Solar Systems Corporation (United Solar) with low fractions of Ge ($0.02 \le x \le 0.2$).

First of all, we employed the drive level capacitance profiling (DLCP) method to determine the total density of defect states in the material. Samples were characterized in their dark annealed State A as well as a light degraded State B produced by exposure to red-filtered ELH light at an intensity of $1 W/cm^2$ for 100 hours. Examples of such profiles for several samples in state A are displayed in Fig. 32, while the deduced defect densities for all 6 samples for both state A and B are displayed in Fig. 33 as a function of the Ge content. We see that the

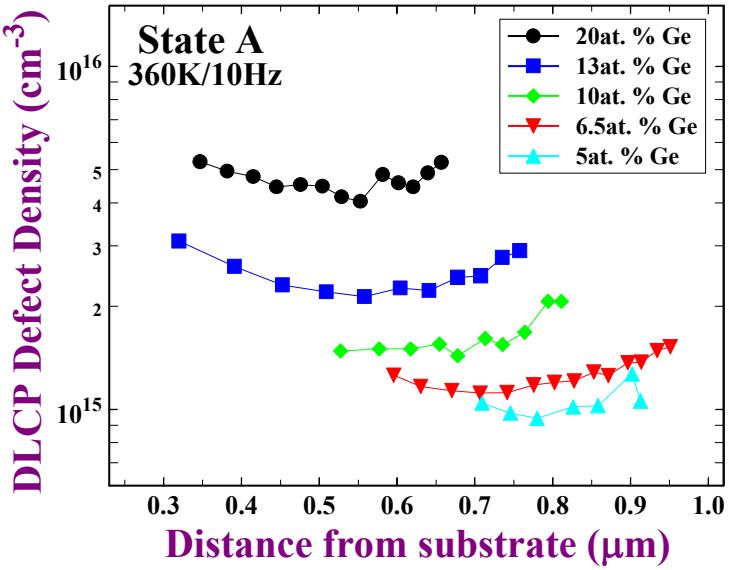

FIG. 32. Drive-level capacitance profiles for five United Solar low Ge fraction a-Si,Ge:H films in state A. A good estimate of the total deep defect densities in these samples is obtained by doubling the average DLCP values obtained under these measurement conditions (360K, 10Hz).

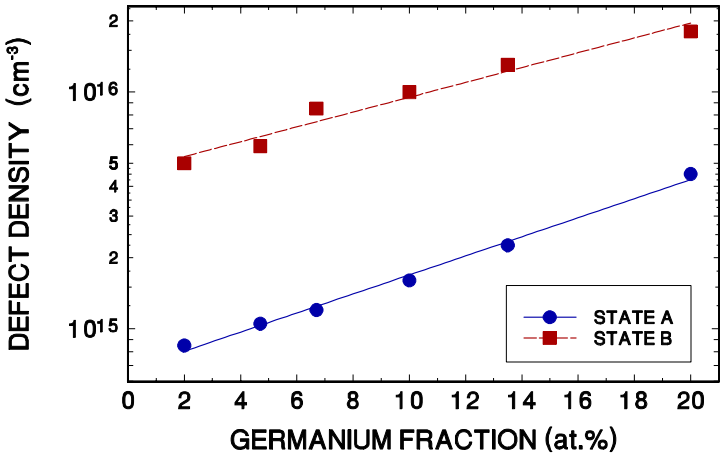

FIG. 33. Defect densities obtained from the DLCP profiles for all six a-Si,Ge:H samples in both state A and state B. Note that the deep defect density increases upon light soaking for every sample. However, the *relative* increase is lower for the films with higher Ge content.

state A defect density was found to increase from around 1 x 10^{15} cm^{-3} to 5 x 10^{15} cm^{-3} with increasing Ge content over this range. These densities are among the lowest ever previously reported for a-Si,Ge:H alloys in this composition range. After light soaking we observed an increase in total defect density for all the samples. However, the relative increase was slightly larger for the samples with smaller fraction of Ge as shown in the figure.

The Fermi energies were determined using admittance measurements. Transient photocapacitance measurements (see Fig. 34) revealed a nearly constant Urbach energies of 45meV to 47meV for all samples. As the Ge content was increased, the optical band gap E_{04} decreased from 1.82eV to 1.70eV, respectively. These results are summarized in Table VIII.

TABLE VIII. Summary of electronic properties of the low Ge fraction films deduced from our experimental studies.

Sample	Ge content (at.%)	State	E_F (eV)	E_{04} (eV) ±20meV	Urbach energy (meV)	Defect Density (10^{15} cm^{-3})	Peak 1 position (eV)	Peak 2 position (eV)
L10570	***2***	***A***	***0.77***	***1.83***	***46***	***0.85***	***0.68***	***0.77***
		B	0.76	--	--	5.0	0.68	0.78
L10567	***5***	***A***	***0.8***	***1.80***	***46***	***1.05***	***0.67***	***0.77***
		B	0.77	--	--	5.9	0.68	0.79
L10569	***6.5***	***A***	***0.78***	***1.79***	***46***	***1.2***	***0.66***	***0.75***
		B	0.75	--	--	8.5	0.69	0.78
L10577	***10***	***A***	***0.79***	***1.76***	***46***	***1.6***	***0.62***	***0.72***
		B	0.77	--	--	10.0	0.68	0.77
L10566	***13.5***	***A***	***0.77***	***1.74***	***47***	***2.25***	***--***	***--***
		B	0.74	--	--	13	--	--
L10608	***20***	***A***	***0.69***	***1.70***	***51***	***4.5***	***0.6***	***0.73***
		B	0.75	--	--	18	0.62	0.75

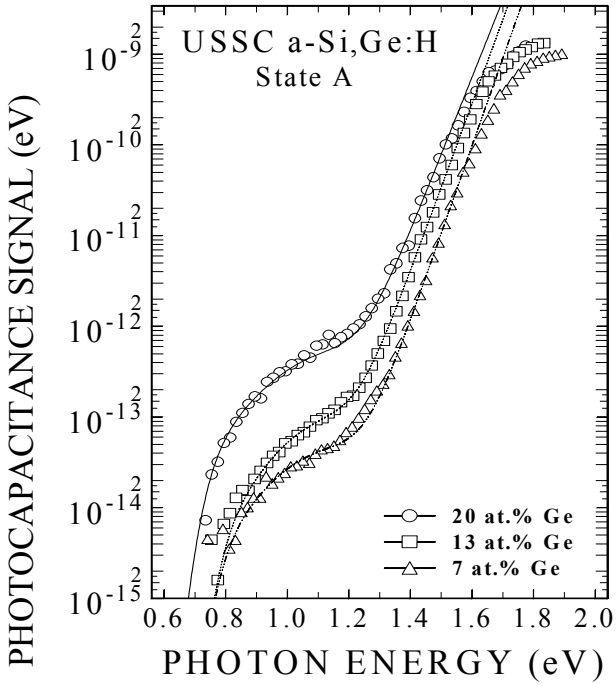

FIG. 34. Photocapacitance spectra for a-Si,Ge:H alloys with different Ge fractions deposited at United Solar. The Urbach energies are nearly independent of Ge fraction, as listed in Table VIII The spectra for the 7 and 13at.% Ge fraction alloys were obtained at 370K, while the 20at.% Ge sample was measured at 360K.

The most intriguing results, however, were obtained using the modulated photocurrent (MPC) method. Unlike MPC measurements performed on pure a-Si:H, which show a single band of defect states [44], our results reveal *two distinct* deep defect bands. Figure 35 shows an annealing study for the 5 at.% Ge content film. In State B one can distinguish clearly between two different bands of deep majority carrier traps located at 0.68eV and 0.79eV below the conduction band. Hereafter, we refer to them as shallow band and deep band, respectively. As the annealing steps proceed, one can see that the magnitude of the shallow band decreases more significantly than the one of the deep band. Many more of the details of the metastable behavior of these samples will be discussed in Section 8. Eventually, in State A the MPC data is dominated by the deep defect band alone. This annealing study was performed for all the samples in this series and exhibited similar behaviors.

We fitted the MPC data using two Gaussian bands. Examples of these fits for the 2at.% sample in states A and B are displayed in Fig. 36. Table VIII summarizes the positions of the peaks of the bands for all the samples. Using the relative magnitudes of the two defect bands obtained from these fits, together with the values of the total defect density obtained from the DLCP measurements, we may estimate the defect densities for each of the defect bands individually for both states A and B. These estimates are plotted in Fig. 37 for the four lowest Ge samples. Note that in each case that the shallow defect density greatly exceeds the deeper defect density in State A, whereas the reverse is true in State B; however, both types of defects increase with light soaking. It is also interesting to note that both types of defects increase monotonically with increasing Ge content in the films.

FIG. 35. MPC spectra for a sequence of anneal states for the 5at.% a-Si,Ge:H sample. In all the samples studied, two distinct bands of electron trapping states were observed: a shallow band lying between 0.65 and 0.7eV, and a deeper band lying between 0.75 and 0.8eV.

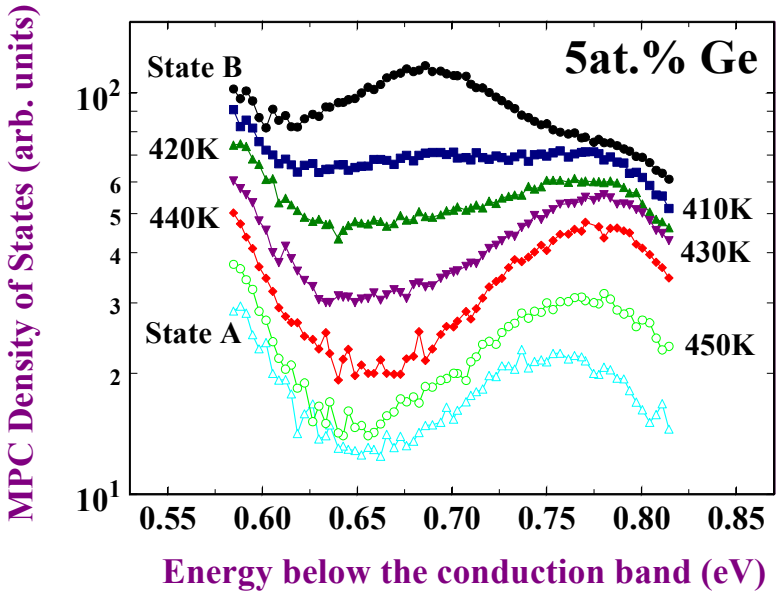

FIG. 36. Example of fits of MPC spectra to two Gaussian shaped defect bands. In the 2at.% Ge sample shown, and in all the other films as well, the deeper band is found to be dominant in state A, while the shallower band has a larger magnitude in state B.

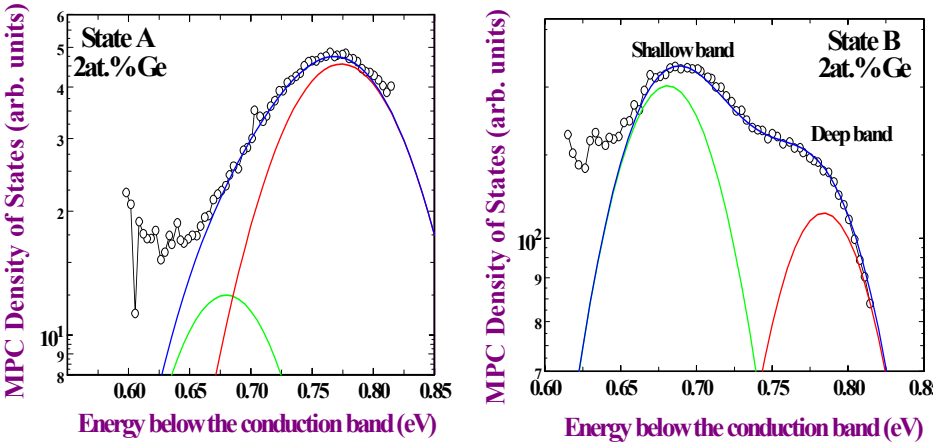

FIG. 37. Estimates of deep defect band densities (Ge) and shallow defect band densities (Si) for both state A (bottom half) and B (top half). The relative defect densities were obtained by fitting the MPC spectra and then their sum was compared to the DLCP values to estimate the actual densities. The identification of the deep and shallow defect bands as Ge and Si dangling bonds is made from ESR measurements as described below.

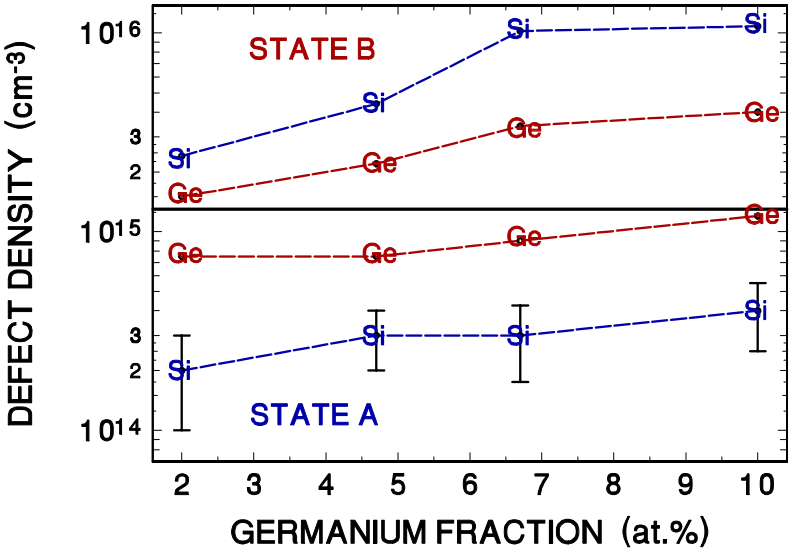

To determine the origin of the two defect bands seen in the MPC data we first note that this technique, as we have implemented it, monitors the re-emission of majority carriers out of deep states into which they get trapped. Therefore it could detect either the transitions from negatively charged to neutral dangling bonds (D^-/D^0 transitions) of the neutral defect states (D^0) or the transitions from the neutral to the positively charged dangling bonds (D^0/D^+ transitions) of the positively charged defect states (D^+). However, we now argue that both bands represent defects that are neutral in thermal equilibrium. First, previous MPC studies in pure a-Si:H have disclosed a defect band with the same prefactor and activation energy as our shallow band and which, through a comparison study with ESR in matched samples, was conclusively identified as originating from neutral Si dangling bond (D_{Si}^0) states [45]. Thus, it is reasonable that the corresponding MPC band in these a-Si,Ge:H alloys with low Ge fraction is again due to D_{Si}^0 states. The deeper MPC might then be associated with neutral Ge dangling bonds or positive Si or Ge dangling bonds. However, the deep band's nearly identical prefactor to the shallow band defect is consistent with a D_{Ge}^0 assignment. In addition, if there were a large number of charged defects we would expect a greater Fermi energy shift upon light soaking than we observe (Table VIII). Therefore we conclude that the MPC measurements are showing two distributions of different types of neutral dangling bonds.

To confirm this identification, we carried out ESR measurements on the a-Si,Ge:H alloy with fractions of 2 and 5 at.% Ge grown on quartz substrates. We observed that the number of D_{Ge}^0 dangling bonds was larger than the number of D_{Si}^0 states in both samples for state A, and that in state B the number of D_{Si}^0 were larger. Moreover, as can be seen in Table IX, the ratios of the magnitudes of these ESR signals agree with the corresponding MPC bands as identified above. Therefore, these facts provide independent evidence for the assignment of the shallow and deep bands to D_{Si}^0 and D_{Ge}^0 defect states, respectively.

We may also briefly discuss the changes in deep defect densities upon light soaking. Apparently, more of the Ge sites already contain unsatisfied bonds in state A due to the lower bond energies compared with Si. This leads to the dominance of the D_{Ge}^0 defects. Somewhat surprisingly, our results show a dominance of D_{Ge}^0 defects even for the samples with the smallest fraction of Ge. On the other hand, since there is an abundance of weak Si bonds, light-induced degradation causes more of these potential sites to become dangling bonds. This results in a higher density of neutral Si dangling bonds than Ge dangling bonds in State B. Not surprisingly,

TABLE IX. A comparison of MPC and ESR defect magnitude ratios for the 2at.% Ge film.

	MPC	ESR
State A	Shallow to deep band: 0.25 ± 0.04	D_{Si}^0/D_{Ge}^0: 0.19 ± 0.05
State B	Shallow to deep band: 1.4 ± 0.1	D_{Si}^0/D_{Ge}^0: 1.6 ± 0.4
State B/State A	Shallow band ratio: 12 ± 1	D_{Si}^0 ratio: ~10

however, once the Ge content exceeds 10%, more and more potential Ge defect sites exist and we observe that the trend begins to reverse.

Additional information can be obtained by comparing the photocapacitance and junction photocurrent spectra for these samples. While equally good photocapacitance spectra can be obtained using either a Schottky barrier or pn junction, reliable photocurrent spectra are only possible by using the buried p^+ substrate junctions. This is because the photocurrent spectra using the top metal junction also contain a component due to internal photoemission. Unfortunately, only 3 of the United Solar samples had sufficiently good blocking contacts at the substrate junctions to allow us to carry out the comparisons between photocapacitance and photocurrent spectra. These were the samples with 7, 13, and 20at.% Ge.

As an example, a photocapacitance/photocurrent spectral pair for the 20at.% Ge sample in state A is shown in Fig. 38. As has been discussed by us at length previously, when the two spectra are aligned at the lowest optical energies, the *ratio* of the photocurrent signal to the photocapacitance signal in the bandtail region allow us to estimate the $\mu\tau$ product for minority carriers (holes). This is because the photocurrent signal results from the *sum* of the minority and majority carrier transitions, while the photocapacitance signal results from the *difference*. In this manner we have estimated the $\mu\tau$ products for the 3 samples in state B, as well as 2 samples in state A. A summary of the results of this analysis is displayed in Fig. 39.

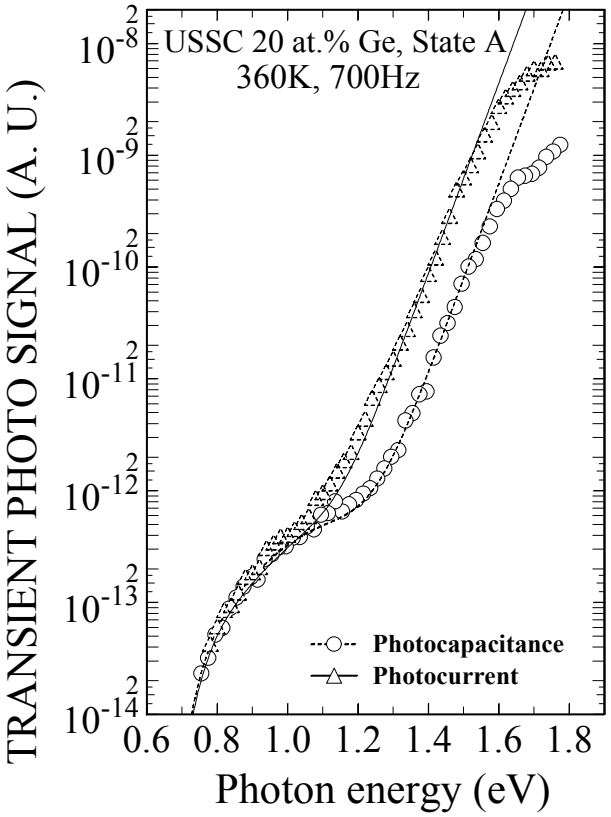

FIG. 38. Transient photocapacitance and transient photocurrent spectra obtained for the 20at.% Ge alloy United Solar sample. The substrate junction was held under 1.1V reverse bias and pulsed to 0.1V reverse bias during carrier filling. The two spectra have been aligned to overlap at the lowest photon energies. The thin solid lines drawn through the data are fits to a model incorporating deep defect transitions plus an exponential valence bandtail.

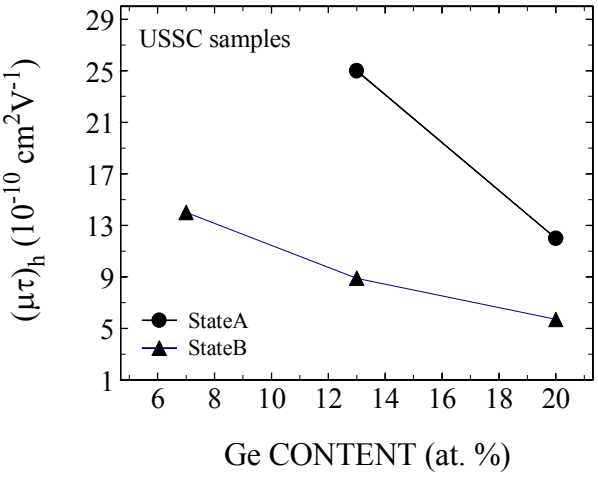

FIG. 39. Hole mobility-lifetime products as a function of Ge content for three a-Si,Ge:H alloys prepared at USSC. The μτ products were obtained by comparing photocapacitance and photocurrent spectra for each case, such as for the pair of spectra displayed in Fig. 37.

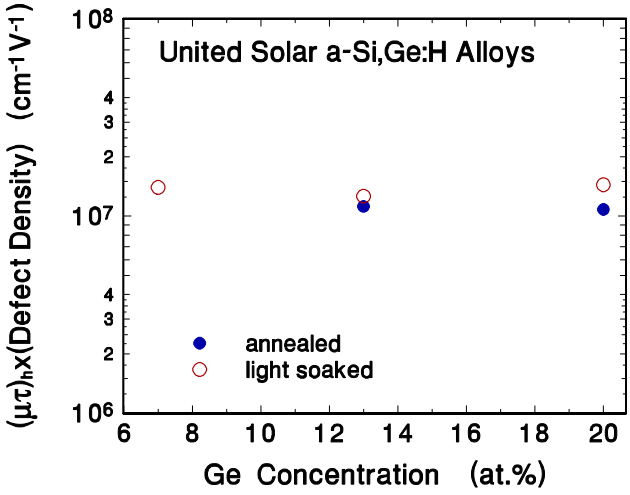

FIG. 40. Hole μτ product multiplied by the corresponding deep defect densities determined by the DLCP method. The nearly constant value near 10^7 cm^{-1} V^{-1} agrees with results for a-Si,Ge:H samples obtained previously with Ge fractions in the range 30 to 50at.%.

In our previous studies of a-Si,Ge:H alloys with Ge fractions in the range 30 to 50at.% we have found that these values of μτ are inversely correlated with the deep defect density. Thus, when we multiplied these μτ products by the corresponding deep defect density in each case as obtained using the drive-level capacitance profiling (DLCP) method, we obtained a nearly constant value independent of the Ge content or metastable state. Figure 40 indicates that this is again the case for these lower Ge fraction alloys. Moreover, the value of the resulting constant (near 10^7 cm^{-1} V^{-1}) agrees very well with the a-Si,Ge:H samples of higher Ge fraction that we have studied previously [46]. That is, the trends established for the higher Ge fraction a-Si,Ge:H alloys seem well preserved for the current series of United Solar low Ge fraction material as well.

The existence of both Si and Ge dangling bonds in these low Ge fraction samples, together with our ability to separately measure these using MPC spectroscopy, provides us with a unique opportunity to test the fundamental mechanisms of light induced degradation in amorphous silicon itself. The details of what we have learned from such studies will be reported in Section 8.

7.2 STRUCTURAL PROPERTIES OF UNITED SOLAR AMORPHOUS SILICON-GERMANIUM SAMPLES

One recurring theme in the subject of the a-Si,Ge:H alloys has been the relationship between preparation, microstructure, and physical properties. The electronic properties of these alloys have improved dramatically since the earliest comprehensive studies in the 1980's. [47,48,49] One of the issues raised in this regard has been that of compositional inhomogeneity, specifically in regard to non-uniform Ge incorporation in these alloys. This issue has considerable potential impact on the interpretation of the results of the previous Section which indicates the presence of two types of deep defects as revealed by our MPC measurements. One might wonder whether or not the stabilization of such defects could be related to the degree of Ge clustering in such alloys. Indeed, such preferential clustering has been predicted by theory [50], although the experimental evidence has been somewhat contradictory.

Given that most of the experimental studies using EXAFS were carried out before the electronic properties of the a-Si,Ge:H films had been optimized [51,52,53,54,55], we decided to examine the issue of Ge clustering again using the EXAFS technique on a set of state-of-the-art United Solar samples. The set of samples employed consisted of a superset of the low fraction Ge alloys described above. Specifically, the set of films studies included the 10at.%, 13at.%, and 20at.% films in the previous set, plus films with Ge fractions of 32.5at.% and 45.2at.%. In each case the Ge content was determined by energy dispersive spectroscopy (EDS) with an absolute accuracy of 0.2at.%. The lower Ge fraction samples (2, 5, and 7at.%) were not included because of the lower EXAFS signal levels involved.

The experimental technique consists of examining the x-ray absorption fine structure in the vicinity of the Ge K-edge. This absorption spectrum reveals a series of small wiggles in the absorption spectrum which result from coherent backscattering from the nearest atomic neighbors of the photo-excited electron from the Ge atom K-shell (see Fig. 41). The detailed structure of these wiggles depends on the types of near neighbors to that Ge atom (i.e., the

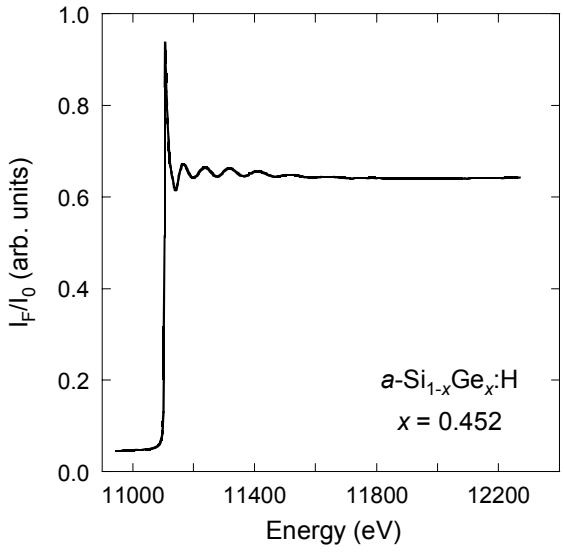

FIG. 41. Example of x-ray absorption fine structure near Ge K-edge in a-Si,Ge:H film with a Ge fraction of 45.2at.%

number of Ge *vs*. Si atoms) and the distances to these neighbors. Thus it is possible to deduce, for example, the number of Ge near neighbors to a given Ge atom in the a-Si,Ge:H network as a function of the Ge fraction in the film. The experimental result can thus be compared with the expected result assuming that the atoms are randomly distributed. If it exceeds this prediction, this would indicate Ge clustering. In addition, the Ge-Ge and Ge-Si bond lengths can be determined, again as a function of the Ge fraction.

These measurements were carried out by our collaborators at the University of Washington: B.D. Chapman, S.-W. Han, and G.T. Seidler using the Pacific Northwest Consortium Collaborative Access Team (PNC-CAT) bending magnet beamline at the advanced photon source x-ray synchrotron located at Argonne National Laboratory. The small sample thickness compared to the x-ray absorption length together with the strong elastic cross-section from the single crystal Si substrates required used of several methods to minimize contamination of the EXAFS signal. These included sample spinning at 500rpm to average out the diffraction background, various types of advanced x-ray filtering, keeping the scattering angle near 90^{o} to decrease dipole scattering, and masking the Bragg peaks from the Si substrate at the detector face with 1mm thick Pb tape.

The results showing the average Ge atom coordination as a function of Ge fraction are displayed in Fig. 42, and the average Ge-Si and Ge-Ge bond lengths are shown in Fig. 43. Two assumptions were made in the fits that were used to obtain these results. First, the total coordination was fixed at four and, second, the two Debye-Waller factors ($\sigma^2_{\text{Ge-Ge}}$ and $\sigma^2_{\text{Ge-Si}}$)

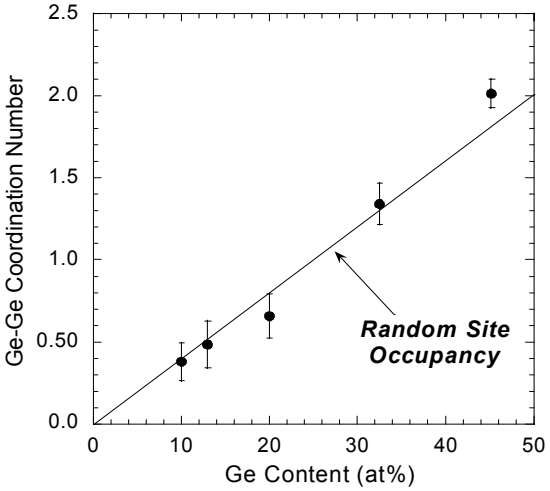

FIG. 42. Plot of Ge-Ge coordination number as a function of Ge content. The solid line is expected for a completely random Ge-Ge distribution (no Ge clustering)

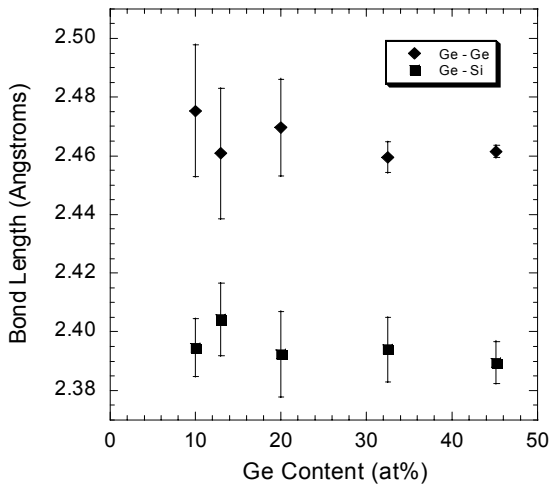

FIG. 43. Plot of near-neighbor bond lengths as a function of Ge content. Note that these bond lengths are essentially independent of the Ge fraction.

were set equal to each other for each data set. This latter assumption has been found to be the case in many previous EXAFS investigations. Relaxing this constraint did not affect any of the conclusions within the experimental uncertainties.

The results displayed in Fig. 42 for the Ge-Ge coordination number are consistent with a random local distribution of the Ge atoms as indicated by the straight line in the figure except for the 45.2at.% film which does show some degree of short range Ge-Ge clustering. The bond lengths displayed in Fig. 43 are found to be effectively independent of the alloy composition with weighted means of 2.461±0.004Å for the Ge-Ge bond length and 2.393±0.009Å for the Ge-Si bond length.

To summarize, then, this structural analysis of the EXAFS data reveals no evidence for Ge-Ge clustering, indicating complete miscibility of Ge and Si in the alloying process as well as little hydrogen incorporation into the local Ge environment. We also find no compositional dependence in the Ge environment near-neighbor bond lengths (Ge-Ge and Ge-Si), suggesting that there is little topological rigidity in the amorphous phase. This latter result appears inconsistent with a recent EXAFS study of MBE grown, Si ion amorphized samples.[56]

We conclude this discussion by noting that there are many types of inhomogeneity which may influence device performance that would not be detected by EXAFS. For example, in the recent careful study by Goerigk and Williamson [57], a degree of anomalous small x-ray scattering was found for a-Si,Ge:H films of high electronic quality similar to those employed in our own study. Their results were interpreted as evidence for two-phase segregation, with a small increase in Ge content in the dominant phase. They inferred a columnar microstructure in the growth direction, and a considerable decrease in local Ge content in the remaining 5 to 10at.% of the sample between the columns. The EXAFS results reported here would probably not be able to discriminate against such a proposed morphology given the experimental errors and the fact that the low-volume phase, with its greatly decreased Ge content, would have little weight the fluorescence signal.

7.3 UNITED SOLAR a-Si,Ge:H FILM PROPERTIES VERSUS CELL PERFORMANCE

We also made a serious attempt to correlate cell performance with defect densities by employing this particular series of low Ge fraction a-Si,Ge:H material produced by United Solar. In this series of depositions they had provided us with a series of six 0.9μm to 1.2μm thick films, with Ge fractions near 2, 5, 6.5, 10, 13, and 20at.% . In addition, they also fabricated a p-i-n device (SS/n-i-p/TCO) using each of these alloy fractions as the i-layer. Unfortunately, many of these devices utilized i-layers of varying thickness. However, three of the matched devices incorporated i-layers of 1600Å thickness, which were the samples with Ge fractions of 5at.%, 13at.%, and 20at.%. We thus decided to examine the film and device properties for these three alloy materials and look for possible correlations.

TABLE X. Comparison of United Solar a-Si,Ge:H films and devices. The cell parameters before and after degradation were measured at USSC; the deep defect densities in the films were measured at Oregon. The light soaking of each film and matched device pair used a 610nm filtered ELH source at the light intensity indicated for 192 hours at the University of Oregon.

Ge (at.%)	State (Intensity)	J_{SC} (mW/cm^2)	V_{OC} (volts)	Fill Factor	Efficiency (%)	Defect Density (cm^{-3})
5	A	11.6	0.917	0.661	7.03	2×10^{15}
5	B ($40mW/cm^2$)	11.3	0.898	0.632	6.41	7.2×10^{15}
13.5	A	12.9	0.852	0.632	6.95	4.5×10^{15}
13.5	B ($39mW/cm^2$)	12.4	0.824	0.590	6.03	9.8×10^{15}
20	A	14.4	0.800	0.602	6.94	9.0×10^{15}
20	B ($26mW/cm^2$)	13.7	0.775	0.560	5.95	1.34×10^{16}

To carry out this study, we first measured the defect densities and device parameters for the 3 pairs of matched films and devices in the annealed state. We then borrowed the 3 devices from United Solar and degraded each film and corresponding device under nearly identical conditions. This involved correcting for the metal contact thickness on each film in the light exposure of each device. We used the same filtered ELH light, consisting of a 610nm long pass, to achieve more spatially uniform degradation. The intensity varied between $26mW/cm^2$ and $40mW/cm^2$ (see Table X) depending upon the attenuation of the metal contact layer used for the film measurements in each case. Exposure time was 192 hours. We verified that this was of sufficient duration to produce saturation in one a-Si,Ge:H film (the 10at.% Ge alloy). After exposure we again measured the defect densities in our films and mailed the devices back to Jeff Yang at United Solar where the device parameters were determined. The results of these matched film and device measurements are given in Table X.

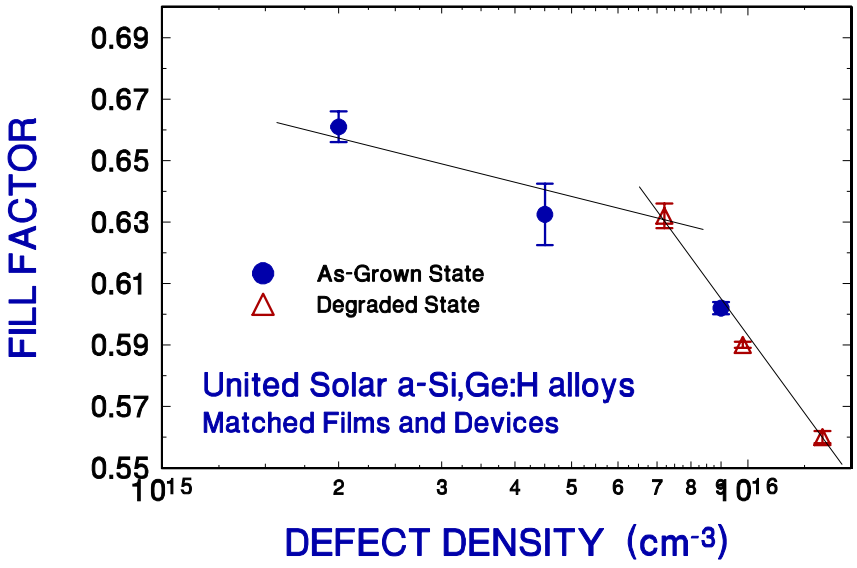

FIG. 44. Fill Factor vs. Deep Defect Density for three matched a-Si,Ge:H films and devices produced at United Solar. The light exposure to produce the degraded state was identical for each film/device pair. The lines drawn are guides to the eye.

Examining the results in this Table allows us to make a few obvious conclusions. First, all of the devices show degradation in all of their device parameters, and a significant increase in the deep defect density. As expected, increasing Ge content increases J_{SC} and decreases V_{OC}. Quantitative correlations between defect density and device parameters are more difficult to formulate; however, a plot of the fill factors vs. defect density displayed in Fig. 44 does seem to indicate a marked effect once the deep defect density exceeds about 7×10^{15} cm^{-3}. Below this value, the fill factor is nearly independent of the defect density, indicating that other device properties are probably limiting the overall cell performance.

7.4 EVALUATION OF a-Si,Ge:H ALLOY MATERIAL FROM OTHER SOURCES

7.4.1. BP Solar a-Si,Ge:H Alloys

This past year we began an evaluation of BP Solar a-Si,Ge:H alloy material. We obtained a preliminary series of a-Si,Ge:H alloy samples deposited with Ge fractions of 5, 10, and 40at.%. These were characterized in a light degraded produced by a 100 hour exposure to a red (610nm) filtered tungsten halogen light source at an intensity 1.1W/cm^2 (corrected for the semi-transparent contact on each film). The electronic properties of each film were measured using drive-level capacitance profiling and transient photocapacitance spectroscopy. The experimental results obtained on the three alloys using these methods are displayed in Figures 45 and 46, respectively.

The deep defect densities (shown in Fig. 45) were estimated by doubling the spatially average capacitance profile for each film. These results are listed in Table XI. We also obtained defect density estimates, as well as Urbach energies, by fitting the photocapacitance spectra shown in Fig. 46. To obtain good fits for the deep defect bands to the 5 and 10at.% sample spectra we found it was necessary to assume *two* Gaussian shaped defect bands in each case. This is consistent with our studies of a-Si,Ge:H alloys in the low Ge fraction regime obtained from United Solar Systems which exhibited two types of defect bands of similar magnitude in the light degraded state (see the previous Section). The values obtained from the fits of the photocapacitance spectra are also listed in Table XI. We observe that the relative magnitudes of the shallower deep defect band agrees most closely with the values determined by the drive-level capacitance profiling. Note that, in general, the defect densities obtained are very low and the value of the Urbach energy is also quite small and essentially independent of the Ge concentrations. This indicates that these BP Solar alloy films are of extremely high quality.

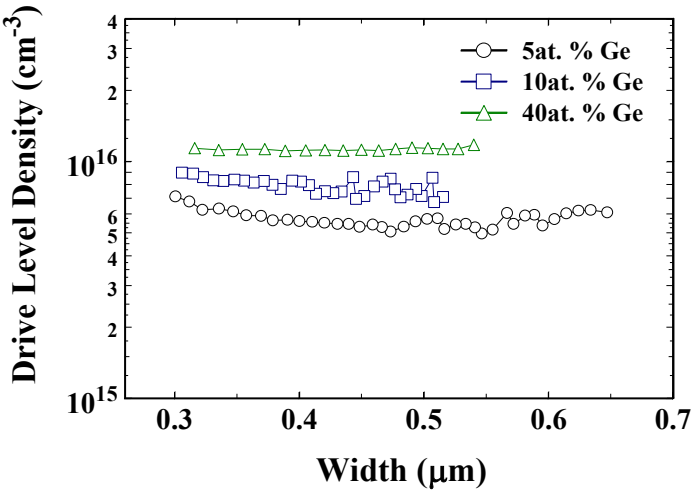

FIG. 45. Drive-level profiles for three BP Solar a-Si,Ge:H alloy films in a light degraded state. The measurement conditions were: 10Hz and 360K for the 5at.% and 10at.% Ge films; 100Hz and 350K for the 40at.% film. Estimated total deep defect densities are obtained by doubling the spatial average of these profile values.

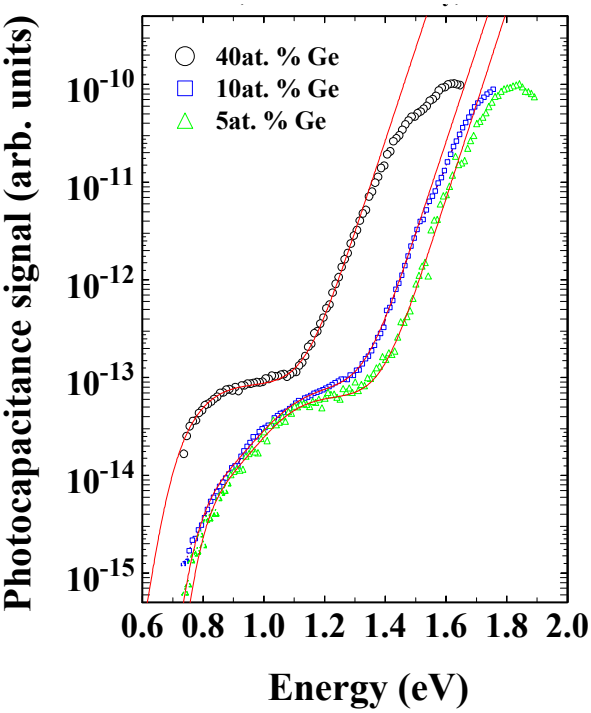

FIG. 46. Transient photocapacitance spectra for the three BP Solar a-Si,Ge:H films in a *light degraded state*. The thin lines drawn through the data points are fits from an assumed density of states consisting of *two* Gaussian shaped deep defect bands plus an exponential band tail. For the 40at.% fits, only a single Gaussian deep defect band was used.

TABLE XI. Defect densities for the three BP Solar a-Si,Ge:H films in their light-degraded states obtained from drive-level capacitance profiling (N_{DL}) and transient photocapacitance spectroscopy. In the latter case, the spectra indicated the presence of two defect bands, a "shallow" and a "deep" band, and the magnitudes obtained from these fits are given below. Urbach energy values obtained from the photocapacitance spectra are also given.

Ge content (at.%)	N_{DL} (cm^{-3})	E_U (meV)	Shallow Band (cm^{-3})	Deep Band (cm^{-3})	Shallow+Deep (cm^{-3})
5	1.1×10^{16}	45	1.1×10^{16}	1.7×10^{16}	2.8×10^{16}
10	1.6×10^{16}	45	1.2×10^{16}	1.6×10^{16}	2.8×10^{16}
40	2.1×10^{16}	46	2.3×10^{16}	---	2.3×10^{16}

7.3.2. NREL Hot-Wire CVD a-Si,Ge:H Alloys

Brent Nelson sent us an extensive series of a-Si,Ge:H films grown by the hot-wire CVD method in the latter part of 1999. These are listed in Section 2.4.2 and contained Ge fractions of roughly 0, 2, 5, 20, 35, and 50at.%. Unfortunately, the higher Ge fraction films (35 and 50at.%) did not allow Schottky barrier contacts with sufficient quality to allow us to characterize their electronic properties by our techniques. Nonetheless, we are able to report on the properties of several of the films deposited on stainless steel substrates in both the annealed and light degraded state. The light soaking conditions are essentially identical to those described above for the BP Solar a-Si,Ge:H films.

It is first of all interesting to compare the relationship between optical gaps and Ge content between the HWCVD films and the a-Si,Ge:H material from the different sources described above. In Fig. 47 we display this relationship for the alloys with Ge fractions of 20at.% or below. Note that for a given Ge content the HWCVD a-Si,Ge:H material exhibits significantly lower optical gaps, although the dependence of E_{04} on Ge fraction is similar to the United Solar material. The two BP Solar DC glow discharge films in this range lie between the United Solar rf glow discharge material and the HWCVD material; however, the dependence of E_{04} on Ge content appears to be considerably stronger.

The defect densities for the HWCVD films were again determined using the DLCP method. In addition, ac admittance measurements were used to determine the Fermi-level positions in both metastable states. Examples of DLCP profiles are displayed in Fig. 48 and indicate good uniformity of materials properties. The defect densities derived from these DLCP profiles for all the samples measured for both states A and B are displayed in Fig. 49.

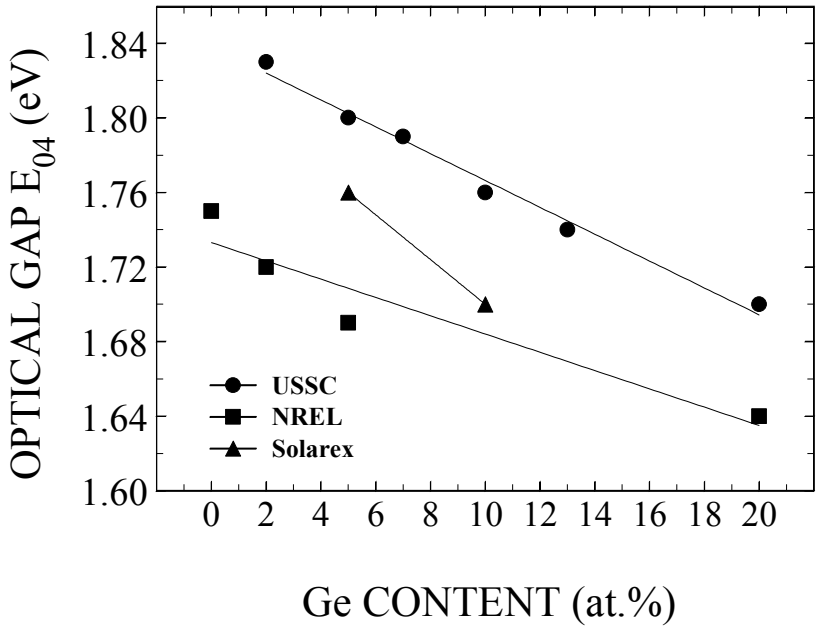

FIG. 47. Optical gap versus Ge content for a-Si,Ge:H alloys from three sources.

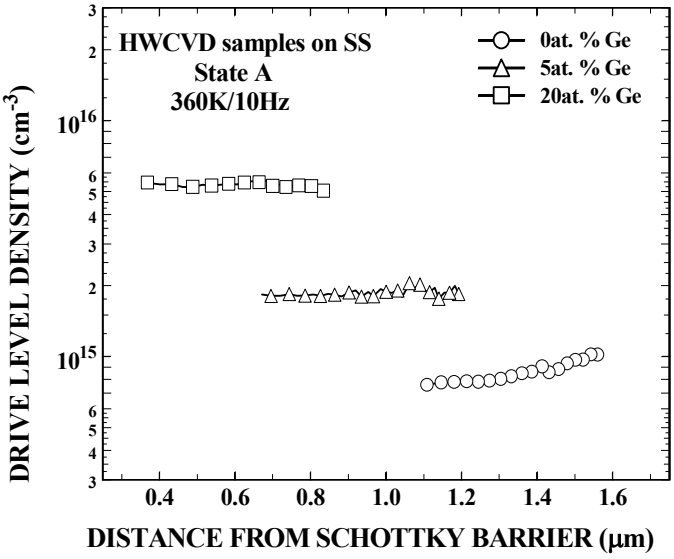

FIG. 48. Examples of drive-level capacitance profiles for 3 NREL HWCVD samples with different Ge fractions. These data were obtained in the dark annealed state for films deposited onto stainless steel substrates.

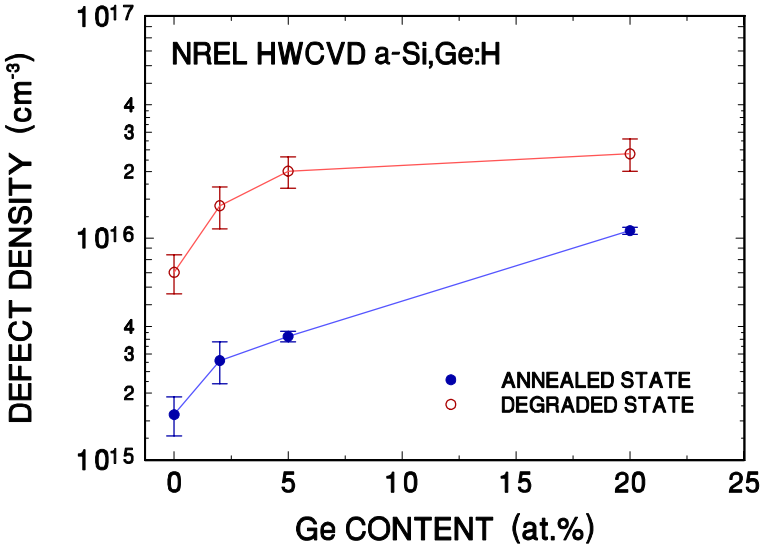

FIG. 49. Defect densities estimated from the drive-level profiling measurements for four NREL HWCVD a-Si,Ge:H films with varying Ge content. The defect density displayed is obtained by doubling the spatially averaged values obtained using a measurement temperature of 360K and a frequency of 10Hz. The error bars reflect the degree of spatial variation in the profiles themselves. Several examples of actual profiles are displayed in Fig. 48.

In Fig. 50 we display the transient photocapacitance spectra for three of these samples in State A. It is quite interesting to compare these spectra with those of the BP Solar a-Si,Ge:H shown in Fig. 46. Although it appears one has similarly good properties for the 5at.% Ge sample, the 20at.% sample definitely appears inferior to the higher Ge BP Solar films in that it exhibits both a much broader Urbach tail and more significant "shoulder" of deep defects. We tentatively conclude that further optimization of these HWCVD samples will be required before they are able to perform well in solar cell devices.

In Table XII we summarize the electronic properties derived for the four HWCVD a-Si,Ge:H alloy samples determined to date.

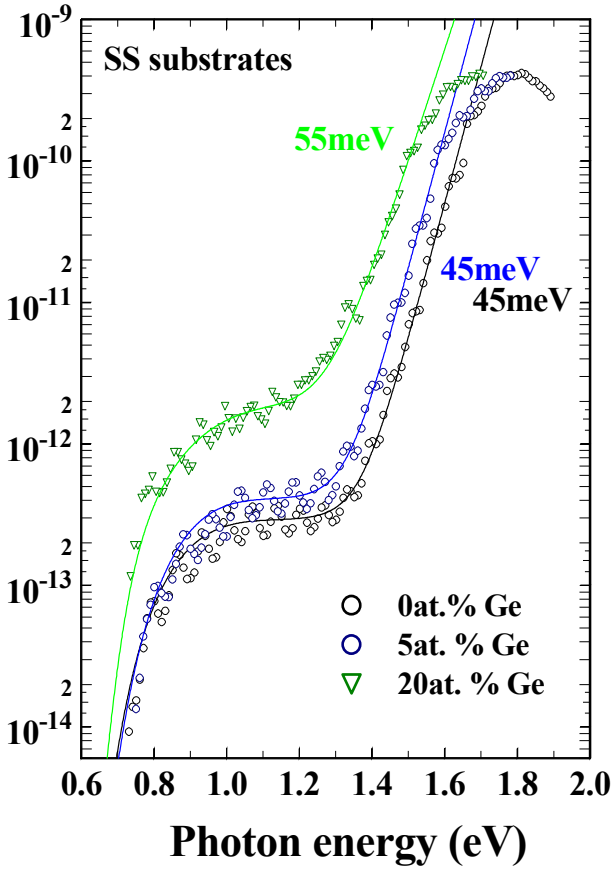

FIG. 50. Transient photocapacitance spectra for three NREL HWCVD a-Si,Ge:H films in their annealed state. The 2at.% sample spectrum lay in between the 0% and 5at.% spectra and is therefore omitted for clarity. Note the much more significant interference fringes in these spectra compared to the spectra of the BP Solar a-Si,Ge:H samples displayed in Fig. 46. This is due to the stainless steel substrates employed for these films instead of the c-Si substrates for the BP Solar samples. Also note the very broad bandtail for the 20at.% Ge sample.

TABLE XII. Summary of electronic properties of NREL HWCVD a-Si,Ge:H alloys. Properties are listed for both the annealed (state A) and light-degraded states (state B). The Fermi-level position, $E_C - E_F$, reflects the activation energy of conductivity determined from ac admittance measurements. The defect densities were determined from the DLCP profiles as described above, and the Urbach energies were obtained from the transient photocapacitance spectra.

Sample	Ge content (at.%)	State	$E_C - E_F$ (eV)	Defect Density (cm^{-3})	Urbach Energy (meV)
H684	0	A	0.69	1.6×10^{15}	45
H684	0	B	0.74	7.0×10^{15}	
H688	2	A	0.72	2.8×10^{15}	45
H688	2	B	0.78	1.4×10^{16}	
H685	5	A	0.69	3.6×10^{15}	45
H685	5	B	0.77	2.0×10^{16}	
H687	20	A	0.67	1.1×10^{16}	55
H687	20	B	0.72	2.4×10^{16}	

8.0 INSIGHTS INTO DEGRADATION FROM STUDIES OF LOW Ge ALLOYS

8.1 METASTABLE DEEF DEFECT CREATION AND ANNEALING FUNDAMENTALS

As discussed in Section 7.1 above, the a-Si,Ge:H films with low Ge fractions were found to exhibit two distinct bands of deep defects as revealed by modulated photocurrent (MPC) measurements. Moreover, using auxiliary ESR measurements on a couple of matched films deposited onto quartz substrates, we were able to identify the two bands as originating from neutral Si dangling bonds (D^0_{Si}) and neutral Ge dangling bonds (D^0_{Ge}). In Section 7.2 we examined the results of EXAFS studies on the United Solar a-Si,Ge:H films which indicated no evidence of Ge atom clustering in these alloys. Thus, with a fair degree of confidence, we may assume, for the samples with Ge fractions below 10at.%, that the Ge atoms and, in particular, the Ge dangling bonds, are effectively isolated within these films possessing only Si atomic near neighbors.

Both bands of dangling bond defects were found to increase significantly under light exposure. Somewhat surprisingly the deeper band (D^0_{Ge}) was larger in the light annealed state (state A) for all the alloys while the shallower band (D^0_{Si}) was always larger in the degraded state (state B) (see Fig.37). The two bands thus were found to be created and to anneal at different rates. Examples of series of such MPC spectra during defect creation and annealing are shown for the 7at.% Ge film in Figs. 51 and 52, respectively.

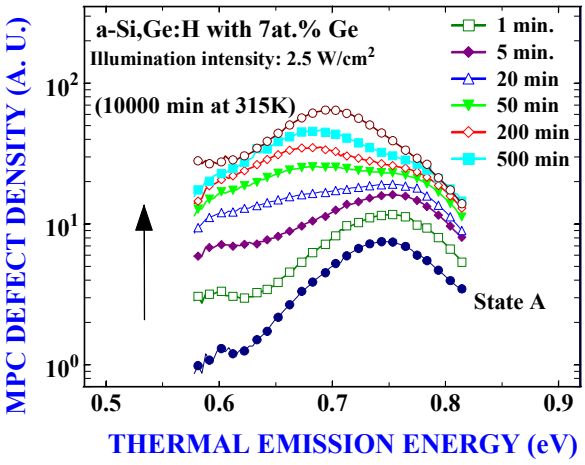

FIG. 51. MPC derived defect distributions at different states of light-induced degradation for the a-Si,Ge:H with 7 at.% Ge content. The temperature during degradation was 315K. The MPC measurement temperature was 340K, and we used the usual thermal emission prefactor ($\nu = 2 \times 10^8 \times T_m^2$) to transform the modulation frequencies into an energy scale.

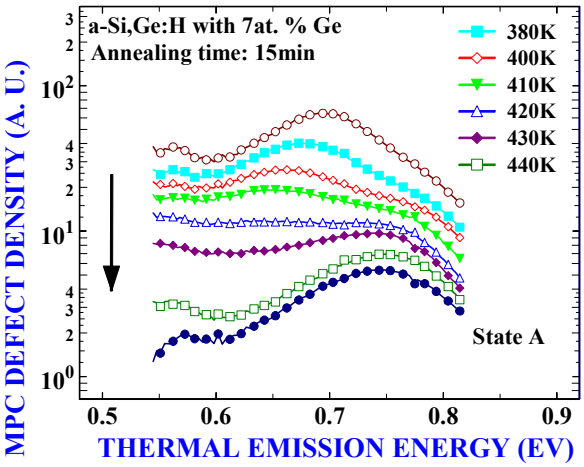

FIG. 52. MPC spectra for a sequence of anneal states for the 7at.% Ge sample. The MPC measurement temperature was again 340K. Note that the deeper band, associated with Ge dangling bonds, is dominant in State A, while the shallower band, associated with Si dangling bonds, is larger in State B.

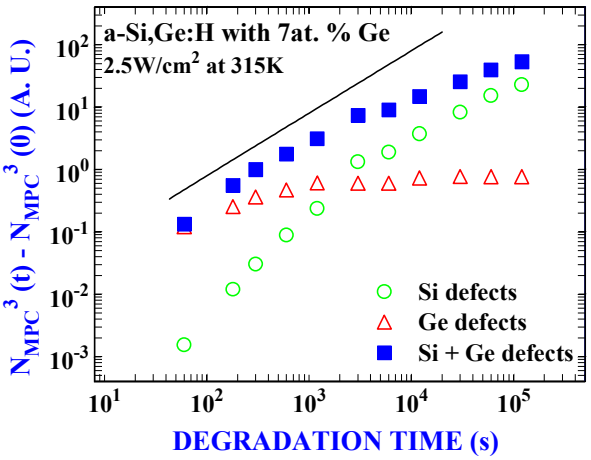

FIG. 53. The cubes of the light-induced Si, Ge, and *total* defect densities of the a-Si,Ge:H sample with 7 at.% Ge are plotted as a function of exposure time. The line in the diagram has unit slope and is shown to help clarify the different time dependencies of the two types of defects.

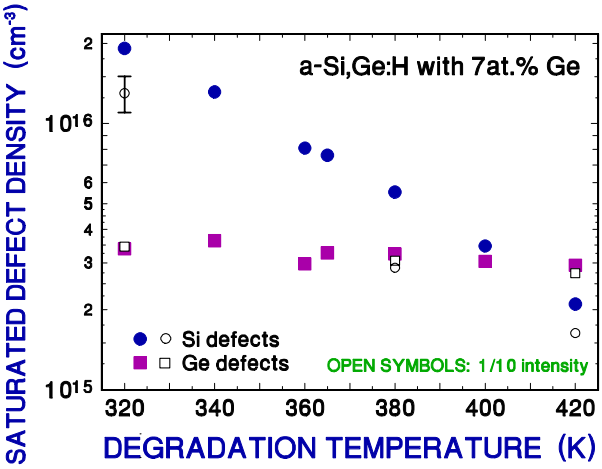

FIG. 54. The densities of Si and Ge dangling bonds for long exposure times for the 7 at.% Ge sample as a function of the degradation temperature at two light intensities. The light intensity was 2.5 W/cm^2 for the solid symbols, and 250 mW/cm^2 for the open symbols

As described in Section 7.1, we fit the two bands with Gaussians to determine their relative magnitudes. In Fig. 53 we display the degradation behavior of the individual densities for D^0_{Si} and D^0_{Ge} for the 7 at.% Ge sample. Two characteristic time regimes seem to appear: (1) For t < 30min, the D^0_{Si} density increases much faster than the usual $t^{1/3}$ time dependence, while the D^0_{Ge} density increases much more slowly. Nevertheless, the overall defect density follows the $t^{1/3}$ time dependence. (2) For t > 30 min, no more metastable D^0_{Ge} are created, while there is still significant creation of D^0_{Si} with the usual $t^{1/3}$ kinetics.

We also studied the defect creation kinetics at different temperatures and light intensities. In Fig. 54 we display the saturated defect densities of D^0_{Si} and D^0_{Ge} as a function of temperature. One can see that the observed maximum value for Ge dangling bonds is almost independent of temperature between 320K and 420K at both light intensities . On the other hand, the saturated density of Si dangling bonds decreases significantly with increasing temperature and decreasing light intensity. This suggests that there is an actual upper limit to the density of Ge dangling bond precursor sites. On the other hand, as is now widely accepted, the saturation behavior of the Si dangling in these samples appears to be determined by a dynamical balance between degradation, thermal annealing, and light-induced annealing. [58,59]

We next address the annealing kinetics of the D^0_{Si} and D^0_{Ge} for these alloys. The defect densities were determined in the same manner as for the degradation studies. We plot in Fig. 55 the individual defect densities as a function of the total integrated MPC density of an annealing series for *two different samples*. In this figure the defect magnitudes for the two samples have been normalized to be the same at the crossing point. One can see that the D^0_{Ge} density remains fairly constant in the initial stages of the annealing (annealing proceeds from right to left), while

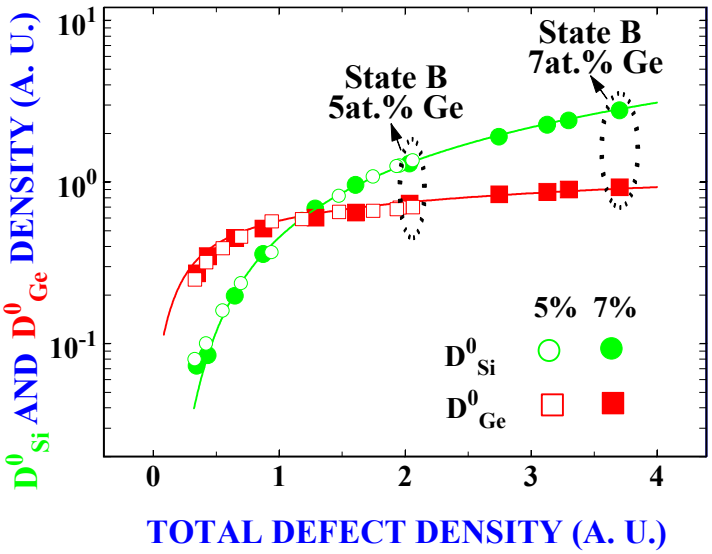

FIG. 55. Estimated MPC densities of Si and Ge deep defects as a function of the total defect density during isochronal anneal sequences of 15 min duration for the 5 at.% (open symbols) and the 7 at.% Ge (solid symbols) samples. To fit the data we used the solution to Eq. (1) with $\eta \approx 0.25$.

the D^0_{Si} drops significantly. However, once the D^0_{Si} becomes appreciably smaller than the D^0_{Ge} density, the latter starts to decrease as well. We have found similar results for all of our samples, independent of the times used for the isochronal anneals (ranging between 15 minutes and 450 minutes). Hence, our data indicate a *direct correlation* between the annealing processes of the two defects rather than different activation energies for the annealing of D^0_{Ge} and D^0_{Si}.

The annealing behavior can be described quantitatively and leads to the fits shown in Fig. 54. Let's suppose that every partial anneal reduces the total deep defect density by some ΔN_{tot}. If there is a global reconfiguration process, then the Si and Ge defects will compete for their share of the total defect density. Independent of possible underlying mechanisms there will be a probability $k_{Si}N_{Si}$ that the D^0_{Si} defects will be reduced and a probability $k_{Ge}N_{Ge}$ that the D^0_{Ge} defects will be reduced. Therefore, we have

$$\frac{dN_i}{dN_{tot}} = \frac{k_i N_i}{k_{Si}N_{Si} + k_{Ge}N_{Ge}} \tag{9}$$

where i denotes Si or Ge, and k_{Si} and k_{Ge} are the corresponding effective "capture coefficients" for the global entity responsible for the annealing process. The integration of Eq. (9) leads to the fits shown in Fig. 55. One should notice that there is basically only one fitting parameter, namely $\eta = k_{Ge}/k_{Si} \approx 0.2$.

One possible microscopic scenario of the annealing behavior might be long-range hydrogen diffusion. H gets released from some kind of reservoir, diffuses through the material and then gets trapped by a dangling bond. This interpretation would be consistent with the recently proposed "hydrogen collision" model by H. Branz [60]. Another viable explanation could involve the release of network strain upon annealing.

FIG. 56. MPC determined Ge defect density plotted *vs*. the MPC determined Si defect density for an annealing sequence (450 min isochronal steps) and a degradation sequences (light exposure at 315 K). The fitted (solid) line for degradation was obtained using the solution to Eq. (13) with $\xi(315K) \approx 4$, and $N_{Ge}^{P} \approx 3.3 \times 10^{15}$ cm^{-3}, while the annealing data were fitted via Eq. (9) with $\eta \approx 0.2$.

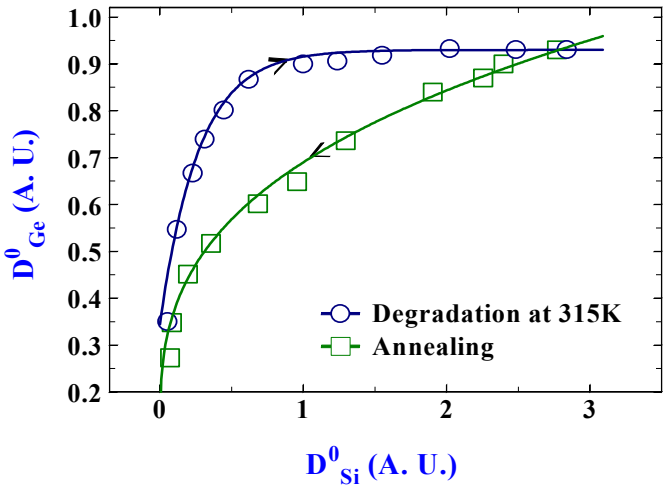

More insight was obtained by studying the degradation kinetics of Si and Ge defects. In Fig. 56 we plot the degradation (at 315K) and annealing MPC densities of D^0_{Ge} *vs* D^0_{Si}. We can see that the degradation and annealing follow different paths. The annealing trajectory is correctly predicted from Eq. (1) to be $N_{Ge} \propto N_{Si}^{\eta}$. The degradation behavior on this plot is found follow a simple exponential behavior which is correctly predicted using fairly general equations. We describe the analysis used to deduce the exponential dependence of N_{Ge} *vs*. N_{Si} briefly as follows:

Defect creation in pure a-Si:H is usually described by the equation:

$$\frac{dN_{Si}}{dt} = c_{SW}^{Si} N_{Si}^{P} - f(G,T) \tag{10}$$

where N_{Si}^{P} denotes the potential deep defect precursor sites and f(G,T) is a function describing the annealing terms which will depend on the generation rate G and degradation temperature T. The annealing terms are usually negligible prior to the onset of saturation after long exposure times. In 1985 Stutzmann, Jackson, and Tsai proposed a bi-molecular carrier recombination (bcr) mechanism to account for the observed $t^{1/3}$ time dependence.[61] Hence, the creation coefficient c^{Si}_{SW} becomes proportional to G^2/N_{Si}^2, where G is the optical carrier generation rate. In the H-collison model [60] Branz suggests one should replace Eq. (10) by:

$$\frac{dN_{Si}}{dt} = \alpha_{Si} N_{Si}^{P} G - \beta_{Si} N_m N_{Si} \tag{11}$$

In this model the precursor sites N^{P}_{Si} are specified as Si-H sites and N_m, whose time evolution is described by another, coupled rate equation, is the concentration of mobile hydrogen atoms in the amorphous network. Also, α_{Si} is considered to be only weakly dependent on G or N_{Si}. In this description, N_m is expected to reach quasi-equilibrium rapidly with N_{Si} through H-emission from Si-H sites and mobile H retrapping to dangling bonds. That is, the second term on the right-hand side of Eq. (11) tracks the first term very closely. Ultimately, N_{Si} will slowly increase through H

collisions that form metastable pairs. Branz showed that the $t^{1/3}$ time dependence could then arise from this occasional pairing of H.

To apply these models to our a-Si,Ge:H alloys we had to extend the rate equations by incorporating a second type of dangling bond. Equation (11) can be used as a general equation to describe the creation of D^0_{Si} with the understanding that the second term on the right side is absent for the bcr mechanism and that α_{Si} is proportional to G/N_{tot}^2. However, for the Ge defects we need to take the apparent upper limit into account in the creation kinetics:

$$\frac{dN_{Ge}}{dt} = \alpha_{Ge}\left(N_{Ge}^{P} - N_{Ge}\right)G - \beta_{Ge}N_{m}N_{Ge} \tag{12}$$

For the bcr mechanism the second term would be again absent and α_{Ge} would be proportional to G/N_{tot}^2. If we ignore in each Eq. (11) and Eq. (12) the H-recapture term (second term) and divide Eq. (12) by Eq. (11), we obtain

$$\frac{dN_{Ge}}{dN_{Si}} = \xi\left(1 - \frac{N_{Ge}}{N_{Ge}^{P}}\right), \quad with\ \xi = \frac{\alpha_{Ge}N_{Ge}^{P}}{\alpha_{Si}N_{Si}^{P}} \tag{13}$$

The solution of this rate equation yields a simple exponential, which gives the excellent fit to the N_{Ge} *vs* N_{Si} data shown in Fig. 56. The inclusion of the second term in Eqs. (11) and (12) would spoil the simple exponential form and this argues, to some degree, against the H-collision model.

To further test the H-collision model we then studied an additional aspect of the defect creation kinetics. Annealing the sample, initially in State B, at 420 K for 15 min creates equal densities of D^0_{Si} and D^0_{Ge} for a very different total defect density than is obtained when we have equal densities during the initial degradation sequence. We can then compare two different degradation cases which are displayed in Fig. 57. One can see that after 20s of light-exposure following an anneal at 420 K for 15 min (Case II), the D^0_{Ge} density becomes the same as for Case I (degraded from the fully annealed State A), while the D^0_{Si} is almost 10 times higher. From here, both defect densities increase at a *slower* rate for Case II than for Case I. Hence, the total defect density increases also at a slower rate, implying that N_m must be smaller in the H-collision model. As N_{Ge} is not much changed, one would expect from Eq. (12) that dN_{Ge}/dt should be larger in Case II than in Case I, contradicting the observed data. On the other hand, the bcr mechanism would predict that dN_{Ge}/dt should be smaller in Case II because the total defect density is larger in Case II at this point. That is, both dN_{Ge}/dt and dN_{Si}/dt should be smaller, agreeing with our observation.

We note that our experimental results do not prove the bcr mechanism, nor do they refute the metastable pairing mechanism proposed in the hydrogen-collision model. However, they seem to be at odds with one aspect of this model; namely, of having a significant population of mobile hydrogen that recaptures frequently onto dangling bonds during the degradation process.

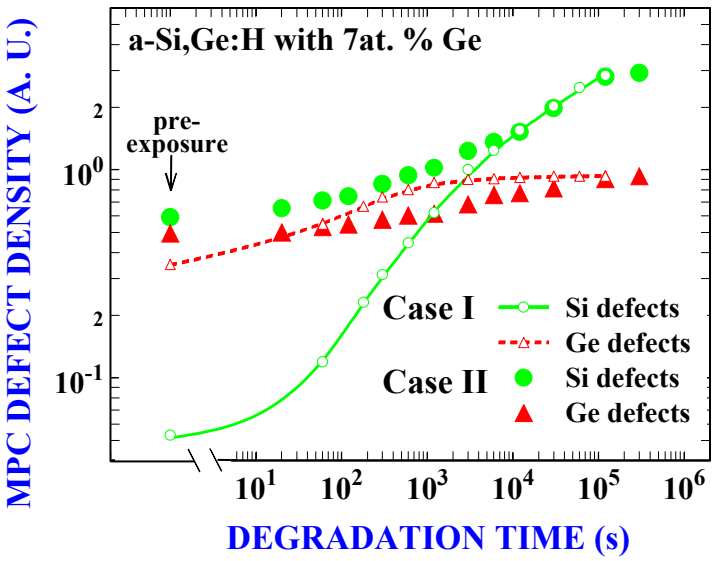

FIG. 57. Comparison of creation kinetics of Si and Ge dangling bond defects for two different initial conditions. The open symbols with the solid lines represent the degradation beginning at state A (Case I), while the solid symbols display the creation of defects vs. light exposure time beginning at a 420K/15min intermediate anneal state (Case II). Note that Ge defects are nearly equal after 20s of light exposure for the 2 Cases, while the Si defects are nearly 10 times higher for Case II compared to Case I.

8.2 LIGHT INDUCED ANNEALING AND SATURATION BEHAVIOR

To try to understand more about saturation (Fig. 54) as well as more of the details of the annealing mechanism, we carried out experiments to specifically examine light induced annealing. These experiments followed procedures paralleling previous studies in pure a-Si:H.[62] We first degraded under high light intensity, 2.5W/cm^2, red filtered light at 365K for 20 hours. In Fig. 58(a) we display the results of annealing in the dark on the magnitudes of both types of defects as a function of the anneal time. In Fig. 58(b) the annealing was also carried out at 365K, but in the presence of the red filtered light at 25mW/cm^2 intensity. Here one can clearly see the effect of the weak light on the annealing process: for example, the rate of annealing of the Si defects has increased by more than an order of magnitude. There is a similar

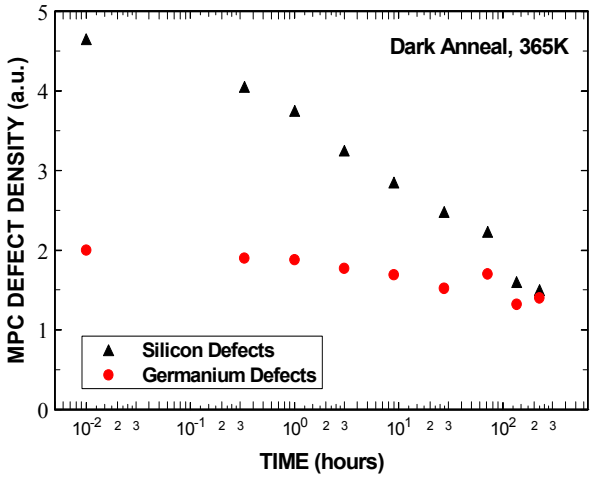

FIG. 58(a). Isothermal anneal of defects in the 7at.% Ge sample in the dark following degradation with high intensity light (2.5W/cm^2) at 365K.

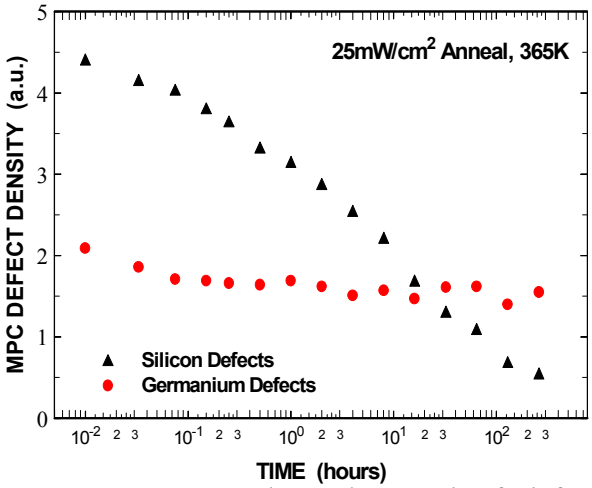

FIG. 58(b). Isothermal anneal of defects from same degraded state as in Fig. 57(a), except in presence of light at 25mW/cm^2 intensity.

increase of annealing rate for the Ge defects except that saturation is apparently reached in a fairly short time – a few hours – even though the Si defect density appears to continue to be reduced even after a couple hundred hours of annealing.

In Fig. 59 we replot the isochronal annealing data of Fig. 55, that is, the individual defect densities vs. the total defect density, except that now the vertical scale is linear instead of logarithmic. Next, we replot the data shown in Figs. 58(a) and 58(b) in the same manner: The defect densities of each type plotted against the total. These are displayed in Fig. 60(a) and 60(b) with the approximate annealing times now indicated on the scale at the top of each graph. There appear to be several noteworthy observations. First of all, the functional form of the dark isothermal anneal data in Fig. 59(a) agrees extremely well with the isochronal anneal data in Fig. 58 except that the state B silicon dangling bond density is lower in Fig. 59 due to the higher temperature employed during degradation (365K *vs.* 315K for the data in Fig. 58).

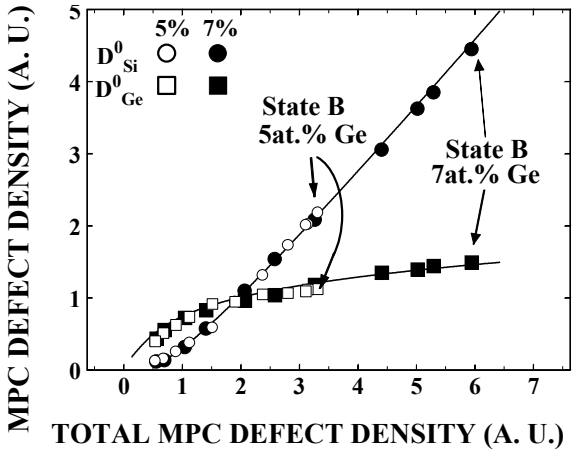

FIG. 59. MPC densities of Si and Ge deep defects as a function of the total density of defects during isochronal anneal sequences in the dark for the 7at.% Ge film and a 5at.% film. The data have been plotted on a *linear scale* for direct comparison with data given below.

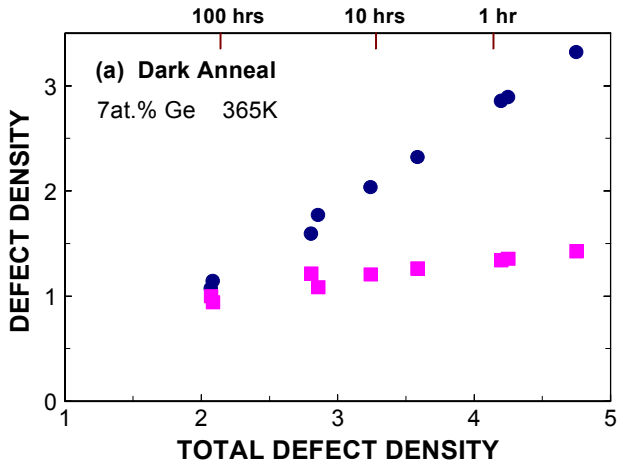

FIG. 60(a). Isothermal anneal in the dark at 365K following degradation in red-filtered light intensity of 2.5W/cm^2 for 12 hours at 365K**.**

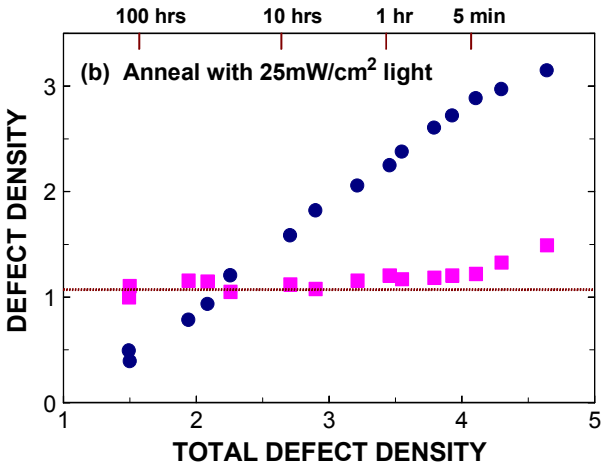

FIG. 60(b). Isothermal anneal at 365K in the presence of 25mW/cm^2 light after the same degradation as for Fig. 60(a).

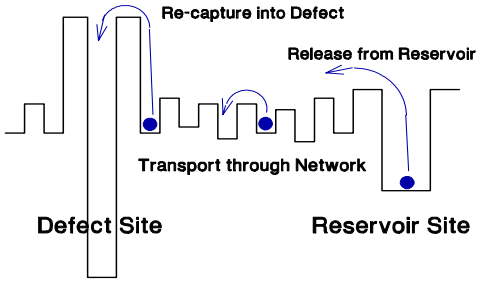

FIG. 61. Schematic indicating possible annealing steps in a global mediated process. The observed annealing kinetics will be determined by the rate-limiting step of the three processes indicated.

The second noteworthy point is the difference between the data in Fig. 60(a) and 60(b) in the initial stages of annealing; namely, the much more rapid initial decrease of N_{Ge} and slower decrease of N_{Si} in the presence of the light. This is a quite surprising result since it implies a difference in the relative annealing rates compared to the dark. This contradicts the simplest picture of a global annealing process in which the rate-limiting step would be the release of the mediating entity from the reservoir site (see Fig. 61) since, in that case, the *relative rates* of annealing between the two types of defects would not change. Instead, our data imply that the relative capture rates onto the two defect sites are being altered by the light. This suggests that the release rate of the mediating entity from the reservoir site may not be the rate-limiting step at all; rather, it is its recapture back onto the defect site. This recapture rate is apparently enhanced by the light and, moreover, the presence of the light causes the relative capture rates to become much more nearly equal.

Finally, we return to the saturation data of Fig. 54. We can demonstrate that the salient features of these data are now easily accounted for in detail within the context of global annealing provided we also limit the density of Ge dangling bond precursor sites. We begin by writing down the equation for light-induced defect creation plus annealing, including light-induced annealing, in its most general form:

$$\frac{dN_{Si}}{dt} = c_{SW}^{Si} N_{Si}^{P} - f_A(G,T) k_{Si} N_{Si} \tag{14}$$

where N_{Si}^{P} denotes the dangling bond precursor sites and $f_A(G,T)$ is a function describing the annealing which depends on the generation rate G and degradation temperature T. We've assumed the annealing rate will be linearly proportional to the density of defects, N_{Si}, and will also be proportional to the capture coefficient k_{Si} introduced in Eq. (9). In the bi-molecular carrier recombination (bcr) mechanism [61] the creation coefficient c^{Si}_{SW} can be expressed as $\alpha_{Si}G^2/N_{Si}^2$, where G is the optical carrier generation rate. For our purposes the exact form of this coefficient is not important except that it should have the general form: $c^{Si}_{SW} = \alpha_{Si}(T) f_C(G,T,N_R)$, where $f_C(G,T,N_R)$ is a function of the carrier concentrations, and thus depends on the generation rate, G, temperature, and the total density of recombination sites, N_R.

To extend Eq. (14) to the a-Si,Ge:H alloys we again need to incorporate a second type of dangling bond, but with a limited number of Ge dangling bond precursor sites, N^P_{Ge}, similar to Eq. (12). Since the results of Section 8.1 have clearly demonstrated the global nature of the annealing process, we propose that the annealing term have the form: $f_A(G,T)k_{Ge}N_{Ge}$, where $f_A(G,T)$ is exactly the same function appearing in Eq. (14) That is, if f_A describes the release of the mediating annealing entity from the reservoir site, it should be the same for both types of defects. Similarly, if creation of both types of defects is initiated by carrier recombination, then the coefficient for Ge dangling bond defect creation, c^{Ge}_{SW} will have the form: $\alpha_{Ge}(T)f_C(G,T,N_R)$. Finally, we must take into account the much lower apparent density of precursor sites, N_{Ge}^P. Thus, we write:

$$\frac{dN_{Ge}}{dt} = c^{Ge}_{SW}\left(N^P_{Ge} - N_{Ge}\right)G - f_A(G,T)k_{Ge}N_{Ge} \tag{15}$$

Under saturation conditions the left hand sides of Eqs. (14) and (15) vanish. Then, dividing Eq. (14) by Eq. (15), we may express the saturation density of Ge dangling bonds, N_{Ge}^S, in terms of that of the Si dangling bonds, N_{Si}^S:

$$N^S_{Ge} = N^P_{Ge}\left[\frac{N^S_{Si}}{(\eta/\xi)N^P_{Ge} + N^S_{Si}}\right] \tag{16}$$

The parameters ξ and η are obtained independently from our measurements of the detailed dependence of the N_{Ge} *vs.* N_{Si} trajectories during light induced degradation and thermal annealing, respectively (Fig. 56). Indeed, for the 7at.% Ge a-Si,Ge:H film in the relevant temperature range we have found that the ration of η/ξ has a value of roughly 0.1.

In Fig. 62 we have replotted the saturation data of Fig. 54 in the form N^S_{Ge} vs. N^S_{Si} and compare it directly (solid line) with the prediction of Eq. (16). Indeed, we see that we are able to quite successfully account for the relation between the saturated Ge and Si defect densities in these low Ge fraction a-Si,Ge:H samples. Again, the primary assumptions in this analysis are (1) the existence of a relatively small and fixed density of Ge precursor sites and (2) the existence of a global mechanism mediating the annealing process for both types of defects.

FIG. 62. The same data as in Fig. 54 but re-plotted to show the relationship between the saturated Ge dangling bond density with the saturated Si dangling bond density. The solid line is obtained from Eq. (16) using an analysis that assumes a global annealing process for both types of defects, plus a limited number of Ge dangling bond precursor sites.

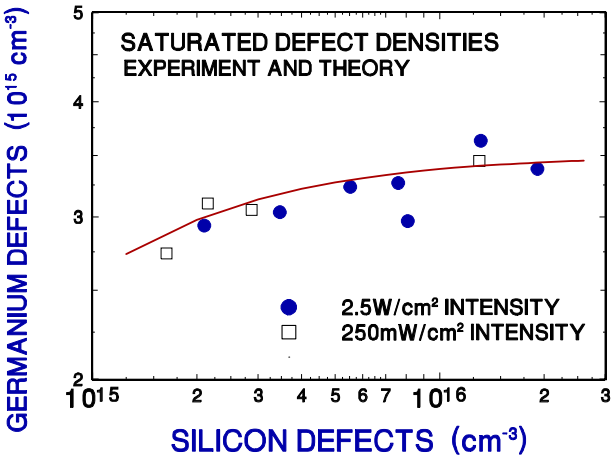

9.0 SUMMARY AND CONCLUSIONS

An overriding theme of the work described above in Sections 4 and 5 of our NREL Subcontract has been the effect of partial crystallinity, or the approach to partial crystallinity, on the electronic properties of a-Si:H. This includes, of course, how degradation or the relative stability of these films is affected by the approach to, or onset of, microcrystallinity. In Section 4 we described work on a set of samples which were produced by United Solar, deposited under conditions of high hydrogen dilution, such that they lay very close to but just below the microcrystalline phase boundary. Our measurements indicated that the defect density following light-induced degradation decreased as the film thickness increased. Corroborating our findings with X-ray diffraction results obtained by Don Williamson on sets of similar films, we concluded that the films were becoming more ordered and less defective just prior to the onset of a detectable microcrystalline component. Furthermore we found that at almost exactly the conditions that Don Williamson found XRD evidence for the onset of microcrystallinity we found the appearance of the distinctive "shoulder" in our sub-band-gap photocapacitance spectra. Some follow up experiments using AFM and KFM to study the surface of these samples confirmed the presence of Si crystalline regions at the surface of the thicker, hydrogen diluted films.

We next discussed (in Section 5) the results on a set of samples produced by dc reactive magnetron sputtering, obtained in collaboration with John Abelson's group at the University of Illinois, for which we demonstrated the existence of a small but significant microcrystalline component occupying about 5% of the total volume of these films. We discovered that the degradation kinetics was quite unusual in these films; however, it could be well accounted for by a model that postulated two phases of degrading material: the a-Si:H host material of good quality plus a more defective component associated with boundary regions near the microcrystallites. Our sub-band-gap photocapacitance measurements on these films again indicated the existence of a distinct feature (a "shoulder" with a threshold near 1.1eV) that signaled the presence of the microcrystalline phase.

A second major theme was the study of a-Si:H samples produced at significantly higher growth rates than the low deposition rate 1Å/s material that has led to the best performing cells. In Section 6, we reported our investigation of four sets of samples where the deposition rate had been enhanced to produce samples from moderate to high to extremely high rates. In the first set, produced at ETL, samples deposited under H_2 dilution at 10 Å/s, were found to exhibit extremely low deep defect densities and narrow Urbach tails, indicating films of exceptional quality. The photocapacitance spectra for these films were again found to contain evidence for a small degree of microcrystallinity. In the second and most extensive set of samples, deposited at BP Solar, both the hydrogen dilution and the power level were varied to produce a set of 9 films, along with 6 matched devices, whose growth rates varied from 0.65Å/s to 6Å/s. We found that the performance of the devices, particularly the fill factors, decreased roughly monotonically with increasing growth rate from 0.63 to 0.48. However, the deep defect densities were found to be

nearly constant. Somewhat to our surprise, we found that by far the strongest correlation between film and device properties involved the Urbach energies in this set of samples. Specifically, an increasing bandtail width in the films correlated fairly directly with poorer fill factors in the matched devices. This tends to point quite directly to the hole transport properties, although our measured values of the hole $\mu\tau$ products did not correlate nearly as well. In another couple higher growth rate samples, produced at United Solar, we again found evidence for somewhat larger Urbach energies for the films deposited at higher rates, also an increasing defect density in the higher deposition rate films.

The fourth set of high growth rate samples we examined were a couple of ultra-high growth rate HWCVD samples produced at NREL at 90Å/s and 130Å/s. We found that defect densities and Urbach energies were a bit higher than lower growth material, but only modestly so. For example, the 130Å/s sample had degraded defect densities that were below 4×10^{16} cm^{-3} and its Urbach energy was only 53meV. That is, these values were not really any higher than for device quality glow discharge a-Si:H deposited at 6Å/s. Therefore, this again seems to point to extraordinary properties of HWCVD a-Si:H compared to a-Si:H deposition by other techniques.

The final major theme was concerned with the general area of the a-Si,Ge:H mid-gap and low-gap alloys. Actually, these alloy studies had two distinct purposes. The first was to characterize the electronic properties of a-Si,Ge:H material in different alloy regimes, or produced by different growth methods, than those examined by us previously. Thus we obtained much lower fraction Ge alloys from United Solar (below 20at.%) than the United Solar samples we had examined before which mostly encompassed the range 30 to 50at.%. We also looked at a few a-Si,Ge:H samples produced by the dc glow discharge method at BP Solar, and a few alloy samples produced by the hot-wire CVD method at NREL. The second purpose evolved after we had examined the low Ge fraction a-Si,Ge:H films. We discovered that we could clearly identify two distinct deep defect bands in these samples using the modulated photocurrent method and that these deep defect both exhibited metastable behavior, with somewhat different characteristics. Thus, we realized that correlations in such metastable behavior of these two types of deep defects might give us important new insights into the fundamental mechanism of light-induced degradation in amorphous silicon itself.

For the six United Solar mid-gap a-$Si_{1-x}Ge_x$:H samples, with $0.02 \leq x \leq 0.2$, the two types of deep defects revealed by modulated photocurrent spectroscopy were identified to be neutral Si and neutral Ge dangling bonds from auxiliary ESR measurements. For all the alloys in the series we found that the Ge dangling bonds dominated the total in the dark-annealed state while the Si dangling bond density was larger in the light-degraded state. For three of these samples (Ge fractions of 5, 13.5, and 20at.%) we also looked for correlations between film properties with corresponding device performance. Unlike the cases of high growth rate material, the Urbach energies for this set of alloy samples were nearly constant. Also in contrast to the results for the BP a-Si:H samples, the fill factors in the devices *did* appear to be inversely correlated with the film deep defect densities provided that defect density exceeded about 7×10^{15} cm^{-3}.

We also evaluated the quality of a-Si,Ge:H alloys from BP Solar and NREL employing the growth techniques that were new to us. Our measurements indicated that the BP Solar dc glow discharge material seemed to have exceptional properties up to a Ge fraction of 40at.%. There was also evidence from sub-band-gap spectra using the transient photocapacitance method that the lower Ge fraction samples exhibited two distinct types of deep defects. The NREL HWCVD alloy material, on the other hand, while very good at the 5at.% Ge level, appeared inferior for Ge fractions at or above 20at.%. This tend to support the notion that ion bombardment is particularly important for good electronic properties in the a-Si,Ge:H alloys, in contrast to the case of pure a-Si:H. Such ion bombardment is obviously absent in the HWCVD growth process. This is clearly an area where additional study will be important.

Finally, we summarize our results from the studies of the United Solar low Ge fraction a-Si,Ge:H alloy films intended to provide new tests concerning the fundamental mechanisms for deep defect creation. We noted that these films contain two types of deep defects (Si and Ge dangling bonds) that both degrade and anneal at different rates. After detailed study we deduced specific correlations in these processes for the two types of defects. In particular, we determined that correlations between the annealing of these defects required that a *global mediating entity* (perhaps mobile hydrogen, or propagating strain causing remote bond breaking) must be involved in the defect creation process. We also found that, in contrast to the metastable Si dangling bonds, there appeared to be a distinct and fairly low limit to the density of Ge dangling bond precursor sites. Light-induced annealing studies were also carried out and provided some additional insight. Specifically, we noted that the most general global process could involve up to three distinct steps for the annealing of deep defects: release of the mediating entity from some reservoir site, transport of this entity, and re-trapping of the entity at the dangling bond to eliminate it as an active defect. The light induced annealing studies pointed to last of these as being the rate-limiting step in certain cases.

10.0 SUBCONTRACT SUPPORTED PUBLICATIONS

1. Chih-Chiang Chen, Fan Zhong, J. David Cohen, Jeffrey C. Yang, and Subhendu Guha, "Evidence for charged defects in intrinsic glow discharge hydrogenated amorphous silicon-germanium alloys", Phys. Rev. B**57**, R4210 (1998).

2. Yoram Lubianiker, J. David Cohen, Hyun-Chul Jin, and John R. Abelson, "Degradation kinetics of hydrogenated amorphous silicon: the effect of embedded microcrystallites", Mat. Res. Soc. Symp. Proc. **507**, 729 (1998).

3. Chih-Chiang Chen, Yoram Lubianiker, J. David Cohen, Jeffrey C. Yang, Subhendu Guha, Paul Wickboldt, and William Paul, "The electronic structure, metastability, and transport properties of optimized amorphous silicon-germanium alloys", Mat. Res. Soc. Symp. Proc., **507**, 769 (1998).

4. S. Guha, J. Yang, D.L. Williamson, Y. Lubianiker, J.D. Cohen, and A.H. Mahan, "Structural, defect and device behavior of hydrogenated amorphous Si near and above the onset of microcrystallinity", Appl. Phys. Lett. **74**, 1860 (1999).

5. Y. Lubianiker, J.D. Cohen, H-C. Jin and John R. Abelson, "The effect of embedded microcrystallites on the light-induced degradation of hydrogenated amorphous silicon", Phys. Rev. B**60**, 4434 (1999).

6 S. Guha, J. Yang, D.L. Williamson, Y. Lubianiker, J.D. Cohen, and A.H. Mahan, "Structural, defect and device behavior of hydrogenated amorphous Si near and above the onset of microcrystallinity", Appl. Phys. Lett. **74**, 1860 (1999).

7. Y. Lubianiker, J.D. Cohen, H.-C. Jin, and J.R. Abelson, "Effect of embedded microcrystallites on the light-induced degradation of hydrogenated amorphous silicon", Phys. Rev. B**60**, 4434 (1999).

8. Y. Lubianiker, Y. Tan, J.D. Cohen, G. Ganguly, "High Quality a-Si:H films grown at high deposition rates", Mat. Res. Soc. Symp. Proc **557**, 139 (1999).

9. Y. Lubianiker, Y. Tan, J.D. Cohen, and G. Ganguly, "Amorphous silicon deposited at high growth rate near the onset of crystallinity", J. Non-Cryst. Solids **266-269**, 450 (2000).

10. Y. Lubianiker, J.D. Cohen, G. Lubarsky, Y. Rosenwaks, J. Yang, and S. Guha, "Structural and electronic properties of optimized a-Si:H films", J. Non-Cryst. Solids J. Non-Cryst. Solids **266-269**, 253 (2000).

11. K. C. Palinginis, J. David Cohen, J.C. Yang, and S. Guha, "Defect bands in a-Si,Ge:H alloys with low Ge content", J. Non-Cryst. Solids **266-269**, 665 (2000).

12. K.C. Palinginis, J.D. Cohen, J.C. Yang, and S. Guha, "A critical test of defect creation models in hydrogenated amorphous silicon alloys", Mat. Res. Soc. Symp. Proc. **609**, A3.3, (2000).

13. J.D. Cohen, J. Heath, K.C. Palinginis, J.C. Yang, and S. Guha, "Light-induced annealing of deep defects in low Ge fraction a-Si,Ge:H alloys: Further insights into the fundamentals of light-induced degradation", Mat. Res. Soc. Symp. Proc. **664**, A12.5 (2001).

14. J. Heath, S.B. Iyer, Y. Lubianiker, J.D. Cohen, and G. Ganguly, "Correlation between film and cell properties for DC plasma deposited amorphous silicon", Mat. Res. Soc. Symp. Proc. **664**, A25.3 (2001).

15. Kimon C. Palinginis, J. David Cohen, Jeffrey C. Yang, and Subhendu Guha, "Experimental evidence indicating a global mechanism for light-induced degradation in hydrogenated amorphous silicon", Phys. Rev. B**63,** 201203(Rapids) (2001).

16. A.H. Mahan, Y. Xu, B.P. Nelson, R.S. Crandall, J.D. Cohen, K.C. Palinginis, and A.C. Gallagher, "Saturated defect densities of hydrogenated amorphous silicon grown by hot-wire chemical vapor deposition at rates up to 150Å/s", Appl. Phys. Lett. **78**, 3788 (2001).

17. B.D. Chapman, S.-W. Han, G.T. Seidler, E.A. Stern, J.D. Cohen, S. Guha, and J. Yang, "Short-range compositional randomness of hydrogenated amorphous silicon-germanium films", J. Appl. Phys, in press.

18. J.D. Cohen, J. Heath, K. Palinginis, J. Yang, and S. Guha, "Insights into the mechanisms of light-induced degradation from studies of defects in low Ge fraction a-Si,Ge:H alloys", J. Non-Cryst. Solids, in press.

11.0 REFERENCES

1. M. Pinarbasi, M. J. Kushner, and J. R. Abelson, J. Appl. Phys. **68**, 2255 (1990).
2. G. Feng, M. Katiyar, Y. H. Yang, J. R. Abelson, and N. Maley, Mat. Res. Soc. Symp. Proc. **258**, 179 (1992).
3. J.E. Gerbi and J.R. Abelson, Mat. Res. Soc. Symp. Proc. **507**, 429 (1998).
4. D. Kwon, H. Lee, J.D. Cohen, H.-C. Jin, and J.R. Abelson, J. Non-Cryst. Solids **227-230**, 1040 (1998).
5. S. Guha, J. Yang, D.L. Williamson, Y. Lubianiker, J.D. Cohen, and A.H. Mahan, Appl. Phys. Lett. **74**, 1860 (1999).
6. R. Hayashi, T. Takagi, G. Ganguly, M. Fukawa, M. Kondo and A. Matsuda, Proc. 2nd WCEPVSEC, 925 (1998).
7. B.P. Nelson, R.S. Crandall, E. Iwaniczko, A.H. Mahan, Q. Wang, Y. Xu, and W. Gao, Mater. Res. Soc. Symp. Proc. **557**, 97 (1999).
8. B.P. Nelson, Y. Xu, A.H. Mahan, D.L. Williamson, and R.S. Crandall, Mater. Res. Soc. Symp. Proc. **609**, A22.8 (2000).
9. D.V. Lang, J.D.Cohen, and J.P. Harbison, Phys. Rev. B**25**, 5285 (1982).
10. C.E. Michelson, A.V. Gelatos, and J.D. Cohen, Appl. Phys. Lett. **47**, 412 (1985).
11. K.K. Mahavadi, K. Zellama, J.D. Cohen, and J.P. Harbison, Phys. Rev. B**35**, 7776 (1987).
12. T. Unold, J. Hautala, and J.D. Cohen, Phys. Rev. B**50**, 16985 (1994).
13. H. Oheda, J. Appl. Phys. **52**, 6693 (1981).
14. G. Schumm and G.H. Bauer, Phys. Rev. B**39**, 5311 (1989).
15. R. Brüggemann, C. Main, J. Berkin, and S. Reynolds, Phil. Mag. B**62**, 29 (1990)
16. Lang, D.V. in *Thermally Stimulated Relaxation in Solids*, vol. 37 of Topics in Applied Physics, ed by P. Braunlich (Springer, Berlin, 1979), p. 93.
17. Cohen, J.D., in *Hydrogenated Amorphous Silicon*, vol. 21C of *Semiconductors and Semimetals*, ed. by J. Pankove (Academic Press, New York, 1984), p. 9.
18. J.D. Cohen and A.V. Gelatos, in *Advances in Disordered Semiconductors Vol I: Amorphous Silicon and Related Materials*, ed. by H. Fritzsche (World Scientific, Singapore, 1988), pp. 475-512.
19. J. David Cohen, Thomas Unold, A.V. Gelatos, and C.M. Fortmann, J. Non-Cryst. Solids **141**, 142 (1992).
20. C.-C. Chen, F. Zhong, J.D. Cohen, J.C. Yang, and S. Guha, Phys. Rev. B**57**, R4210 (1998).
21. S. Guha, J. Yang, D.L. Williamson, Y. Lubianiker, J.D. Cohen, and A.H. Mahan, Appl. Phys. Lett. 74, 1860 (1999).
22. D.V. Tsu, B.S. Cho, S.R. Ovshinsky, S. Guha and J. Yang, Appl. Phys. Lett. **71**, 1317 (1997).

23. A.V. Gelatos, K.K. Mahavadi, J.D. Cohen, and J.P. Harbison, Appl. Phys. Lett. **53**, 403 (1988).

24. T. Unold, J. Hautala, and J.D. Cohen, Phys. Rev. B**50**, 16985 (1994).

25. A.V. Gelatos, K.K. Mahavadi, J.D. Cohen, and J.P. Harbison, Appl. Phys. Lett. **53**, 403 (1988).

26. R. Shikler, T. Meoded, N. Fried, Y. Rosenwaks, Appl. Phys. Lett. 74 2972 (1999), and references therein.

27. R. Platz and S. Wagner, Appl. Phys. Lett. 73, 1236 (1998).

28. X. Xu, J. Yang, A. Banerjee, S. Guha, K. Vasanth, S. Wagner, Appl. Phys. Lett. 67, 2323 (1995).

29. S. Hamma, P. Roca i Cabarrocas, Appl. Phys. Lett. 74, 3218 (1999).

30. D. Kwon, C.-C. Chen, J.D. Cohen, H.-C. Jin, E. Hollar, I. Robertson, and J.R. Abelson, Phys. Rev. B**60**, 4442 (1999).

31. M. Stutzmann, W.B. Jackson and C.C. Tsai, Phys. Rev. B**32**, 23 (1985).

32. Z.Y. Wu, J.M. Siefert and B. Equer, J. Non-Cryst. Solids **137-138**, 227 (1991).

33. L. Yang and L.-F. Chen, Mat. Res. Soc. Symp. Proc. **297**, 619 (1993).

34. Y. Lubianiker, J.D. Cohen, H.-C. Chul, and J.R. Abelson, Mat. Res. Soc. Symp. Proc. **507**, 729 (1998).

35. Y. Lubianiker, J.D. Cohen, H.-C. Jin, and J.R. Abelson, Phys. Rev. B**60**, 4434 (1999).

36. Unusual defect creation kinetics have been observed in several a-Si:H samples deposited under high hydrogen dilution by the Penn State group.

37. S. Vignoli, R. Meaudre, M. Meaudre, P. Roca I Cabarrocas, C. Godet and P. Morin, J. Non-Cryst. Solids **198-200**, 474 (1996).

38. D.V. Tsu, B.S. Cho, S.R. Ovshinsky, S. Guha, and J. Yang, Appl. Phys. Lett. **71**, 1317 (1997).

39 A. Matsuda, J. Non-Cryst. Solids **59-60**, 767 (1983).

40. R. Robertson and A. Gallagher, J. Appl. Phys. **59**, 3402 (1986).

41. A.H. Mahan, Y. Xu, B.P. Nelson, R.S. Crandall, J.D. Cohen, K.C. Palinginis, and A.C. Gallagher, Appl. Phys. Lett. **78**, 3788 (2001).

42. See, for example, C. Maltern et al., in Mat. Res. Soc. Symp. Proc. **377**, 505 (1995).

43. W. Fuhs, F. Finger, J. Non-Cryst. Solids **114**, 387 (1989).

44. F. Zhong and J.D. Cohen, Mat. Res. Soc. Symp. Proc.**258**, 813 (1992).

45. J.David Cohen and Daewon Kwon, J. Non-Cryst. Solids **227**, 348 (1998).

46. C.-C. Chen, F. Zhong, J.D. Cohen, J.C. Yang, and S. Guha, Mat. Res. Soc. Symp. Proc. **467**, 55 (1997).

47. S. Aljishi, Z E. Smith, and S. Wagner, in *Amorphous Silicon and Related Materials*, ed. by H. Fritzsche (World Scientific, Sinapore, 1989), pp. 887-938.

48. M. Stutzmann., R.A. Street, C.C. Tsai, J.B. Boyce, and S.E. Ready, J. Appl. Phys. **66**, 569 (1989).

49. P. Della Sula, C. Reita, G. Conte, F. Galluzzi and G. Grillo, J. Appl. Phys. **67**, 814 (1990).

50. C. Tzoumanekas and P.C. Kelires, Phys. Rev. B**60**, 14205 (1999); J. Non-Cryst. Solids **266-269**, 670 (2000).

51. L. Incoccia, S. Mobilio, M.G. Proietti, P. Fiorini, C. Giovannella, and G. Evangelisti, Phys. Rev. B, 1028 (1985).

52. Y. Nishino, S. Muramatsu, Y. Takano, and H. Kajiyama, Phys. Rev. B**38**, 1942 (1988).

53. S. Minomura. K. Tsuji, M. Wakagi, T. Ishidate, K. Inoure, and M. Shibuya, J. Non-Cryst. Solids **59&60**, 541 (1983).

54. H. Kajiyama, S.-I. Muramatsu, T. Shimala, and Y. Nishino, Phys. Rev. B**45**, 14005 (1992).

55. M. Matsuura, J. M. Tonnerre, and G.S. Cargill, Phys. Rev. B**44**, 3842 (1991).

56. M.C. Ridgway, K.M. Yu, C.J. Glover, G.J. Foran, C. Clere, J.L. Hansen, and A.N. Larsen, Phys. Rev. B**60**, 10831 (1999).

57. G. Goerigk and D.L. Williamson, J. Non-Cryst. Solids **281**, 181 (2001).

58.. Z.Y. Wu, Siefert, and B. Equer, J. Non-Cryst. Solids **137&138**, 227 (1991).

59 . R. Meaudra and M. Meaudre, Phys. Rev. B**45**, 12134 (1992).

60. H.M. Branz, Phys. Rev. B**59**, 5498 (1999).

61. M. Stutzmann, W. B. Jackson, C.-C, Tsai, Phys. Rev. B**32**, 23 (1985)

62. See, for example, H. Gleskova and S. Wagner, J. Non-Cryst. Solids **190**, 157 (1995).

H. Fritzsche (World Scientific, Sinapore, 1989), pp. 887-938.

48. M. Stutzmann., R.A. Street, C.C. Tsai, J.B. Boyce, and S.E. Ready, J. Appl. Phys. **66**, 569 (1989).
49. P. Della Sula, C. Reita, G. Conte, F. Galluzzi and G. Grillo, J. Appl. Phys. **67**, 814 (1990).
50. C. Tzoumanekas and P.C. Kelires, Phys. Rev. B**60**, 14205 (1999); J. Non-Cryst. Solids **266-269**, 670 (2000).
51. L. Incoccia, S. Mobilio, M.G. Proietti, P. Fiorini, C. Giovannella, and G. Evangelisti, Phys. Rev. B, 1028 (1985).
52. Y. Nishino, S. Muramatsu, Y. Takano, and H. Kajiyama, Phys. Rev. B**38**, 1942 (1988).
53. S. Minomura. K. Tsuji, M. Wakagi, T. Ishidate, K. Inoure, and M. Shibuya, J. Non-Cryst. Solids **59&60**, 541 (1983).
54. H. Kajiyama, S.-I. Muramatsu, T. Shimala, and Y. Nishino, Phys. Rev. B**45**, 14005 (1992).
55. M. Matsuura, J. M. Tonnerre, and G.S. Cargill, Phys. Rev. B**44**, 3842 (1991).
56. M.C. Ridgway, K.M. Yu, C.J. Glover, G.J. Foran, C. Clere, J.L. Hansen, and A.N. Larsen, Phys. Rev. B**60**, 10831 (1999).
57. G. Goerigk and D.L. Williamson, J. Non-Cryst. Solids **281**, 181 (2001).
58.. Z.Y. Wu, Siefert, and B. Equer, J. Non-Cryst. Solids **137&138**, 227 (1991).
59 . R. Meaudra and M. Meaudre, Phys. Rev. B**45**, 12134 (1992).
60. H.M. Branz, Phys. Rev. B**59**, 5498 (1999).
61. M. Stutzmann, W. B. Jackson, C.-C, Tsai, Phys. Rev. B**32**, 23 (1985)
62. See, for example, H. Gleskova and S. Wagner, J. Non-Cryst. Solids **190**, 157 (1995).

REPORT DOCUMENTATION PAGE

Form Approved
OMB NO. 0704-0188

1. AGENCY USE ONLY (Leave blank)	2. REPORT DATE	3. REPORT TYPE AND DATES COVERED
	July 2002	Final Subcontract Report, 16 January 1998-15 October 2001

4. TITLE AND SUBTITLE
Identifying Electronic Properties Relevant to Improving the Performance and Stability of Amorphous Silicon Based Mid-Gap and Low-Gap Cells, Final Subcontract Report, 16 January 1998-15 October 2001

5. FUNDING NUMBERS
CF: XAF-8-17619-05
PVP25001

6. AUTHOR(S)
J. David Cohen

7. PERFORMING ORGANIZATION NAME(S) AND ADDRESS(ES)
University of Oregon
Eugene, Oregon

8. PERFORMING ORGANIZATION REPORT NUMBER

9. SPONSORING/MONITORING AGENCY NAME(S) AND ADDRESS(ES)
National Renewable Energy Laboratory
1617 Cole Blvd.
Golden, CO 80401-3393

10. SPONSORING/MONITORING AGENCY REPORT NUMBER
NREL/SR-520-32535

11. SUPPLEMENTARY NOTES
NREL Technical Monitor: B. von Roedern

12a. DISTRIBUTION/AVAILABILITY STATEMENT
National Technical Information Service
U.S. Department of Commerce
5285 Port Royal Road
Springfield, VA 22161

12b. DISTRIBUTION CODE

13. ABSTRACT *(Maximum 200 words)* This report describes our experimental studies which have been concentrated in roughly five areas. Specifically: (1) We have examined a-Si:H grown very close to the microcrystalline phase boundary, so-called “edge material,” to help understand why such material is more stable with respect to light-induced degradation; (2) We have also studied the electronic properties, and degradation characteristics of mixed phase material that is mostly a-Si:H, but which contains a significant microcrystalline component; (3) We have examined the electronic properties of high deposition rate material. These studies have included both moderately high deposition rate material (up to 6Å/s) produced by the PECVD growth method, and extremely high deposition rate material (up to 130Å/s) produced by the HWCVD growth method. (4) We have examined series of a-Si,Ge:H alloys from several sources. In one extensive series of studies we examined low Ge fraction alloys in an attempt to learn more about the fundamentals of degradation in general. In a couple other studies we evaluated the properties of a-Si,Ge:H alloys produced by methods we had not previously examined. (5) Finally, for three different types of samples we compared basic material properties with companion cell performance data. This was carried out in each case on series of samples for which one or more specific deposition parameters were varied systematically.

14. SUBJECT TERMS: PV; microcrystallites; high hydrogen dilution; X-ray diffraction (XRD); reactive magnetron sputtering; hot-wire CVD films; light-induced photocurrent; a-Si:H; photocapacitance; light-soaking time; defect density; isothermal anneal

15. NUMBER OF PAGES

16. PRICE CODE

17. SECURITY CLASSIFICATION OF REPORT	18. SECURITY CLASSIFICATION OF THIS PAGE	19. SECURITY CLASSIFICATION OF ABSTRACT	20. LIMITATION OF ABSTRACT
Unclassified	Unclassified	Unclassified	UL